Photoacoustics and Fluorescence based Nanoprobes towards Functional and Structural Imaging *in vivo*

by

Aniruddha Ray

A dissertation submitted in partial fulfillment
of the requirements for the degree of
Doctor of Philosophy
(Biophysics)
in the University of Michigan
2013

Doctoral Committee:
Professor Raoul Kopelman, Chair
Professor Zhan Chen
Professor Ari Gafni
Professor Mary-Ann Mycek
Associate Professor Jennifer Ogilvie
Assistant Professor Xueding Wang

A prayer for the Teacher and Student

ॐ सह नाववतु ।
सह नौ भुनक्तु ।
सह वीर्यं करवावहै ।
तेजस्वि नावधीतमस्तु मा विद्विषावहै ।
ॐ शान्तिः शान्तिः शान्तिः ॥

“Om, may GOD protect us both,

May GOD nourish us both,

May we work together with energy and vigour,

May our study be enlightening, not giving rise to hostility,

Om, Peace, Peace, Peace.”

- Taittiriya Upanishad (~600BC)

ACKNOWLEDGEMENTS

With deep sense of gratitude, I wish to express my reverence towards my supervisor Dr. Raoul Kopelman for his excellent mentorship. He has always been very supportive and receptive of my ideas and has given me the opportunity to explore new areas during the course of my research. His profound knowledge and stimulating enthusiasm towards science and scientific research have been a great source of inspiration and motivation for me and will remain so throughout my career. I have immensely benefited from the numerous discussions on many aspects of research and I could not have asked anything more from him. It is indeed a great opportunity for me to work under his erudite supervision.

I would also like to thank profusely Dr. Xueding Wang for his valuable guidance on Photoacoustics. He has been an excellent mentor throughout my association with him. With his vast knowledge and experience on Photoacoustics, he was always on hand to help me with the experiments. I am also very grateful to him for the financial support he provided to me during this summer and for attending conferences.

I would also like to express my deep sense of appreciation to the other distinguished members of my doctoral committee Dr. Zhan Chen, Dr. Ari Gafni, Dr. Mary-Ann Mycek and Dr. Jennifer Ogilvie. I would like to thank Dr. Chen for his valuable comments and critiques on my research. His great depth of knowledge on nonlinear optics has been very helpful to me. I am very thankful to Dr. Gafni for all his help, advice and guidance since my first year, when he was the chair of the Biophysics graduate committee. Dr. Gafni has been very supportive especially during some

difficult times in my second year and has been a valuable mentor for me throughout. I would like to thank Dr. Mycek for bringing her expertise in the area of Bio-medical Optics into my research. I had taken her course on Biomedical Optics and thoroughly enjoyed it and also got to learn a great deal from it. I am very grateful to her for her valuable advice regarding the different aspects of my projects and also about career options in this field. I did my first rotation with Dr. Ogilvie and I can never thank her enough for all her help during that period. She not only taught me a lot about Raman microscopy, but also helped me adjust to life here. I still recall how she helped me ease into life here, often giving valuable advice about academics and university life. Her expertise on optics has been valuable to me in my projects as well. I will remain deeply indebted to her for all her support.

I am pleased to record my sincere thanks to Dr. Prasanta Kumar Datta who was my supervisor during my undergraduate studies at IIT. Kharagpur. He had been a great mentor not only throughout my undergraduate research but even now. He instilled in me a curiosity towards research that led me to consider graduate studies in the first place. I would also like to thank my teacher Dr. Prabir Chakraborty and previous group members especially Dr. Sourabh Mukhopadhyay & Dr. Susanta Das for their help during my early research. I would also like to take this opportunity to thank Dr. Koen Visscher, University of Arizona, for introducing me to bio-photonics during my internship in his laboratory and initiating me into this field.

My current group members have had a big contribution towards my work and life as well. I have greatly enjoyed working with them. I would like to thank Dr. Yong-Eun Koo Lee for her constant support and guidance. She had helped me on numerous occasions from teaching new techniques to troubleshooting experiments, editing and critically analyzing my write-ups. I thank Taeyjuana Curry for being a wonderful friend and for editing a part of my thesis; Remy Elbez

and Ariel Hecht for being part of our ESPN trio and all the fun times we had together as well as for the frequent stimulating discussions; Kristen Herrmann for being one of my closest friends and sharing so many wonderful moments together as well as for her support during any difficult times and also for the tips she provided regarding *in vivo* experiments; Leshern Karamchand for being a big brother and for all his help in both academic & non-academic aspect, lessons in cell biology as well as for editing a part of my thesis; my close friends Hyung Ki Yoon, Teppei Shirakura and Ming Qin for the enjoyable conversations and all the help, advice regarding nanoparticle synthesis; Dr. Kim and Dr. Hah for teaching me protocols of nanoparticle synthesis, cell work and for sharing their expert advice whenever needed. I could not have asked for a better group of colleagues and I am extremely thankful to each and everyone.

I would also like to thank the PIBS directors Dr. Kate Barald and Dr. Lori Isom and the rest of the staff in PIBS, Biophysics and Chemistry as well as Dr. Kopelman's assistants Stephanie D'Cruz and Maddy Kelly. I would also like to acknowledge the funding from National Institute of Health, National Science Foundation, Rackham research and travel grants, SPIE student scholarship and the PIBS fellowship.

I am really thankful to all my friends, with whom I have really enjoyed my time, be it during traveling, sports or other activities. I am thankful to them for their wonderful company. Last but not the least I would like to thank my parents, sister and grandparents for their continuous love, support, encouragement and blessings. It has been a privilege to have come across so many wonderful people in my life including my supervisors, professors, friends and family and I am very thankful to everyone for their support and the part they played in my life.

Table of Contents

Acknowledgements…….. ii

List of Figures……...…vii

Abstract ……xi

Chapter

1. Introduction…….…….. 2
   Reference…….. 15
2. Development of two-photon fluorescent nanoprobe: Subcellular pH Measurements…...18
   Introduction…….....18
   Experimental ……21
   Results and Discussion ….……26
   Acknowledgement…….36
   References……..37
3. Core-Shell nanoprobes for enhanced two photon fluorescence imaging: application to subcellular pH ……...39
   Introduction…….....39
   Experimental ……43
   Results and Discussion ….……50
   Acknowledgement…….62
   References……..63
4. Nanoprobe aided pH measurement *in vivo* using photoacoustics **..**……..65
   Introduction…….....65
   Experimental ……67
   Results and Discussion ….……68
   Acknowledgement……74
   References……75
5. Oxygen sensing *in vivo* using photoacoustics**..**…….77
   Introduction…….....77
   Experimental ……81
   Results and Discussion ….……82
   Acknowledgement…….87
   References……..88

6. Nano-Contrast Agent for Brain Tumor Delineation using Photoacoustics..……..……..90
Introduction…….....90
Experimental ……94
Results and Discussion ….……98
Acknowledgement…….……..110
References……111
7. Summary and Future directions……...……...114
Summary...……114
Future directions ……..……118
References……122

List of Figures

Figure1.1: The Jablonski diagram demonstrating the two photon fluorescence. Electrons are excite from the ground state to the excite state via short lived intermediate states by simultaneous absorption of two Near Infrared (NIR) photon……...5

Figure 1.2: Flowchart demonstrating the mechanism of Photoacoustics……7

Figure 1.3 (a) Sonogram of a triangular piece of rubber. The sonogram is constructed from p_δ (b) The photoacoustic image of the rubber (obtained from the sonogram by using back projection algorithm in this case)…….…….. 11

Figure 2.1: Two photon pH dependent fluorescence excitation spectra of HPTS-NP…….27

Figure 2.2: pH calibration curve of the HPTS-NP. The two photon calibration curve was obtained by taking the ratio of the total fluorescence intensity, measured around 510nm, when excited at 900 nm vs. 752nm wavelength. (R sq value is 0.98). The single photon calibration curve was obtained by taking the ratio of excitation at 452nm and 418nm (the isobestic point). (R sq value is 0.96) ……28

Figure 2.3: Two photon pH response of the (a) BCECF and (b) Lysosensor based nanoprobes..29

Figure 2.4: Two Photon image of the 9L rat glioma cells (Scale 50μm). This image was obtained by exciting the live cells at 900nm. A 10X magnification was used for this image. The fluorescence signal was recorded using a PMT…….31

Figure 2.5: Overlay of the fluorescence from nanoprobes (green) and the lysotracker (red). Orange/Yellow shows the position of nanoprobes overlapping with lysosomes. We see that only a small fraction of nanoparticles are inside the lysosomes. The nanoparticles were excited by both 405nm and 450nm, while the lysotracker was excited by 568nm wavelength. This image was taken in the confocal mode. (Scale 20μm)…….32

Figure 2.6: Autofluorescence from the 9L control cells when excited with (a) 405 nm, (b) 450 nm and (c) 752 nm (Scale 20 μm). The single photon autofluorescence images (a&b) were performed in the confocal mode……32

Figure 2.7: (a) A two-photon fluorescence image of the Hela cell spheroid with pH sensing nanoparticles, excited at 900nm (Spheroid size ~0.8 mm), (b) pH distribution inside the HeLa

Cell spheroid. The blue pixels have a pH value of 7.4 whereas the red pixels have an average value of 6.5, The overlay (pink pixels) have a pH value inbetween 6.5 and 7.4……..33

Figure 2.8: The pH distribution inside the spheroid as obtained from Fig7. We observe the average pH value is around 7.05……34

Figure 3.1: Potential two photon fluorescence enhancement mechanisms ……..43

Figure 3.2: Characterization of the nanoparticle. (a) Second Harmonic generated by the 60 nm silver nanospheres, irradiated at 900 nm. (b) pH dependent two photon excitation spectra from the nanoparticles, (c) XRD pattern recorded from the nanoparticles with silver core. The peaks corresponds to the (111) and (200) reflection of the fcc silver, respectively (d) TEM image of the nanoparticles containing silver (Scale: 100 nm). Inset: magnified image of the nanoparticle (3X)……...49

Figure 3.3: Two-photon fluorescence enhancement of the HPTS-nanoparticles with 60 nm silver core (Fig. 3a) and 10 nm silver core (Fig. 3b). For the 60 nm silver we see a maximum enhancement of 20 times whereas for the 10 nm silver we see a maximum enhancement of only 2.2 times……52

Figure 3.4: The pH calibration curve of the nanoparticles. The curve is constructed by taking the ratio of the fluorescence when excited by 900 nm and 740 nm photons. We obtain an R^2 value of 0.98……57

Figure 3.5: A two-photon fluorescence image of the MDA-MB-435 cells with pH sensing, core-shell nanoparticles, excited at 900 nm (The scale bar represents 20 μm). Monitored is the pH of the acidic endosomes/lysosomes in which the nanosensors are preferentially localized/trapped, in contrast to other cell locations…….....58

Figure 3.6: Fluorescence images from the cells. (a) Fluorescence signal from the nanoparticles inside the MDA cells, (b) Fluorescence signal from the lysotracker dye used to stain the acidic vesicles and (c) Overlay of the fluorescence from nanoparticles (green) and the lysotracker (red). Orange/Yellow shows the position of nanoparticles overlapping with acidic vesicles. We see that many of the nanoparticles are inside acidic vesicles (Scale 20μm). This image was taken in the confocal mode…… 60

Figure 4.1: Interference with albumin. Changes in the absorption of the dye and the nanoprobe in presence of albumin.……..68

Figure 4.2: Schematic setup for the experiment on live rats. ……..…….69

Figure 4.3: *In vitro* pH calibration curve. The calibration curve was obtained by taking the ratio of the photoacoustic signal intensities when the nanoprobes were illuminated at 580nm and 565nm, respectively……...……71

Figure 4.4: Photoacoustic signal intensity at (a) 580nm and (b)565nm respectively, from a rat tail joint before and after the local injection of the pH sensitive nanoprobes……..72

Figure 5.1: The schematic of the experimental setup. PD: Photodiode, OPO: Optical parametric oscillator, Nd Laser: Second harmonic of Nd:YAG laser. The dye laser is used to trigger the delay generator which, in turn, triggers the OPO after a set delay. The acoustic signal corresponding to different delay times is measured using the transducer…….81

Figure 5.2: (a) The photoacoustic (PA) signals from the G2 dye dissolved in water (containing 6% albumin), correspondent to different pump-probe delays. (b) The *in-vitro* change in the photoacoustic amplitude with time. The exponential decay curves for oxygen saturated water and air saturated water, mixed with albumin, are shown for comparison……....82

Figure 5.3: (a) The *in vivo* change in the photoacoustic amplitude with time. The exponential decay curves for two different levels of oxygen saturation are shown. (b) The change in the upper-state lifetime of the dye measured with PALT for different blood oxygen saturations (R sq value: 0.99)……....83

Figure 6.1: Schematic illustration of the PAI setup…….....95

Figure 6.2: Synthesis of targeted Coomassie Blue-loaded nanoparticles, through a reverse nano-emulsion polymerization process followed by the attachment of the tumor-homing F3 peptide..98

Figure 6.3: Characterization of the Coomassie Blue-attached nanoparticles. (a) The size distribution of the nanoparticles in aqueous medium, as obtained from the DLS reading. (b) SEM image of the nanoparticles, (c) Normalized extinction (absorption + scattering) spectrum of the nanoparticles and the free dye. The nanoparticle spectral curve does not go to the baseline due to significantly higher scattering, compared to the free dye. (d) The 9L glioma cell and MCF7 cell targeting efficiency of the F3-attached nanoparticles. The dye stains the cells, irrespective of the cell line, due to its high affinity towards the proteins. However the F3-targeted nanoparticles stain the 9L cells significantly more than the MCF7 cells. Note that the non-targeted nanoparticles stain the targeted cells (9L) significantly less, while for the non-targeted cells (MCF7) both targeted and non-targeted particle staining is equally poor, as expected……99

Figure 6.4: (a) and (b): Photographs of phantoms #1 (concentration of nanoparticle (clockwise): 0.5 mg/mL, 0.25 mg/mL, 0.2 mg/mL and 0.125 mg/mL) and #2 (concentration of nanoparticles (anti-clockwise): 0.1 mg/mL, 0.04 mg/mL, 0.02 mg/mL and 0.01 mg/mL) , respectively. (c) and (d): PAI images of the phantoms #1 and #2, respectively (taken with an amplifier gain of 35 db and 45 db, respectively) (scale 3 cm x 3 cm)…….101

Figure 6.5: (a) Photograph of a rat brain with three embedded tumors. (b) PAI image of the brain (scale 2 cm x 2 cm)……..103

Figure 6.6: (a) Photograph of a rat brain containing a tumor treated with nanoparticles. (b) PAI image of the sample (scale 2 cm x 2 cm). (c) Photograph of the control tumor in the brain containing no contrast agent. (d). PAI image of the sample (scale 2 cm x 2 cm). We do not see any signal from the control tumor……107

Abstract

Photoacoustics and Fluorescence based Nanoprobes towards Functional and Structural Imaging *in vivo*

Imaging of chemical analytes and structural properties related to physiological activities within biological systems is of great bio-medical interest; it can contribute to the fundamental understanding of biological systems and can be applied to the diagnosis and prognosis of diseases, especially tumors. The work presented in this thesis focuses on the development and application of polymeric nanoprobe aided optical imaging of chemical analytes (Oxygen, pH) and structural properties in live cells and animal models. To this end, specific nanoprobes, based on the polyacrylamide nanoplatform, bearing both appropriate targeting functionalities, and high concentrations of sensing and contrast agents, have been developed. The nanoprobes presented here are biodegradable, biocompatible and non-toxic, rendering them safe for *in vivo* use. Furthermore the nanoprobes are designed to have variable optical properties that are dependent on the local concentration of the specific analyte of interest. Optical imaging techniques that are particularly suited for deep tissue applications, such as two-photon fluorescence and photoacoustics, were applied for non-invasive real-time imaging and sensing in cancer cells, tumor spheroids and animal models. Our results demonstrate that this technique enables high sensitive detection of chemical analytes with a sensitivity of <5 Torr for oxygen and <0.1 pH units *in vivo*, which is better than the currently available *in vivo* functional imaging techniques. This non-invasive and non-ionizing, yet low cost, method will enable morphological and functional evaluation across any tissue, with both high spatial and temporal resolution but without eliciting short- or long-term tissue damage. Currently no gold standard exists for such

functional imaging. The approach presented here can be used for early detection and diagnosis of tumors, as well as for monitoring the progression of disease and therapy. This technique will also enable observing phenomena at the cellular level *in vivo* that would lead to a better understanding of the pathophysiology of diseases as well as the disease onset, progression, and response to therapy.

Chapter 1

Introduction

Imaging of chemical analytes and physical properties that are related to physiological activities within any biological system is an important and challenging task. Due to its potential applicability to disease diagnosis and prognosis, real-time, spatially-resolved, chemical and physical information is of significant medical interest. For instance, tumors are often in altered metabolic states that produce abnormal chemical and physical environments (e.g., local pH, oxygen, glucose and temperature) [1-2]. Tumors often outgrow their vasculature oxygen supply which generally leads to an inadequate oxygen supply to the core. This causes a lack of oxygen concentration in the core of the tumors and is known as hypoxia. This condition has been shown to cause tumor aggressiveness, local recurrence and metastasis. [3-4]. More importantly they cause resistance to various kinds of therapy, such as radiation therapy, which utilizes ionizing radiation to damage the double stranded DNA; chemotherapy, which targets the proliferation of cells and photodynamic therapy, which involves creation of photon mediated singlet oxygen species to kill cancer cells[5-6]. . Thus tumor hypoxia is one of the biggest reasons for the failure of cancer therapy. Furthermore, the excess metabolism of ATP and production of lactic acid, especially in the hypoxic region where most of the cells undergo anaerobic metabolism also leads to a lower pH level [2]. This lower pH level in cancer tissues has also been shown to cause resistance to drug delivery and therapy. On the other side, the lower pH is also exploited by many drug delivery systems where the drug capsules are designed to release their contents at a

specific pH. An exact knowledge of the chemical composition in the tissues will lead to a better understanding of the disease, and its treatment options, for each individual patient. A quantitative assessment of such cancer characteristics, *in vivo*, will contribute toward a more accurate diagnosis and also toward a more optimal treatment. Abnormal chemical pH levels are also observed during the body's stress conditions, such as inflammation, high exercise levels, interruption of normal blood supply, or bio-chemical shock arthritis , open wounds etc. [7, 8]. Some techniques based on Magnetic Resonance Imaging and spectroscopy, Positron Emission tomography, luminescence and micro-electrodes have been used for such purpose but unfortunately no gold standard methods currently exist for the detection of chemical levels inside the body [9-14].

Nanotechnology has become a powerful tool to develop bioimaging modalities that are more reliable and effective than the existing ones [15-16]. Nanotechnology facilitates the design of multi-functional and multi-analyte diagnostic platforms that may define early stage changes or progression of diseases, such as cancer, by identifying unique biological molecules, chemical substances and physical structures, or other aspects not addressable with current imaging technologies, such as enhanced contrast agents [17]. In the past decade, there has been significant progress in the development of nanoparticle sensors for evaluation of cellular events [18]. These nanosensors can also be engineered so as to observe phenomena at the molecular level *in vivo*, allowing better understanding of the pathophysiology of diseases as well as the disease's onset, progression, and response to therapy.

Described in this thesis is the development and application of appropriate nanoprobes based on polymer nanoplatforms, containing high amounts of sensing and contrast agents for the

purpose of *in vivo* imaging and sensing. The use of appropriate nanoprobes may avoid potential problems of traditional molecular probes (cytotoxicity, interferences from biological molecules, non-specificity etc).

This includes developing suitable polyacrylamide based nanoprobes that contain high amounts of sensing and contrast agents, yet are biodegradable, biocompatible and non-toxic, rendering them safe for *in vivo* use. The properties of the polymer matrix, such as its porosity, surface charge, particle size, hydrophobicity of the core etc., can be controlled with respect to the molecular agents being used. The surface of these nanoprobes can be further modified by attaching tumor targeting moieties, for active targeting to any specific type of tumor. The nanoprobes can be designed to have variable optical properties that are dependent on the local concentration of the specific chemical analyte of interest. The small pore size of the polymer matrix limits the interactions of the molecular agents encapsulated inside, with the proteins present in plasma and cells, but allows free flow of ions like H^+, Ca^{2+} and small molecules like O_2, making them efficient chemical sensors. This also eliminates the need for calibrating the nanoprobes *in vivo*; on-bench calibration is sufficient [17, 18].

Several imaging and sensing technologies have been utilized for medical applications. Some of the most commonly utilized imaging techniques include Magnetic Resonance Imaging (MRI) and spectroscopy (MRS)[9, 10, 14], X-Ray tomography [19], Positron Emission Tomography (PET)[11-12], ultrasound [20] and optical techniques such as fluorescence[13], photoacoustics[21], diffused optical tomography[22], near infrared scattering spectroscopy and tomography (NIRS) [23]. All these techniques have some distinct advantages but also come with several limitations.

For example PET is capable of qualitatively distinguishing changes in oxygenation and pH level, using indirect methods based on monitoring probe oxidation and cellular uptake of probes throughout the tumor tissue; however these processes are cell dependent [11-12]. PET also involves harmful ionizing radiations and therefore is not suitable for repeated imaging and image-guided interventions. MRI has also been utilized for functional imaging, especially of hypoxia, by monitoring the oxygen dependent spin lattice relaxation time and also by indirect methods such as measuring the tumor perfusion, and using contrast agents followed by extensive modeling [9-10]. These methods have a relatively low oxygen sensitivity of ~10 Torr and a temporal resolution of minutes [14]. The best achievable spatial resolution for functional imaging is ~100 μm for MRI and ~1 mm for PET. A more sensitive and widely used technique is fMRI (functional MRI) for measuring the oxygenation of blood, but it cannot be applied to tumor tissues devoid of blood. Both these methods, especially PET, are quite expensive in terms of price and space. The most commonly used method for chemical measurements employs microelectrodes; they however are invasive in nature and cannot provide complete spatial information. For the purpose of structural imaging ultrasound has become a highly utilized imaging method, from cardiology to oncology, but its sensitivity may still not suffice for reliable detection of cancer, especially in the early stages. The challenge in continuing proper assessment of the tumor and its microenvironment, so as to help determine the proper course of therapy and monitor its efficacy, still remains unaddressed. Currently no gold standard exists for functional imaging.

Thus there is a real need for a less expensive, more capable and reliable imaging tool. Optical techniques offer a relatively safer, faster and cheaper method of imaging and sensing with

very high resolution. However most of the optical techniques are limited by the optical tissue penetration depth due to soft tissue scattering and absorption. To improve the optical tissue penetration depth generally NIR light based techniques such as two photon fluorescence, NIR fluorescence, NIRS tomography etc as well as the hybrid photoacoustic imaging technique are regularly used. Nanotechnology when realized with the low-cost, yet powerful, *in vivo* optical imaging techniques such as two photon fluorescence and photoacoustics, nanoprobe facilitated imaging and sensing will reduce time, uncertainty and expenditures on the diagnosis and treatment of diseases.

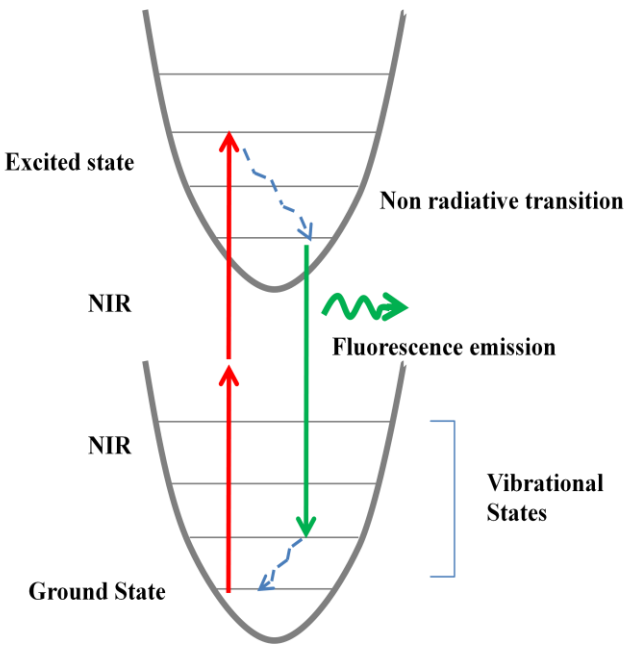

Fig 1. The Jablonski diagram demonstrating the two photon fluorescence. Electrons are excite from the ground state to the excite state via short lived intermediate states by simultaneous absorption of two Near Infrared (NIR) photon.

Two photon fluorescence

The phenomenon of two photon excitation was first predicted by Maria Goppert-Mayer in 1931 [24]. Since then this technique has evolved significantly and is now very widely used

for several applications. The first two photon microscopy was demonstrated by Webb et. al. in 1990 [25].

Two photon fluorescence is a nonlinear optical process that involves simultaneous absorption of two low energy photon followed by emission of a higher energy photon (as shown in Fig 1). This is a second order nonlinear process and so the absorption by each molecule per unit time is proportional to the square of the incident light intensity (I) and the absorption cross section (δ) which has an unit of Goeppert-Mayer (GM) and is given as 1 GM is 10^{-50} cm^4 s $photon^{-1}$. The number of photons absorbed $N_{abs}(t)$ is given by: [26-28]

$$N_{abs}(t) = \int_V C(r,t) I^2(r,t) \delta dV \quad (1)$$

Where C(r, t) is a factor that takes into account the temporal and spatial saturation and photobleaching of the molecule. It can be considered a constant for simple cases. The light intensity distribution '*I'* can be broken down into two components the spatial '*S(r)*' and temporal '*I(t)'* components: $I\,(r,t) = S(r)I(t)$.

Thus $N_{abs}(t)$ can be written as

$$N_{abs}(t) = C(r,t) I^2(t) \delta \int_V S^2(r) dV \quad (2)$$

The amount of two photon fluorescence photons emitted, which depends on the number of absorbed photons is given by

$$F(t) = {}^1/_2\, \eta_2 N_{abs} \quad (3)$$

Where η_2 is the fluorescence quantum efficiency.

The time averaged two photon fluorescence emission flux, which is essentially measured by the CCD is give by:

$$\langle F(t)\rangle = {}^{1}/_{2}\,\eta_2 C(r,t)\langle I^2(t)\rangle \delta \int_V S^2(r)dV \qquad (4)$$

For most applications using diffraction limited lens for focusing the spatial intensity distribution can be assumed to be an extension of the paraxial form of the normalized intensity point-spread function. [26]

Two photon fluorescence has several advantages over other optical methods such as higher penetration depth (~mm) due to the utilization of NIR wavelengths. They also have a higher signal to noise ratio, low autofluorescence and low photodamage. The quadratic dependence for excitation also leads to automatic cross-sectioning of the sample and leads to better resolution.

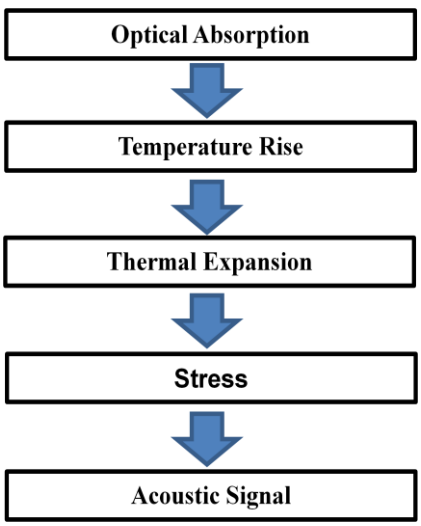

Fig 2. Flowchart demonstrating the mechanism of Photoacoustics.

Photoacoustics

Photoacoustics is a hybrid optical imaging technique that combines the merits of optics and ultrasound [21, 29-31]. This technique involves the generation of acoustic signal from the nanoprobes or any contrast agent after light irradiation. When irradiated with the proper frequency of light, the probes absorb the photons and reach an excited state. They then go back to the ground state by the process of non radiative transition by releasing heat in the process. The temperature rise is generally of the order of milli Kelvins. This change in temperature leads to a stress and this gives rise to the acoustic signal typically in the range 1-50 MHz, which can be detected using a transducer. This is summarized in Figure 2. By monitoring the acoustic signal response from the chemically sensitive probes it is possible to extract information about the chemical composition in its local microenvironment. They can also be used for structural imaging by monitoring the local distribution of the nanoprobes.

The pressure created in at a particular point in a medium due to absorption of photons is given by [29]

$$P_o = (\beta c^2 / C_p)\mu_a F \tag{5}$$

So the pressure created generally depends on the following parameters:

β: Isobaric volume expansion coefficient

c: speed of sound in the medium ~1.5mm/μs

C_p: Specific heat (J/K Kg)

μ_a: Absorption Coeff (cm^{-1})

F: Light fluence (J/cm^2)

The pressure at position '**r**' and time '**t**', due to generation of heat in a homogeneous liquid like medium , is given by the following wave equation[21, 29]:

$$\nabla^2 p(r,t) - \frac{1}{c^2}\frac{\partial^2}{\partial t^2} p(r,t) = -\frac{\beta}{C_p}\frac{\partial}{\partial t} H(r,t) \tag{6}$$

Where, H: Thermal energy deposited by the EM radiation per unit time and per unit volume

β: Isobaric volume expansion coefficient

C_p: Specific heat (J/K Kg)

c: Velocity of sound in that particular medium.

Solution to this equation 6, using the free space Green's function can be written as:

$$p(r,t) = \frac{\beta}{4\pi c}\iiint \frac{d^3 r'}{(r-r')}\frac{\partial H(r',t)}{\partial t}\Big|_{t=|r-r'|/c} \tag{7}$$

The heating function H can be broken into two parts: spatial absorption function and temporal illumination.

$$H(r,t) = A(r) I_e(t) \tag{8}$$

Thus the integral can be assumed to be the convolution between the temporal profile of the illumination and acoustic wave form $p_\delta(\mathbf{r},t)$ that is excited by an infinitesimally short pulse $\delta(t)$.

$$p(r,t) = \int_{-\infty}^{+\infty} I(t-\tau)\, p_\delta(r,\tau) d\tau \tag{9}$$

Where $p_\delta(\mathbf{r},t)$ is:

$$p_\delta(r,t) = \frac{\partial}{\partial t}\left[\frac{1}{4\pi} \iint_{|r-r'|=ct} p_o(r) d\Omega\right] \tag{10}$$

Where $p_o(r) = \Gamma A(r)$, $\Gamma(r)$ Is gruneisen coeff and is given as $(\beta c^2 / C_p)$

p_δ is the measured data and can be obtained from the sonogram, as shown in Figure 3 and p_o is the pressure at the initial source . The spatial distribution of the pressure generated ($\mathbf{p_o}$) can be obtained by using different image reconstruction algorithms such as Radon transformation, Back projection etc.

The main advantage of photoacoustics over other conventional optical imaging is the deep tissue penetration. Due to the single passage of light this technique enables imaging upto a few cm's in tissues. This method also has a high sensitivity and good resolution, comparable to ultrasound.

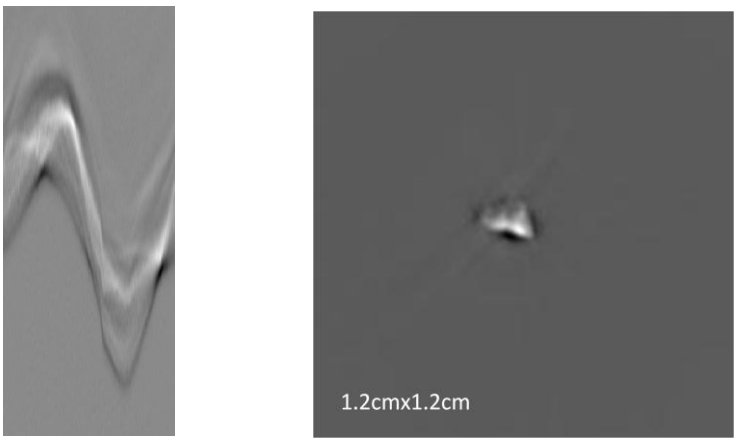

Fig. 3 (a) Sonogram of a triangular piece of rubber. The sonogram is constructed from p_δ (b) The photoacoustic image of the rubber (obtained from the sonogram by using back projection algorithm in this case).

Outline of dissertation

The focus of this thesis is on development and application of nanoprobes that can be used for chemical sensing and structural imaging using optical techniques. Broadly, the specific aims are as follows: 1.Development of nanoprobes for (i) pH sensing, (ii) Oxygen sensing (iii) Structural imaging and 2.Application of the nanoprobes to live cells and animals.

The second chapter describes the development of pH sensitive, polyacrylamide based, nontoxic and biodegradable nanoprobes, which operate in the near infrared (NIR), by exploiting their nonlinear fluorescence. NIR light is particularly suitable for *in vivo* optical imaging because of deeper penetration depth and high signal to noise (S/N) ratio. The nanoprobes utilize a pH sensitive fluorescent dye, encapsulated in a specially designed polyacrylamide (PAA) matrix. They were employed to map the intracellular pH of live cells (Glioma-9L) and micro-tumors (Cervix cancer-HeLa), also known as spheroids, using two photon microscopy. Both targeted and non-targeted nanoprobes were used for the purpose of

intracellular mapping. Targeting was achieved by attaching the tumor targeting F3 peptide (PKAARALPSQRSRPPEKAKKPPDKPAPEKKKC) onto the surface of the nanoprobes. The intracellular measurements suggest that the non-targeted nanoprobes are mostly trapped in acidic endosomes and lysosomes, whereas the F3 peptide targeting enables them to escape/avoid these acidic compartments [32].

The technique of using nonlinear fluorescence, for pH sensing, showed good results but had an inherent drawback - low fluorescence output signal. In the third chapter this problem is addressed using a novel method by developing a hybrid polyacrylamide-based nanoprobe containing a noble-metal nanocore, citrate molecules and pH sensitive fluorescent dye. The presence of the metal core can enhance the fluorescence from the sensor dyes through various mechanisms, arising due to its non-linear properties, surface plasmons and resonance energy transfer. The method preserves all the advantages of two photon microscopy and enhances the fluorescence signal by twenty times. It enabled us to demonstrate fluorescence enhancement in live cells, for the first time ever, as all previously developed fluorescence enhancement techniques could only be used in solutions *in vitro*. The fluorescent nanoparticles are extremely sensitive to pH, and they enable high resolution imaging with excellent S/N ratio. However, they have limited *in vivo* imaging ability, due to low tissue penetration depth (~ mm) of the excitation and emission wavelengths [33].

The fourth chapter focuses on utilizing a hybrid photonic imaging technique, photoacoustic imaging (PAI), for the purpose of pH sensing. Nanoprobes with a hydrophobic core containing a pH sensitive dye were used to accurately measure the pH level *in vivo* by performing experiments on a rat joint model, with a sensitivity of less than 0.1 pH units. The

ability of the hydrophobic polyacrylamide matrix to shield the molecular dye from proteins in the plasma, as well as preventing the dye from leaching out, is also demonstrated.

Described in the fifth chapter is the development of a lifetime-based photoacoustic system for detection of the local oxygen pressure *in vivo*. The lifetime based photoacoustic technique for the measurement of oxygen *in vivo was performed* using an oxygen sensitive probe containing a porphyrine core and dendrimer covering, enabling real time quantification of blood oxygenation. The results derived from the main artery in the rat tail indicated that the lifetime of the dye, quantified by the photoacoustic technique, shows a linear relationship with the blood oxygenation level in the targeted artery. The upper state lifetime of the dye in the artery changed from 45 microseconds when blood oxygenation was 94% to 158 microseconds when blood oxygenation was 77%, demonstrating good sensitivity as well as dynamic range [34].

The sixth chapter describes a novel method to delineate brain tumors, using a highly sensitive photoacoustic imaging technique that is enhanced by tumor-targeting blue nanoprobes serving as both visible and PAI contrast agent. Experiments on phantoms and on rat brains, *ex-vivo,* demonstrate the high sensitivity of the enhanced photoacoustic imaging, delineating the tumor containing contrast agent at a concentration much lower than needed for visualization by the naked eye. The limit of detection of the system for the nanoparticles is about 0.77 μgram/ml in water (equivalent to 0.84 μM CB dye). The present study suggests that photoacoustic imaging, when used with strongly optical absorbing contrast agents, could facilitate cancer surgery intra-operatively by revealing the distribution and extent of the tumor at relatively low, and thus safe, doses [35].

The seventh and final chapter discusses a summary of the work presented here in this thesis and also the future directions. Possible applications of the technique demonstrated in the thesis are also discussed, as well as different methods to further improve the systems and nano-platforms.

The results presented in this thesis demonstrate the feasibility of nanoprobe aided structural imaging as well as chemical sensing *in vivo* with extremely high sensitivity. The nanoprobes provide an efficient, economic and reliable method for tumor diagnostics which has the potential to be applied clinically. These nanoprobes can also be tailored to deliver drugs, enabling therapy. Using such a single nanoprobe that enables multiple chemical and physical imaging functions as well as therapy, healthcare practitioners would not have to perform multiple examinations so as to generate complete diagnostics, followed by diagnostics based therapy, and by monitoring its effectiveness. It could thus also lead the way towards personalized therapy.

References

1. Vaupela P, Harrison L, Tumor Hypoxia: Causative Factors, Compensatory Mechanisms, and Cellular Response,The Oncologist, 2004, 9: 4-9.

2. Tannock IF, and Rotin D, Acid pH in Tumors and Its Potential for Therapeutic Exploitation, Cancer Res 1989, 49:4373-4384.

3. Facciabene A, Peng X, Hagemann IS, Balint K, Barchetti A, Wang LP, Gimotty PA, Gilks CB, Lal P, Zhang L & Coukos G, Tumour hypoxia promotes tolerance and angiogenesis via CCL28 and T_{reg} cells, *Nature 2011,* 475; 226–230.

4. Wilson WR, Hay MP, Targeting hypoxia in cancer therapy, *Nature Reviews Cancer* 2011, 11; 393-410.

5. Trédan O , Galmarini CM, Patel K, Tannock IF, Drug Resistance and the Solid Tumor Microenvironment, J Natl Cancer Inst 2007, 99: 1441–54.

6. Brown JM, Wilson WR, Exploiting tumor hypoxia in cancer treatment, *Nature Reviews Cancer* 2004, 4: 437-447.

7. Andersson SE, Lexmüller K, Johansson A, Ekström GM, Tissue and intracellular pH in normal periarticular soft tissue and during different phases of antigen induced arthritis in the rat, J Rheumatol. 1999 Sep;26(9):2018-24.

8. Schneider LA, Korber A, Grabbe S, Dissemond J, Influence of pH on wound-healing: a new perspective for wound-therapy?, Arch Dermatol Res. 2007 Feb;298(9):413-20 .

9. Liu S, Shah SJ, Wilmes LJ, Feiner J, Kodibagkar VD, Wendland MF, Mason RP, Hylton N, Hopf HW, Rollins MD, Quantitative tissue oxygen measurement in multiple organs using 19F MRI in a rat model, Magnetic Resonance in Medicine, 2011, 66;1722–1730.

10. Gallagher FA, Kettunen MI, Day SE, Hu DE, Ardenkjær-Larsen JH, Zandt R, Jensen PR, Karlsson M, Golman K, Lerche MH, Brindle KM, Magnetic resonance imaging of pH *in vivo* using hyperpolarized ^{13}C-labelled bicarbonate, *Nature* 2008, 453; 940-943.

11. Imam SK, Review of Positron Emission Tomography Tracersfor Imaging of Tumor Hypoxia, Cancer Biotherapy and Radiopharmaceuticals 2010, 25, 3.

12. Vāvere AL, Biddlecombe GB, Spees WM, Garbow JR, Wijesinghe D, Andreev OA, Engelman DM, Reshetnyak YK, Lewis JS, A novel technology for the imaging of acidic prostate tumors by positron emission tomography, Cancer Res. 2009,69(10):4510-6.

13. Helmlinger G, Yuan F, Dellian M, Jain RK, Interstitial pH and pO_2 gradients in solid tumors *in vivo*: High-resolution measurements reveal a lack of correlation, *Nature Medicine* 1997, 3, 177 - 182.

14. Giraudeau C, Djemaï B, Ghaly SOA, Robert P, Port M, Robic C, Bihan DL, Lethimonnier F, Valette J, High sensitivity 19F MRI allows dynamic biodistribution study and oxygen tension mapping at pharmaceutical doses of a PFOB emulsion in the mouse reticuloendothelial system, *Proc. Intl. Soc. Mag. Reson. Med.* 2011, 19; 1703.

15. Minchin RF, Darren J, Martin DJ, Minireview: Nanoparticles for Molecular Imaging—An Overview. *Endocrinology* 2010, 151: 474–481

16. Orringer DA, Koo YE, Chen T, Kopelman R, Sagher O, Philbert MA, Small solutions for big problems: The application of nanoparticles to brain tumor diagnosis and therapy. *Clin. Pharmacol. Ther.* 2009, *85*: 531–534 .

17. Koo Lee Y-E, Orringer DA, Kopelman R. "Polymer-based nanosensors for medical applications", In Broz P., ed., Polymer-based Nanostructures: Medical Applications, 2010, pp.333-353

18. Koo Lee YE, Smith R, Kopelman R, Nanoparticle PEBBLE sensors in live cells and *in vivo*. *Annu. Rev. Anal. Chem.* 2009, *2*: 57–76.

19. Paulus MJ, Gleason SS, Kennel SJ, Hunsicker PR, and Johnson DK, High Resolution X-ray Computed Tomography: An Emerging Tool for Small Animal Cancer Research, *Neoplasia*. 2000 January; 2(1-2): 62–70.

20. Mittelstaedt CA, Ultrasound as a Useful Imaging Modality for Tumor Detection and Staging, *Cancer Research* 1980 40, 3072-3078.

21. Xu M and Wang LV, Photoacoustic imaging in biomedicine, *Rev. Sci. Instrum.* 2006, 77, 041101.

22. Enfield LC, Gibson AP, Hebden JC and Douek M, Optical tomography of breast cancer—monitoring response to primary medical therapy, *Target Oncol.* 2009, 4(3):219-33.

23. Nioka S, Chance B, NIR spectroscopic detection of breast cancer, *Technol Cancer Res Treat.* 2005, 4(5):497-512.

24. Goeppert-Mayer M, Über Elementarakte mit zwei Quantensprüngen, *Ann Phys* 1931, 9 (3): 273–95.

25. Denk W, Strickler JH and Webb WW, Two-photon laser scanning fluorescence microscopy. Science 1990, 248: 73–76

26. Xu C and Webb WW, Measurement of two-photon excitation cross sections of molecular fluorophores with data from 690 to 1050 nm, J. Opt. Soc. Am. B 1996, 13(3); 481 .
27. Makarov NS, Drobizhev M, and Rebane A, Two-photon absorption standards in the 550-1600 nm excitation wavelength range, Optics Express, 2008, 16 (6); 4029.

28. Prasad P. N., Introduction to BioPhotonics, Wiley Interscience, 2003.

29. Wang L. V. and Wu H-I, Biomedical Optics: Principles and Imaging, Wiley Interscience, 2007.

30. Wang X, Pang Y, Ku G, Xie X, Stoica G, Wang LV: Noninvasive laser-induced photoacoustic tomography for structural and functional in vivo imaging of the brain. *Nat Biotechnol* 2003, 21(7):803-806.

31. Wang X, Pang Y, Ku G, Stoica G, Wang LV: Three-dimensional laser-induced photoacoustic tomography of mouse brain with the skin and skull intact. *Opt Lett* 2003, 28(19):1739-1741.

32. Ray A, Koo YEL, Epstein T, Kim G and Kopelman R, Two-photon nano-PEBBLE sensors: subcellular pH measurements, *Analyst* 2011, 136; 3616-3622.

33. Ray A, Koo YEL , Kim G and Kopelman R, Two-photon fluorescence imaging super-enhanced by multi-shell nano-photonic particles : Application to subcellular pH, *Small* 2012, 8(14):2213-21.

34. Ray A, Raijan J, Koo YEL, Wang X and Kopelman R, Lifetime based photoacoustic oxygen sensing *in-vivo, Journal of Biomedical Optics* 2012, 17 (5); 057004.

35. Ray A, Wang X, Koo Lee YE, Hah HJ, Kim G, Chen T, Orringer DA, Sagher O, Liu X and Kopelman R, Targeted blue nanoparticles as photoacoustic contrast agent for Brain tumor delineation, *Nano Research* 2011, 4(11); 1163-1173.

Chapter 2

Development of two-photon fluorescent nanoprobe: Subcellular pH Measurements

This chapter has been adapted with minor modifications from the following published article:

A. Ray, Y.E Lee Koo, T. Epstein, G. Kim and R. Kopelman, "Two-photon nano-PEBBLE sensors: subcellular pH measurements" *Analyst*, Vol. 136, 3616-3622 (2011)

Introduction

Intracellular pH plays a critical role in many aspects of cell physiology. Many physiological processes, such as protein synthesis, RNA & DNA synthesis, ion channel conductivity, ion transport, cell cycle control, cellular proliferation, cell fertilization, cell volume regulation, neurotransmitter reuptake, muscle contraction, and apoptosis, are controlled by the pH of the cell [1-3]. Small changes in the intracellular pH can drastically affect these processes. Also the pH of the microenvironment of tumor tissues is characterized by significantly low pH. Thus pH can also be used to distinguish between normal and tumor tissue in-vivo [4]. Of the popular techniques to measure the intracellular pH, including 31P-NMR spectroscopy, ion-sensitive microelectrodes and metal nanoparticles, pH indicator dyes seem to be highly attractive, due to their higher sensitivity and ability for continuous monitoring of rapid kinetic pH changes [5-6]. The pH response of these dyes in the form of changes in their upper state lifetime [7-8], or their absorption/emission spectrum or intensity [9-10], is exploited to accurately measure the pH.

The ratiometric fluorescence approach, which involves taking the ratio between two emission peaks of a

single fluorophore, or of a pair of fluorophores (of which at least one is sensitive to the pH) is used for precise determinations of the pH value. The ratiometric approach reduces the errors due to variation in the dye concentration, optical path length, light intensity and photobleaching (for a single dye or if the two dyes have similar photobleaching rates). However, a potential disadvantage is that the (free) dye molecule can interact with cell components, such as proteins, to give significant errors. For example BCECF,(*2',7' - Bis - (2 - carboxyethyl) - 5 - (and - 6) – carboxyfluorescein),* which is one of the most commonly used pH indicator dyes, can bind to proteins due to its high charge, resulting in a large spectral shift [11]. This requires the calibration of the dye inside cells. Some of the pH-sensitive dyes have also been shown to interfere in the proper functioning of the cell, such as inhibiting calcium-ATPase [12], etc. Furthermore, dye's such as lysosensor, can exhibit alkalization effect, which severely limits the time of incubation and time-scale of the kinetic studies. Another factor that often limits the time scale of measurement is the tendency of the dye to leak out of the cell, or to be sequestered in one of its components. Some dyes are also membrane impermeable and cannot be used for intracellular measurements, unless they are invasively forced into the cells.

Polymer based nanoprobes, were developed in our lab for the purpose of eliminating some of the undesirable effects of using free dye [13-14]. The dye indicators, sensitive to specific analytes, are encapsulated within the pores of the inert polymer matrix of the nanoprobes. The small size of the pores of the polymer matrix limits the interactions of the indicator dyes with the proteins and cell organelles, but allows free flow of ions like H^+, Ca^{2+}, K^+, Cu^{2+}, etc [14-16]. This eliminates the need for calibrating the sensors in vivo; on-bench calibration is sufficient. The nanoprobes are also made to be biocompatible, chemically and physically noninvasive to cells, and can be retained in the cytoplasm for days [17-20]

It should be noted that fluorescent intracellular measurements suffer from strong auto-fluorescence. Recently, several different approaches have been taken so as to avoid such problem. These include development/use of near-infrared (NIR) molecular probes, MagMOON's (Magnetically-modulated optical nanoprobes) or two-photon excitable molecular probes [21-22]. The MagMOON's are made of PEBBLEs half-coated with magnetic metal, and their rotation under a rotating magnetic field, creates a blinking effect, allowing easy background subtraction while imaging [22-23]. However, the MagMOONS have, so-far, been rarely applied for intracellular measurements, due to size-related difficulties. Two photon excited fluorescence is a nonlinear optical process in which two photons, typically in the infrared region, are absorbed and fluorescence occurs at a lower wavelength (higher frequency), in the visible region. The nonlinear excitation by near infrared light significantly reduces both autofluorescence and photodamage to the cells. Since the exciting wavelength is considerably longer than the fluorescent wavelength, they can be easily separated out, leading to a high signal over noise ratio. Due to the nonlinear nature of the excitation, it is highly localized and results in higher spatial resolution on the microscope. Most importantly, photobleaching is minimized due to the use of low energy photons and highly localized excitation [24]. Thus the use of two photon fluorescence microscopy enables highly accurate and spatially localized measurement. Interestingly, there are only a few reports that look into two-photon pH response of dyes based on their changes in either the spectrum [21, 25] or the lifetime [8]. Actually, several single-photon NIR probes for pH sensing have been developed [26-27]. Although these NIR probes have much higher absorbance cross sections, they have few of the other advantages of the two-photon fluorescence technique.

Here we demonstrate for the first time, ratiometric fluorescent pH sensing nanoprobes that are based on two photon excitation. The nanoprobes contain a pH sensitive dye, 8-Hydroxypyrene-1,3,6-trisulfonic

acid (HPTS), encapsulated in a polyacrylamide matrix. We also compare the two-photon sensitivity of HPTS-NP with BCECF-NP and lysosensor-NP. The HPTS-NPs are found to be most suitable for two-photon pH measurement, compared to the other two. The nanoprobes have an average size of 68 nm and contain about 0.5% dye by weight. HPTS is a highly sensitive, water soluble pH sensitive dye with low toxicity. It is a membrane impermeant dye and cannot be used for intracellular measurements in its free form, without the use of an invasive procedure. Thus there exist only a few reports on intracellular pH measurements with HPTS [28-29]. Also, all the previous measurements were performed by monitoring the change in the single photon fluorescence emission/absorption spectrum. Invasive techniques such as microinjection, electroporation or scrape loading, which might be harmful to the cells, were previously used to deliver the free dye molecules into the cells [6]. The nanoprobes can be non-invasively delivered into the cells by nonspecific or receptor mediated endocytosis. We use both the targeted and unmodified HPTS-NPs to study the 9L rat glioma cells. We obtain an intracellular pH value of 7.1 for the 9L cells. The results demonstrate that, combining pH sensitive nanoparticles with specific targeting that allows intracellular access to any probe, yet doesn't interact with the contents of intracellular organelles, and with the advantages of two photon microscopy, is attractive and promising.

Experimental

Chemicals and materials

Acrylamide, methylene-bis-acrylamide (MBA), dioctyl sulfouccinate (AOT), Brij 30, hexane, ammonium persulfate (APS), N,N,N',N'-tetramethyl ethylenediamine (TEMED), N-(3-dimethylaminopropyl)-N'-ehtylcarbodiimide hydrochloride (EDC), bovine serum albumin (BSA) (30% w/v) and L-cysteine were all acquired from Sigma-Aldrich (St. Louis, MO). 3-

(aminopropyl)methacrylamide hydrochloride salt (APMA) was obtained from Polysciences Inc. (Warrington, PA). Ethanol (95%) was acquired from Decon labs, Inc (King of Prussia, PA). N-hydroxysulfosuccinimide (sulfo-NHS) and succinimidyl 4-[N-maleimidomethyl]cyclohexane-1-carboxylate (SMCC) were acquired from Pierce Biotechnology (Rockford, IL). HPTS and Lysosensor was obtained from Invitrogen (Carlsbad, CA). BCECF was acquired from AnaSpec (San Jose, CA). F3-Cys peptide (PKAARALPSQRSRPPEKAKKPPDKPAPEKKKC) were purchased from SynBioSci (Livermore, CA). The buffer soultions were obtained from Fischer Scientific. All solutions were prepared in 18-MΩ water purified in a Barnstead 1 Thermolyne Nanopure II system. All the chemicals and materials were used as received.

Preparation of the nanoprobes

Thenanoprobes containing HPTS, BCECF and Lysosensor were prepared using micro-emulsion and radical polymerization technique, as described previously [13]. The monomer solution contained 8.6 mmol acrylamide, 0.25mmol APMA, 1.2 mmol MBA and 19 mmol HPTS dissolved in 1.6 ml Phosphate buffer at pH 7.4. This solution was then added to a 36 ml hexane solution containing 6.85 mmol Brij-30 and 2.88 mmol dioctyl sulfosuccinate. The two solutions were emulsified by stirring them for 20 mins under an inert atmosphere. The reaction was initiated by using 0.54 mmol TEMED and 28 μmol APS, freshly prepared 10% (Weight/Volume) in water. The solution was further stirred for two hours to complete the polymerization. Hexane was removed by rotary evaporation, using Rotavapor-R (Brinkmann Instruments), and then suspended in ethanol. The surfactants and excess dye were removed by washing the particles five times in ethanol and five times in water for over two days, in an Amicon ultra-filtration cell (Millipore Corp., Bedford, MA), using a 300 kDa filter, and then freeze-dried with a

5L ModulyoD freeze dryer (ThermoFisher Scientific).

F3 Peptide conjugation: The F3 peptide is used to target the nucleolin that is over-expressed in tumor vasculature and some tumor cells such as 9L glioma[30]. F3 peptides were conjugated to the surface of the nanoprobes, for specific targeting of tumor cells. The freeze-dried PAA nanoprobes (50 mg) were dissolved in pH 7.4 PBS (2.5 mL), treated with SMCC (2 μmol) and stirred at room temperature for 30 min. The reaction mixture was then subjected to thorough washings, to remove any unreacted ligands, and concentrated to ~20 mg/mL. F3 peptide tagged cystein, F3-Cys peptides (0.06 μmol) were added to the concentrated nanoprobe solution and gently stirred overnight (>8 hours), at room temperature, and treated with L-cysteine (1 μmol) for another 2 hours. The resultant solution was thoroughly washed with water and PBS in an Amicon cell and then freeze dried.

Nanoprobe Characterization

Particle size and Zeta Potential measurement

The particles were diluted in water at a concentration of 1mg/ml and the particle size distribution in aqueous solution and the Zeta potential were measured by dynamic light scattering (DLS), using a Beckman-Coulter DelsaNano C Zeta potential/submicron size analyzer.

Dye concentration

The amount of dye encapsulated in the nanoprobes was determined by comparing the fluorescence from a known concentration of nanoparticles in water to the fluorescence signal obtained from a set of known concentration of dye in water. The fluorescence measurements were done in a FluoroMax-3 spectrofluorometer (Jobin Yvon-Spex).

Leaching

The nanoprobe solution was diluted in water at a concentration of 2mg/ml and stirred in an Amicon ultra filtration cell for 48 hours, at constant volume. Occasionally the filtrate was collected and the concentration of the dye was determined by comparing the absorbance of the filtrate with the absorbance of a known concentration of dye. The absorption studies were done using a Shimadzu UV-VIS spectrometer.

Calibration and limit of detection

The nanoparticles were dissolved in different pH buffer at a concentration of 25 mg/ml. The calibration was done using a widely tunable femtosecond Ti:Sapphire (Mai-Tai, Spectra-Physics) laser to excite thenanoprobes. The laser has a pulse width of less than 100 fs and operates at a frequency of 80 MHz. The central wavelength can be tuned from 690 nm to 950 nm. The light was focused onto the sample using a 10x objective. The fluorescence signal between 480 nm and 580 nm was collected through the same objective and passed through a tunable acoustic filter before being collected using a CCD. For the BCECF-NP and Lysosensor-NP the fluorescence was detected between 500nm to 600nm. The ratio of fluorescence intensity when excited with 900nm and 752nm was used for calibration. The limit of detection was determined by looking at the spectra with different concentrations of nanoprobes in different pH buffer.

Cell culture and cellular uptake procedures

A rat gliomasarcoma cell line, 9L was chosen for the pH monitoring with 2 photon NPs because of its known targetability with F3 peptide [30]. 9L cells were cultivated in Rosewell Park Memorial Institute medium (RPMI-1640), supplemented with 10 % heat inactivated fetal bovine serum (Hi-FBS). The 9L cells were plated on an 8 well chambered coverglass (Nunc. Lab-TekTM) and grown for a few days before incubation with NPs. Both the targeted and unmodified nanoprobes were incubated with the cells at 1 mg/mL final concentration for three different incubation times, 1 hour, 6 hours, and 20 hours. After each incubation, unbound NPs were removed by gentle rinsing with fresh cell media three times. Then the cells were treated with a lysosomal staining probe, lysotracker red DNB-99 for 10 minutes. The excess lysotracker probe was removed by washing with colorless RPMI media one more time.

Preparation of Spheroids

Spheroids were formed following the hanging droplet method [22]. In brief, 12 μl droplets of cell media (RPMI) containing the required density of cells (~20-50cells/12uL) were transferred onto the inner side of a Petri dish cover, filled with 10ml of PBS to prevent evaporation. The spheroid formation was monitored over 7-10 days to monitor their size and shape. When the spheroids were sufficiently large (>0.5mm), and achieved a round micro-tumor shape, the nanoprobes were added to the droplets and the spheroids incubated overnight. They were then washed thoroughly with DPBS and then used for imaging.

Fluorescence microscopy

The two photon and single photon images of the cells loaded with nanoparticles were taken using the Leica confocal microscope (SP-5X), located at the Microscopy image analysis Lab, University of Michigan. The single photon images were taken with the diode laser at 405 nm and at 450 nm, and the fluorescence emission was detected at 510nm. The single photon images were aquired in the confocal mode with a slit width of 1 Airy unit. The two photon images were taken by exciting the nanoparticles with 752 nm and 900 nm laser lines from the femtosecond Ti:Sapphire laser and the fluorescence emission was collected around 510 nm. The two photon images were aquired using either a 10X or 20X objective, whereas the single photon images were aquired using a 40X or 60X oil immersion objective. Photo multiplier tubes (PMT) were used to collect the fluorescence in both cases.

Results & Discussion

The size distribution of the nanoprobes in aqueous solution was obtained by looking at the dynamic light scattering in a particle size analyzer. The average particle size in aqueous solution was about 68 nm. The zeta potential was measured to be about +18 mV. The small size (<100nm) of the nanoprobes enables easy endocytosis of the nanoprobes into the cells. The positive charge also facilitates the uptake of the nanoprobes by the cells. From our fluorescence measurements we obtain that the concentration of dye in the nanoparticles was 0.5% by weight. The nanoprobes are highly soluble in water and PBS. However we observe some dye leaching from the nanoparticles. About 8% and 9% dye leaches out in 24 and 60 hrs, respectively. Dye leaching is an important factor because dyes outside the nanoparticle can interact with the different proteins and cell organelles that might result in a change in the optical properties of the dyes. However a 9% dye leaching over 60 hours, as observed in our case, is quite

small, especially compared to the time scale (1, 6 and 20 hours) of nanoparticle incubation with cells.

The two-photon response to pH of the HPTS-NP was characterized by looking at the fluorescence excitation spectra. The nanoprobes were excited at different wavelengths and the fluorescence emission between 480 and 580 nm was measured. The two photon excitation spectra of the nanoprobes are shown in Fig. 1(a). We look at the excitation spectra as an alternate method to the absorption spectra − which is generally the standard method to monitor the response of HPTS to variation in pH. The spectra show two distinct peaks, at 752 nm and 900 nm, as well as small local maxima at 780 nm, 810 nm and 870 nm. They correspond to the single photon absorption peaks at 376 nm, 405 nm & 450 nm. All the three single photon absorbance peaks are highly pH sensitive. The absorption at 376 nm and 405 nm increases at lower pH whereas the absorption at 450 nm decreases at lower pH. The ratio between the absorption peaks at 450 nm and 405 nm or 376 nm is generally used for calibration for pH determination [28]. We observe a drastic pH dependent change at 900 nm but, contrary to the single photon pH response, we see relatively small changes at other wavelengths, such as 752 nm or 810 nm.

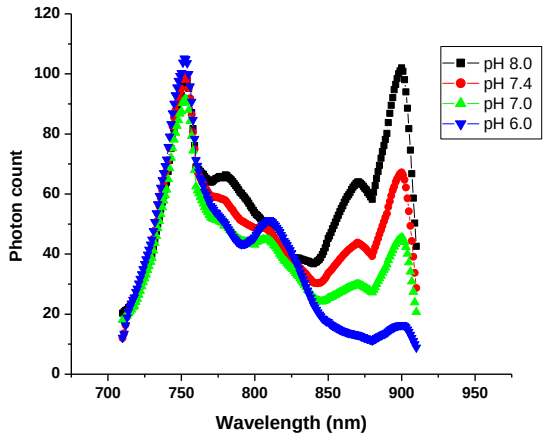

Fig 1. Two photon pH dependent fluorescence excitation spectra of (a) HPTS-NP.

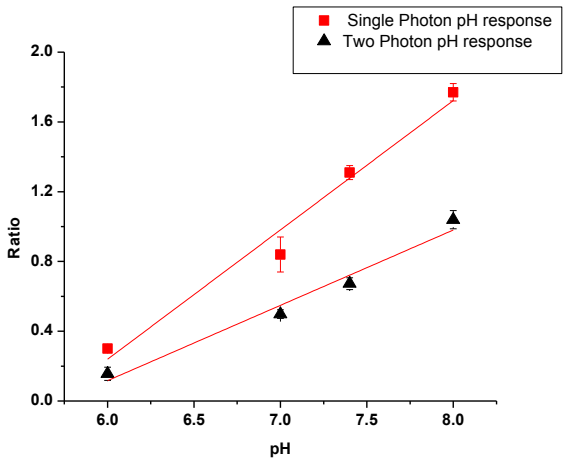

Fig 2. pH calibration curve of the HPTS-NP. The two photon calibration curve was obtained by taking the ratio of the total fluorescence intensity, measured around 510nm, when excited at 900 nm vs. 752nm wavelength. (R sq value is 0.98). The single photon calibration curve was obtained by taking the ratio of excitation at 452nm and 418nm (the isobestic point). (R sq value is 0.96)

The fluorescence intensity ratio at the two-photon excitation wavelengths of 900 nm and 752 nm increases linearly in the pH range between 6.0 and 8.0, for the HPTS-NP. The pH calibration curve, based on the ratio of fluorescence intensities, with excitation at 900 nm and 752 nm, is shown in Fig 2. It nearly follows a straight line with a slope of 0.43. The pH response of the dye is generally sigmoidal in nature. The linear region of the sigmoidal curve is determined by the pKa of the dye. So we perform the calibration in the pH region 6-8, which is close to the pKa of the dye and is also the physiologically most relevant range.

The single photon pH calibration curve is also shown in Fig 2. The single photon calibration curve follows a straight line with a slope of 0.71. With our nanoprobes it should be possible to distinguish a minimum pH change of 0.05 with the single photon and 0.08 with the two photon meaurements. The sensitivity of the single photon measurement is slightly higher (roughly 1.6 times) than the sensitivity of the two photon measurement. This is due to the higher single photon absorption cross section compared to the two photon absorption cross section and fluorescence. However the two photon technique has significantly higher signal to noise ratio.

We also compared the response of HPTS-NP with two of the most popular pH sensitive dyes, BCECF and Lysosensor based nanoparticles. The amount of dye encapsulated in these nanoprobes was similar to that of the HPTS-NP. The two-photon response based on their excitation spectra are shown in Fig. 3. Free BCECF is calibrated by taking the ratio of the excitation at 439 nm and 490 nm for fluorescence emission at 530 nm. However, strangely, the two photon excitation spectrum of the nanoparticles is not very sensitive to pH from 850 nm onwards. They are sensitive to pH from 700 nm to 850 nm but the response is not very linear in the pH range 6 to 8. The lysosensor based nanoprobes do show a linear response to change in pH, but the two-photon absorption cross section of the Lysosensor-NP is very poor. We only observe fluorescence from the Lysosensor-NP at incident powers three times higher than the normal power used for the HPTS-NP or BCECF-NP. The fluorescence output was also about ten times lower than from HPTS-NP. This is because of the low two photon cross section of Lysosensor. Thus we see that, compared to the HPTS-NP, the BCECF and Lysosensor based nanoparticles are inferior choices for two-photon pH sensing.

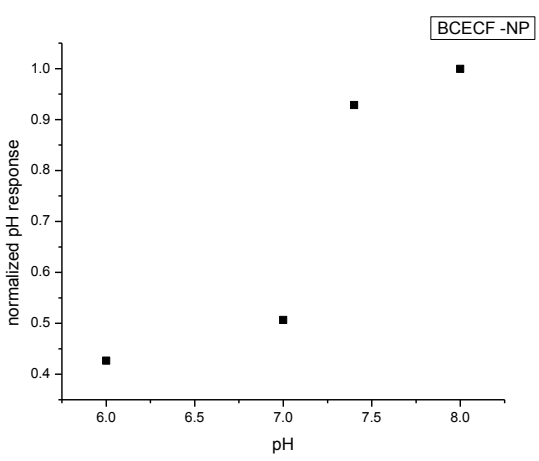

Fig 3(a)

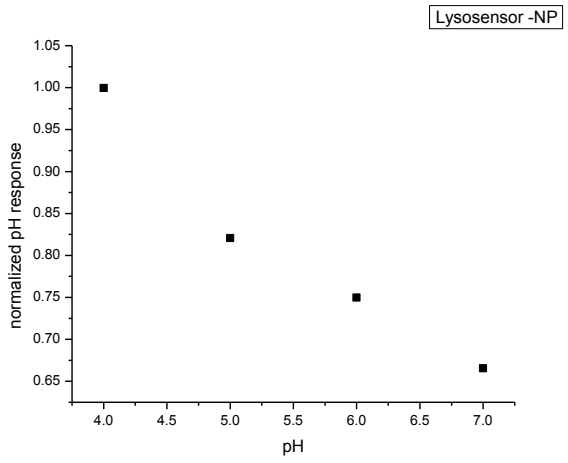

Fig 3(b)

Fig 3. Two photon pH response of the BCECF and Lysosensor based nanoprobes

Subcellular pH measurement

We used nanoprobes conjugated with the F3 peptide, and also untargeted nanoparticles, to measure the pH of the 9L rat glioma cells. The F3 peptide is a 31-amino acid fragment of HMNG-2 (human high-mobility group-2) protein and is known for its tumor homing capability towards neucleolin over-expressing tumor and tumoric endothelial cells [30-33]. Its affinity towards the 9L cell line has been previously investigated by our group [34]. In the latter case (for non-targeted nanoparticles), the 9L cells were incubated by the nanoparticles to allow the uptake via normal endocytosis. To check the effect of the surface modification and F3 peptide on the sensor, we compared the spectra of the unmodified and those of the F3 peptide attached nanoparticles in different pH buffer solutions. Attachment of the F3 peptide does not modify the spectrum of the sensor or its response to pH. During the extensive washing procedure we observed some dye leaching, which reduces the overall intensity but not the ratio. The two-photon fluorescence image of the live cells, containing nanoprobes, is shown in Fig. 4. We take the ratio of the fluorescence intensity when excited at 900 nm and 752 nm, and obtain an average intracellular pH value of 7.1 ± 0.2, with the F3 peptide targeted nanoprobes, which is similar to the values reported previously for the 9L cells using NMR spectroscopy [35].

For the unmodified (non-targeted) nanoprobes we obtain an average intracellular pH value of 6.3±0.2. This is probably because these nanoprobes are trapped in endosomes, which are acidic in nature. The difference between the cellular uptake mechanism for the unmodified nanoprobes and for the nanoprobes attached to targeting or cell internalizing peptide are currently being studied.. In both cases we look at changes in the intracellular pH values due to varying the incubation time of the nanoprobes. The nanoprobes were incubated for 1 hr, 6 hrs and overnight. The intracellular pH values did not change appreciably in either case and were identical, within the error range.

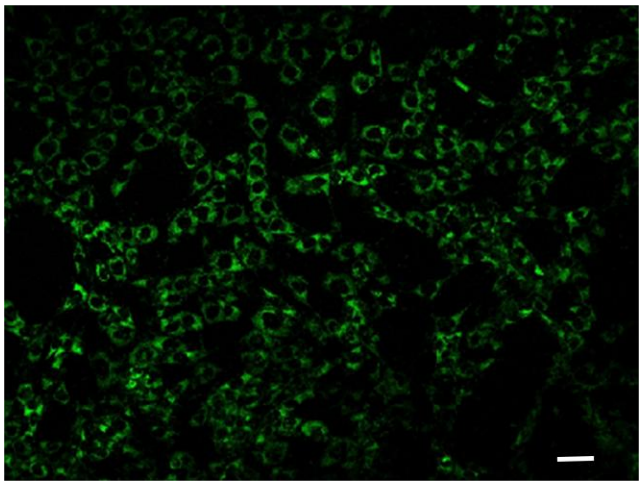

Fig. 4. Two Photon image of the 9L rat glioma cells (Scale 50μm). This image was obtained by exciting the live cells at 900nm. A 10X magnification was used for this image. The fluorescence signal was recorded using a PMT.

To explain the discrepancy between the targeted and nontargeted nanoprobes we perform co-localization studies of the targeted nanoprobes with early endosomes and lysozome. We incubated the cells with nanoprobes and lysotracker. The lysotraker probes can specifically stain the acidic compartments of the cells and have been widely used to visualize lysosomes, which has strong relative acidity. The fluorescence images were obtained by exciting the nanoprobes with 450 nm & 405nm and the lysotracker with 568 nm, while collecting the fluorescence emission at 510 nm and 600 nm, respectively. The overlaid image is shown in Fig 5. We observe, by comparing the yellow and green coloured pixels, that only a small fraction (~5%-) of the nanoparticles is in the lysosomes. We estimate that the rest 95% remains elsewhere in the cytoplasm, even after overnight incubation.

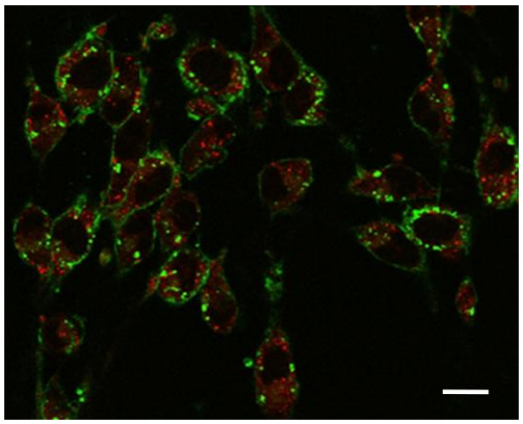

Fig. 5 Overlay of the fluorescence from nanoprobes (green) and the lysotracker (red). Orange/Yellow shows the position of nanoprobes overlapping with lysosomes. We see that only a small fraction of nanoparticles are inside the lysosomes. The nanoparticles were excited by both 405nm and 450nm, while the lysotracker was excited by 568nm wavelength. This image was taken in the confocal mode. (Scale 20μm).

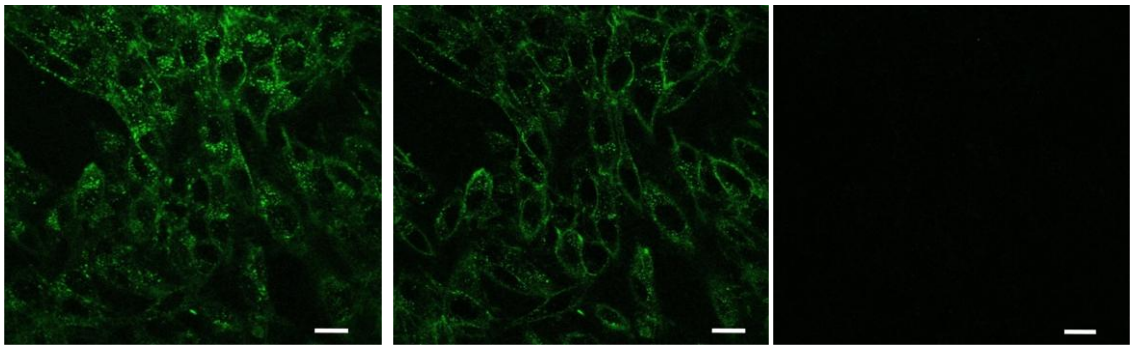

Fig 6(a) Fig 6(b) Fig 6(c)

Fig 6. Autofluorescence from the 9L control cells when excited with (a) 405 nm, (b) 450 nm and (c) 752 nm (Scale 20 μm). The single photon autofluorescence images (a&b) were performed in the confocal mode.

One of the major advantages of using two-photon fluorescence is the reduction in cell autofluorescence. We used control cells, which were not incubated with nanoprobes, to check the two-photon autofluorescence. Fig 6 shows the autofluorescence of these cells when excited with 405 nm, 450 nm and 750 nm respectively. The autofluorescence measurements were taken under the same imaging conditions as the other pH measurements. The single photon autofluorescence is 20-25% of the total single photon fluorescence from the nanoparticles. This might lead to considerable errors when taking measurements. On the other hand, extremely low autofluorescence is observed from the cells when excited with 750 nm or 900 nm wavelengths. The two photon autofluorescence was less than 5% of the total two photon fluorescence signal from the nanoparticles inside cells.

pH mapping in tumor spheroids

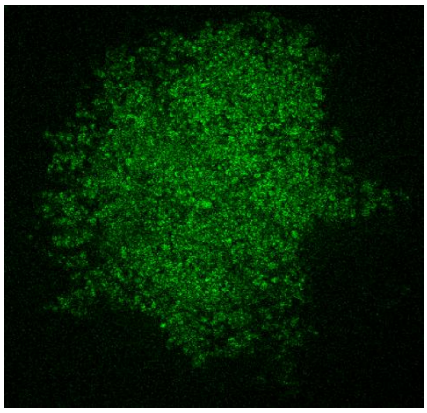

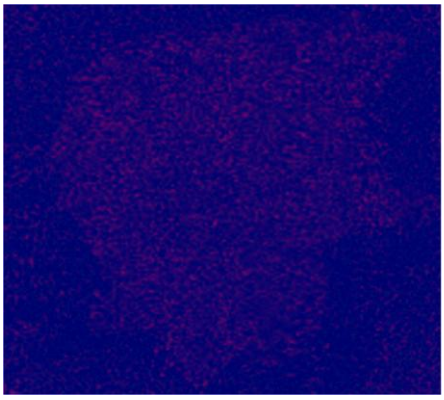

Fig 7 (a) Fig 7(b)

Fig 7. (a) A two-photon fluorescence image of the Hela cell spheroid with pH sensing nanoparticles, excited at 900nm (Spheroid size ~0.8 mm), (b) pH distribution inside the HeLa Cell spheroid. The blue pixels have a pH value of 7.4 whereas the red pixels have an average value of 6.5, The overlay (pink pixels) have a pH value inbetween 6.5 and 7.4.

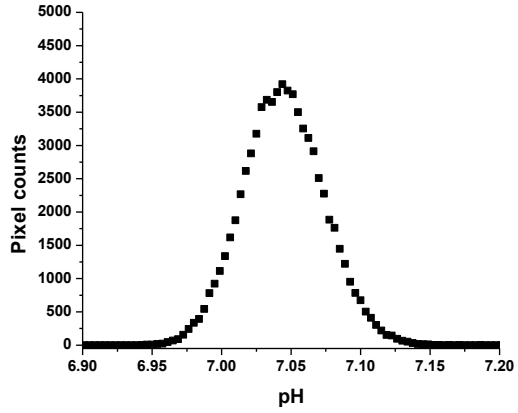

Fig. 8. The pH distribution inside the spheroid as obtained from Fig7. We observe the average pH value is around 7.05.

Another important aspect of using two photon fluorescence is the high penetration depth. To exploit the high penetration depth we map the pH distribution inside human cervix cancer cell (HeLa cell) spheroids. We use the HeLa cell spheroids because of their stability as compared to the 9L or MDA cell spheroid. Spheroids are micro-tumors that are widely used as *in-vitro* three-dimensional tumor models to study the different properties of the tumor for the purpose of drug delivery, therapy, etc. [36].

We use nanoparticles conjugated with the F3 peptide to measure the pH of the human cervix cancer (HeLa) cell spheroid. Spheroids as big as 500-800 microns were used for this purpose. The two photon fluorescence image of the spheroid cross section, at the core, is shown in figure 7a. We observe a slightly higher concentration of nanoparticles at the spheroid core rather than the periphery. Fig 7b shows the 2-dimentional pH map at the center cross-section of the spheroid. The pH distribution was determined by dividing the fluorescence intensity at 900nm to that of 752nm and comparing the ratio with the calibration curve. The higher pH regions (pH 7.4) were assigned blue color whereas the low pH regions (pH 6.5) were assigned red color. The overlay of the blue and red pixels (pink pixels) gives us

the exact pH value at the particular point. From the pH distribution curve (Fig.8), we observe that the average pH of the spheroid is around 7.05, however there are certain regions within the tumor that have a relatively lower pH, probably due to the presence of necrotic cell clusters or anomalous metabolic rates. Otherwise the overall pH follows a Gaussian distribution. Further studies are ongoing to determine the exact reasons for this variation in pH and the effect of changes in the local environment on the spheroid pH.

Conclusions

We demonstrated two-photon intracellular pH sensing in 9L glioma cells, using both targeted and nontargeted ratiometric nanoprobes. The nanoprobes are made of HPTS dye encapsulated inside a PAA hydrogel matrix. The nanoproes have an average size of 68 nm and contain about 0.5% dye by weight. They have two-photon absorption peaks at 752 nm, 810 nm and 900 nm. The ratio between the excitation at 900 nm and 752 nm is used to measure the pH. The sensor has a linear response in the biological range of pH 6 to 8. These nanoprobes are expected to be suitable for both in-vitro and in-vivo measurements, using NIR light at 900 nm, which minimizes scattering and cell autofluorescence and thus significantly increases the signal-to-noise ratio. We note that the use of these nanoprobes allows HPTS, which is membrane impermeant, to enter intra-cellular environments, as well as subcellular targeting. These nanoprobes were used successfully for reliable real-time pH measurements, inside live tumor cells. We obtained an intracellular pH value of 7.1 throughout most of the 9L cells.

Acknowledgement's

This work was supported by NIH/NCI Grant R33CA125297 (RK). We thank Dr. Steve Katnik and Mr. Ron Smith for their help to troubleshoot the femtosecond laser. We thank Dr. Hoe Jin Hah for his help during F3 peptide conjugation. We also thank Mr. Chris Edwards and Mr. Sasha Meshinchi at the Microscopy and Image-analysis Laboratory for their technical support in confocal imaging.

References

1. S. Humez, M. Monet, F. van Coppenolle, P. Delcourt and N**.** Prevarskaya, *Am. J. Physiol. Cell Physiol*., 2004, 287, 1733-1746.

2. I. H. Madshus, *Biochem J.,* 1988, **250**, 1–8.

3. A. Kurkdjian and J. Guern, *Annu. Rev. Plant Physiol. Plant Mol. Bio*., 1989, **40**, 271-303.

4. X. Zhang, Y. Lin and R. J. Gillies, *J. Nucl. Med.,* 2010, **51**,1167–1170.

5. A. Salvi, J. M. Quillan and W. Sadé, A.A.P.S. Pharm. Sci., 2002, **4**, article 21.

6. J. Han and K. Burgess, *Chem. Rev.,* 2010, **110**, 2709–2728.

7. R. M. Andersson, K. Carlsson, A. Liljeborg and H. Brismar, *Anal. Biochem.,* 2000, **283**, 104–110.

8. C. Hille, M. Berg, L. Bressel, D. Munzke, P. Primus, H. G. Löhmannsröben and C. Dosche, *Anal. Bioanal. Chem.,* 2008, **391**, 1871–1879.

9. R. Pal and D. Parke, Org. Biomol. Chem., 2008, **6**, 1020 – 1033.

10. J. Han, A. Loudet, R. Barhoumi, R. C. Burghardt and K. Burgess, *J. Am. Chem. Soc.,* 2009, **131**, 1642–1643.

11. S. Egginton, E. W. Taylor and J. A. Raven, Cambridge University Press, 521623170, 1999.

12. C. Gatto and M. A. Milanick, Am. J. Physiol. Cell. Physiol., 1993, **264**, C1577-C1586.

13. H. A. Clark, M. Hoyer, M. A. Philbert and R. Kopelman, *Anal. Chem.,* 1999, **71**, 4831-4836.

14. H. A. Clark, R. Kopelman, R. Tjalkens and M.A. Philbert, *Anal. Chem.,* 1999, **71**, 4837-4843.

15. J. P. Sumner, N. M. Westerberg, A. K. Stoddard, C. A. Fierke and R. Kopelman, *Sensors and Actuators B,* 2006, **113**, 760–767.

16. E. Moding, J. Hellyer, K. Rank, P. Lostroh and M. Brasuel, *Journal of Sensors,* 2009, **2009**, Article ID 235158. Page 1-4.

17. Y. E. Koo Lee, R. Smith and R. Kopelman, *Annu. Rev. Anal. Chem.,* 2009, **2**, 57-76.

18. Y. E. Koo Lee and R. Kopelman, *WIREs Nanomed. Nanobiotechnol.,* 2009, **1**, 98-110.

19. S. M. Bucka, H. Xua, M. Brasuel, M. A. Philbert and R. Kopelman, *Talanta,* 2004, **63**, 41–59.

20. Y. E. Koo Lee, E. E. Ulbrich, G. Kim, H. Hah, C. Strollo, W. Fan, R. Gurjar, S. M. Koo and R. Kopelman, *Anal. Chem.,* 2010, **82**, 8446-8455.

21. F. Bestvater, E. Spiess, G. Stobrawa, M. Hacker, T. Feurer, T. Porwol, U. Berchner-Pfannschmidt,C. Wotzlaw and H. Acker, *J. of Microscopy,* 2002, **208**, 108–115.

22. J. N. Anker and R. Kopelman, *Applied Physics Letters*, 2003, **82**, 1102-1104.

23. J. N. Anker, C. J. Behrend, H. Huang, R. Kopelman, *Journal of Magnetism and Magnetic Materials*, 2005, **293**, 655–662.

24. M. Oheim, D. J. Michael, M. Geisbauer, D. Madsen and R.H. Chow, *Adv. Drug Deliv. Rev.*, 2006, **58**, 788-808.

25. P. D. Jobsis, C. A. Combs and R. S. Balaban, *Journal of Microscopy*, 2005, **217**, 260–264.

26. Z. Zhang and S. Achilefu, *Chem. Commun.*, 2005, **47**, 5887–5889

27. H. Lee, M. Y. Berezin, K. Guo, J. Kao and S. Achilefu, *Org. Lett.*, 2009, **11**, 29–32.

28. C. C. Overly, K. D. Lee, E. Berthiaume and P. J. Hollenbeck, *Proc Natl. Acad. Sci. U.S.A.*, 1995, **92**, 3156.

29. A. Pena, J. Ramirez, G. Rosas and M. Calahorra, *J. Bacteriol.*, 1995, **177**, 1017.

30. D. A. Orringer, Y. E. Koo, T. Chen, G. Kim, H. J. Hah, H. Xu, S. Wang, R. Keep, M. Philbert, R. Kopelman and O. Sagher, *Neurosurgery*., 2009, **64,** 965–972.

31. K. Porkka, P. Laakkonen, J. A. Hoffman, M. Bernasconi and E. Ruoslahti, *Proc. Natl. Acad. Sci. U.S.A.*, 2002, **99**, 7444–7449.

32. E. Akerman, W. C. Chan, P. Laakkonen, S. N. Bhatia and E. Ruoslahti, *Proc. Natl. Acad. Sci.U.S.A.*, 2002, **99**, 12617–12621.

33. E. Ruoslahti, T. Duza and L. Zhang, *Curr. Pharm. Des.*, 2005, **11**, 3655–3660.

34. Y. E. Lee Koo, G. R. Reddy, M. Bhojani, R. Schneider, M. A. Philbert, A. Rehemtulla, B. D. Ross and R. Kopelman, *Adv. Drug Deliv. Rev.*, 2006, **58**, 1556–1577.

35. N. Suzuki, I. L. Kwee, L. B. Tamas and T. Nakada, *Magnetic Resonance in Medicine*, 1991, **19**, 422-428

36. Santini, M. T. and Rainaldi, G., "Three-dimensional spheroid model in tumor biology," *Pathobiology* 67(3), 148-57 (1999).

Chapter 3

Core-Shell nanoprobes for enhanced two photon fluorescence imaging: application to subcellular pH

This chapter has been adapted with minor modifications from the following published article:

A. Ray, Y. E. Koo Lee, G. Kim and R. Kopelman, "Two-photon fluorescence imaging super-enhanced by multi-shell nano-photonic particles : Application to subcellular pH", *Small* 8(14):2213-21 (2012)

Introduction

Multi-photon fluorescence is a very powerful technique for spectroscopic measurements and for biomedical imaging in cells or tissues. Multi-photon excited fluorescence is a nonlinear optical process in which two, or more, photons, typically in the near infrared (NIR) region, are absorbed simultaneously and the fluorescence occurs at a shorter wavelength (higher frequency), typically in the visible region. Two-photon fluorescence is the most commonly used option, due to its relatively higher absorption cross-section, compared to other multi-photon fluorescence modes. Multi-photon fluorescence has higher spatial resolution than one-photon fluorescence, because the fluorescence's quadratic (two-photon) [or cubic (three-photon)] dependence on the excitation intensity turns it into a highly localized and spatially confined excitation. It also allows the use of NIR radiation for exciting fluorescent dyes in the visible range, enabling a much enhanced penetration depth, on the order of several mm, in tissues. Furthermore, it also significantly

reduces both autofluorescence from, and photo-damage to, the cells/tissues, and thus increases further the signal-to-noise ratio.[1-3] However, one of the biggest disadvantages of using nonlinear excitation is its extremely low absorption/fluorescence cross-section. The probability of simultaneously absorbing two low-energy photons is quite low. Thus, for most dyes, the two-photon fluorescence signal is much weaker, by many orders of magnitude, than the one-photon fluorescence signal. The weak nature of this two-photon fluorescence emanating from the dye molecules has severely limited in-vivo applications, penetration depth and choice of dye, thus preventing it from achieving its full potential.

Several methods have been utilized to enhance the two-photon fluorescence signal,[4-13] some of which have indeed shown orders of magnitude enhancements in the two-photon fluorescence signal, and also enabled optical microscopy beyond the diffraction limit. Most of these near-field optics or nanophotonic techniques have used metallic films, or nanoparticles, or fractal nano-islands, or tips, which, however, would all be limited to the cellular membrane or tissue surface, and thus would not be suitable for intracellular or deep *in-vivo* imaging. Also, some of the above techniques use total internal reflection fluorescence (TIRF) microscopy to couple the light into the surface plasmon resonance (SPR) modes. TIRF microscopy is a very sensitive technique and has a very high signal-to-noise ratio but, unfortunately, it is unable to exploit one of the main advantages of using NIR light - its large penetration depth. In TIRF microscopes the penetration depth is determined by the decay of the evanescent waves, which is typically only several hundred nm. One possible way to enhance the two-photon fluorescence, which would overcome the above limitations, was introduced using the technique of resonance energy transfer between semiconductor nanocystals and probes,[14] however this technique has not been demonstrated in

cells or tissues. So far, no technology has been established that can enhance two-photon fluorescence signals inside cells, or deep inside tissues.

The two-photon fluorescence enhancement in the previous studies is mostly based on surface plasmon resonance (SPR), also known as the MEF effect. The presence of metallic nanoparticles can either enhance or quench the fluorescence of a fluorophore adsorbed on its surface, with a delicate dependence on the distance from the metal surface,[15-17] and, presumably, the molecular orientation. The enhancement in fluorescence generally occurs when fluorophores are present close enough to the metal surface, due to the presence of the metal's surface plasmons (SP), which lead to an enhanced local electric field near the metal surface. Surface plasmons are oscillating free electrons on the surface of the metal. If the dye molecules are too close to the metal surface (0-5 nm), their fluorescence is quenched, because the excitation fluorescence energy is transferred to the metal surface and is dissipated as heat.[15] For larger separations there is an increase in fluorescence, either due to an enhancement of the incident light field, especially around the edges of the nanoparticles, or due to an increase in the radiative decay rate.[16-17] Apart from SPR, Förster resonance energy transfer (FRET) has also been utilized to enhance the two-photon fluorescence from fluorophores.[14] The fluorescence is enhanced due to a direct resonance energy transfer from the oscillating electrons of the donor to the fluorophore, due to a transition-dipole—transition-dipole coupling.

Presented in this chapter is a new strategy to enhance two-photon fluorescence *in vivo* , using the MEF effects due to resonance energy transfer, surface plasmon resonance and second harmonic generation known as hyper Rayleigh scattering (HRS), as shown in Fig 1. This is the first demonstration of such fluorescence enhancement inside living cells. HRS is a second-order

nonlinear process that leads to *incoherent* second harmonic generation (SHG), i.e., production of light at half the wavelength of the excitation laser. The phenomenon of HRS arises from the induced-dipole polarization and the quadrupole polarization, due to the surface-induced nonlinear susceptibility. The quadrupole contribution is more significant for nanoparticles greater than 30 nm.[18] Metal nanoparticles such as gold or silver have been used for HRS due to their large hyperpolarizability (β), which gives rise to very large second harmonic signals.[19-23] HRS has been used for certain biological applications, such as the detection of the Tau protein, identification of E Coli bacteria, sequence specific HCV RNA quantification, etc., by looking at the change in the scattering intensity of the second harmonic signal.[24-26]

This nano-photonic technique exploits all the advantages of NIR excited multi-photon fluorescence, such as reduced scattering, larger penetration depth, highly localized excitation, low autofluorescence and high signal-to-noise ratio. The technique can be applied using any type of metal nanoparticles that has a large hyperpolarizability value, such as gold or silver. We note that metal core-polymer shell type nanoparticles [27-29] or gold nanoparticles[30] have already been used to enhance the one-photon fluorescence signal [27-28] and second harmonic signal [29-30] but not yet for two-photon fluorescence.

To demonstrate the *in-vivo* applicability of this technique, we prepared a core-shell nanoparticle pH sensor by encapsulating into an inert polyacrylamide matrix a pH sensitive dye, 8-Hydroxypyrene-1,3,6-trisulfonic acid (HPTS), adsorbed onto citrate-coated silver nanospheres. The citrate coating helps maintain some distance between the dye molecules and the metal surface. The polyacrylamide matrix shell of our nanoparticles has several chemical and biological advantages, as reported previously,[31- 34] in addition to obviating metal nanoparticle

clusterization. We observed a maximum enhancement of 20 times for the fluorescence intensity of HPTS, when irradiated with focused femtosecond pulses at a selected NIR wavelength, compared to free dye or nanoparticles containing dye only. We applied this nanoparticle sensor for intracellular pH sensing, which demonstrates the feasibility of these nanosensors for imaging applications in cells and tissues, and for future *in-vivo* sensing. We note that nanoparticle-based fluorescent sensors have numerous advantages over fluorescent molecular probes, such as better sensitivity, selectivity and targetability,[31- 34] can be seamlessly combined with this new multishell approach for enhancing two-photon biochemical imaging.

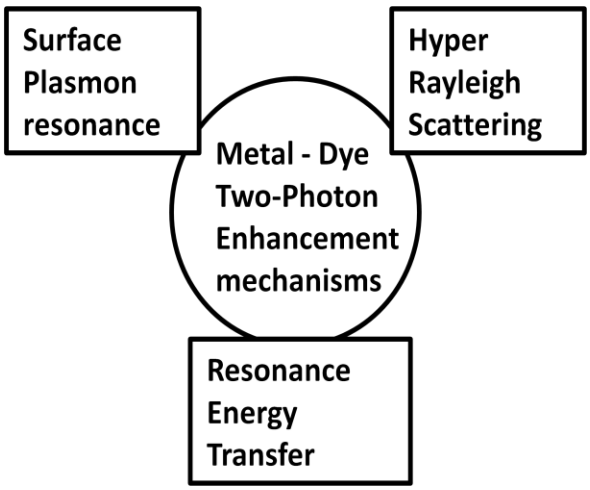

Figure 1. (a) Potential two photon fluorescence enhancement mechanisms

Experimental

Materials.

Acrylamide, methylene-bis-acrylamide (MBA), dioctylsulfouccinate (AOT), Brij 30, hexane, ammonium persulfate (APS), N,N,N',N'-tetramethylethylenediamine(TEMED), and L-cysteine were all acquired from Sigma-Aldrich (St. Louis, MO). 3-(aminopropyl)methacrylamide hydrochloride salt (APMA) was obtained from Polysciences Inc. (Warrington, PA). Ethanol (95%) was acquired from Decon labs, Inc (King of Prussia, PA). HPTS was obtained from Invitrogen (Carlsbad, CA). The silver nanoparticles (Biopure) were obtained from NanocomposixInc. (San Diego, CA). All solutions were prepared in 18-MΩ water purified in a Barnstead 1 Thermolyne Nanopure II system. All chemicals and materials were used as received.

Preparation of the nanoparticles

The nanoparticles were prepared using a micro-emulsion and radical polymerization technique. The core was prepared by first adding 19 mmol HPTS to 1.6ml solution of silver nanospheres(10 nm or 60 nm) in citrate buffer (1mg/ml).The silver nanospheres have a citrate capping. Citrate is a small molecule and a relatively weak capping agent, so it may not prevent, but possibly limit, dye molecule adsorption. After the dye got adsorbed into the silver, the monomers—acrylamide(8.6 mmol), APMA (0.25mmol), MBA(1.2 mmol)—was added to it. This solution was then added to a 36 ml hexane solution containing 6.85 mmol Brij-30 and 2.88 mmoldioctyl-sulfosuccinate. The two solutions were emulsified by stirring them for 20 mins under an inert atmosphere. The reaction was initiated by using 0.54 mmol TEMED and 28 μmol APS, freshly prepared 10% (Weight/Volume) in water. The solution was further stirred for two

hours under an inert atmosphere so as to complete the polymerization. Hexane was removed by rotary evaporation, using Rotavapor-R (Brinkmann Instruments), and then suspended in ethanol. The surfactants and excess dye were removed by washing the particles five times with ethanol and five times with water for over two days, in an Amicon ultra-filtration cell (Millipore Corp., Bedford, MA), using a 300 kDa filter, and then freeze-dried with a 5L ModulyoD freeze dryer. The rhodamine containing nanoparticles were prepared by post loading the Rhodamine dye into blank polyacrylamide nanoparticles containing a silver core. Rhodamine is extremely soluble in ethanol and leaches out of the nanoparticles while washing in ethanol. Therefore we post load the dye into the nanoparticle by stirring it in an aqueous solution containing blank nanoparticles overnight. The nanoparticles are then washed thoroughly in water a few times to get rid of any extra dye and then freeze dried.

Particle size and Zeta Potential.

The particles were diluted in water at a concentration of 1mg/ml and the particle size distribution in aqueous solution and the Zeta potential were measured by dynamic light scattering (DLS), using a Beckman-Coulter Delsa Nano C Zeta potential/submicron size analyzer.

Silver encapsulation

ICP spectroscopy: The amount of silver encapsulated is determined by Inductively Coupled Plasma (ICP)-Optical Emission Spectroscopy, using a Perkin-Elmer Optima 2000 DV machine. The nanoparticle sample concentration was 2mg/ml in water.

X-Ray Diffraction : Powder XRD experiments were performed by using a Bruker D8 Advance Powder X-ray Diffractometer.

Dye concentration

The amount of dye encapsulated in the nanoparticles was determined by comparing the fluorescence and absorbance from a known concentration of the nanoparticles in water to the fluorescence signals obtained from a set of known concentration of dye and silver nanoparticles in water. We first determined the amount of silver nanospheres present in the nanoparticle solution by performing ICP. We then prepared calibration samples containing the same amount of free silver nanospheres while varying the concentration of the dye. We constructed the calibration curve by looking at the fluorescence (and absorbance), using the (free silver + dye) calibration solution and then comparing it with the absorbance/ fluorescence of the nanoparticle solution. This is a bulk measurement and is quite accurate. The fluorescence measurements were done in a FluoroMax-3 spectrofluorometer (JobinYvon-Spex).

Leaching.

The nanoparticle solution was diluted in water at a concentration of 5mg/ml and kept for 48 hours under constant stirring. They were then centrifuged at 4000 RPM. The filtrate was collected and the concentration of the dye was determined by comparing the absorbance of the filtrate with the absorbance of a known concentration of dye. The absorption studies were done using a Shimadzu UV-VIS spectrometer.

Calibration and optical characterization.

The nanoparticles were dissolved in different pH buffer at a concentration of 6.5 mg/ml. The calibration was done using a widely tunable femtosecond Ti:Sapphire (Mai-Tai, Spectra-Physics) laser. The laser has a pulse width of less than 100 fs and operates at a frequency of 80 MHz. The

central wavelength can be tuned from 690 nm to 950 nm. The light was focused onto the sample using a 10x objective. Two excitation wavelengths, 900 nm and 740 nm were used and the fluorescence signal between 480 nm and 580 nm at each excitation wavelength was collected through the same objective and passed through a tunable acoustic filter before being collected using a photo-multiplier tube (PMT). The ratio of the two fluorescence intensities was used for calibration. The enhancement was measured by taking the ratio of the fluorescent signal from the silver and dye encapsulated nanoparticle and the equal concentration of free dye by exciting them between 740 nm and 920 nm.Transmission Electron Microscopy (TEM) was performed by using 0.01mg/ml nanoparticle solutions and the negative staining of the polyacrylamide was done with Uranyl Acetate. The TEM was performed using a Philips CM-100 TEM microscope.

Cell culture procedures.

MDA-MB-435 was chosen for intracellular sensing. MDA cells were cultivated in a Roswell Park Memorial Institute medium (RPMI-1640), supplemented with 10 % heat inactivated fetal bovine serum (Hi-FBS). The cells were plated on an 8 well chambered coverglass (Nunc. Lab-Tek^{TM}) and grown for a few days before incubation with NPs.

Cellular uptake procedures

The cells were incubated with the nanoparticles of 1 mg/mL final concentration for three hours. After incubation, unbound NPs were removed by gentle rinsing with fresh cell media three times. Then the cells were treated with a lysosomal staining probe, lysotracker red DNB-99 for 10 minutes. The excess lysotrakcer probe was removed by washing with colorless DMEM media one more time.

Fluorescence microscopy

The two photon and single photon images of the cells loaded with nanoparticles were taken using the Leica confocal microscope (SP-5X), located at the Microscopy image analysis Lab, University of Michigan. The single photon images were taken with the diode laser at 405 nm and at 450 nm, and the fluorescence emission was detected at 510 nm. The single photon images were acquired in the confocal mode with a slit width of 1 Airy unit. The two photon images were taken by exciting the nanoparticles with 752 nm and 900 nm laser lines from the femtosecond Ti:Sapphire laser and the fluorescence emission was collected around 510 nm. The two photon images were acquired using either a 10X or 20X objective, whereas the single photon images were acquired using a 40X or 60X oil immersion objective. Photo multiplier tubes (PMT) were used to collect the fluorescence in both cases.

MTT Assay for toxicity test

Cells were cultivated on 96-well plates. For each treatment with nanoparticles and for a control (cells without any treatment), a total of 12 wells were used for reliable measurements. The nanoparticles containing silver and dye were added to a cell medium, so as to make the nanoparticle concentration to be 1 mg/mL. For comparison, blank PAA nanoparticles were also added to a cell medium at a similar concentration of 1 mg/mL. After a 4 hour incubation, the treated cells were washed three times with fresh cell medium, so as to remove any unbound nanoparticles. A 100 µl of an MTT solution (2.5 mg/ml in PBS) was added to each treated well and control. The cells were incubated for 4 h at 37°C, and then the cell medium was removed and 100 µl of DMSO was added, in order to solubilize water-insoluble formazan that was formed

by reduction of the MTT agent by live cell enzymes. The cell viability was determined by measuring the light absorbance of each well at a wavelength of 550 nm and comparing the results with those from the controls.

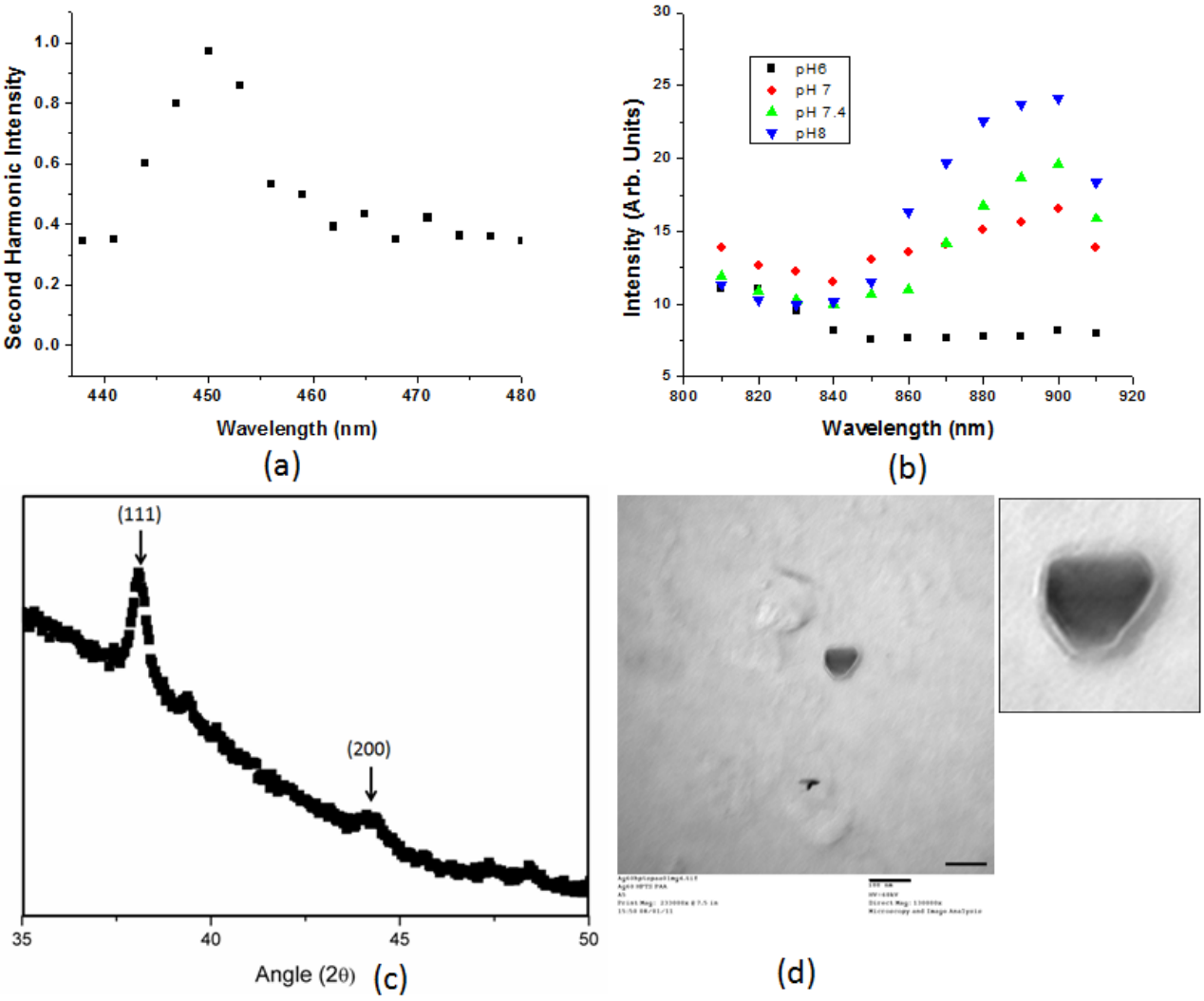

Figure. 2 Characterization of the nanoparticle. (a) Second Harmonic generated by the 60 nm silver nanospheres, irradiated at 900 nm. (b) pH dependent two photon excitation spectra from the nanoparticles, (c) XRD pattern recorded from the nanoparticles with silver core. The peaks

corresponds to the (111) and (200) reflection of the fcc silver, respectively (d) TEM image of the nanoparticles containing silver (Scale: 100 nm). Inset: magnified image of the nanoparticle (3X).

Results and discussion

Characterization of nanophotonic particles

We confirmed the presence of HRS by irradiating the silver nanoparticles, without the dye and polymer coating, with a high intensity femtosecond laser and collecting the second harmonic generated signal using a Photo-Multiplier Tube. Fig. 2a shows the second harmonic spectrum generated by the 60 nm silver nanoparticles, when irradiated by the 900 nm laser line. Under biologically relevant laser intensity conditions we see a weak second harmonic signal generated by the 60 nm silver nanospheres, which is quite easily distinguishable from the background. However, we did not see second harmonic signals generated from 10 nm silver nanospheres. This is due to the much lower SH generation, possibly due to the low β (hyperpolarizability) value of the 10 nm spheres, compared to the 60 nm ones.

We prepare nanoprobes by encapsulating dye adsorbed silver nanoparticles (10 nm or 60 nm) into a polyacrylamide matrix. Encapsulating the silver in the polyacrylamide matrix prevents them from aggregating, which is one of the main challenges with metallic nanoparticles. The small pore size of the matrix prevents not only the silver but also the dye molecules from interacting with the proteins or other macromolecular components present inside the cell compartments. However, the hydrogel pores allow free flow of small ions and molecules, such as H^+, Ca^{2+}, K^+ or O_2, thus enabling the nanoparticle core to act as chemical sensor.[31-34] The

prepared nanoparticle sensors show pH dependent two-photon fluorescent excitation spectra, as presented in Fig 2b. The ICP measurements show a high amount of silver encapsulation inside the nanoparticles. This is also confirmed by looking at the powder X-Ray diffraction, as shown in Fig 2c. The size of the nanoparticles containing a silver core varies from 90-130 nm, according to the TEM images. A typical TEM image of a nanoparticle containing silver is shown in Fig 2d. The surface charge of the nanoparticles was measured to be about +18 mV. We confirmed the absence of silver nanosphere clusters in our nanoparticles by looking at the bulk absorption spectra of these nanoparticles. Free silver nanospheres, when clustered, have a second absorption peak in the range 600-700 nm. But for our nanoparticles we do not observe any absorption band at 600-700 nm. This bulk absorption study further confirms that most, if not all, of the embedding polyacrylamide nanoparticles contain a single silver nanosphere and not a cluster of nanospheres. From our fluorescence and absorbance measurements we obtain that the concentration of dye in the nanoparticles with 60nm core was about 1.1% by weight, while the 10 nm core nanoparticles had only 0.57% dye (by weight) encapsulated in them. The nanosensors are highly soluble in water and PBS. The dye leaching from the nanoparticles was extremely low. Generally, dye leaching is very significant when the dye is just encapsulated and not covalently linked to the matrix. With the silver core the dye leaching from the nanoparticles was about 0.2%, under constant stirring in water for 24 hours, which is 50 times less compared to the nanoparticles without a silver core.[34] This reduction in the dye leaching is because the dye gets adsorbed onto the surface of the silver cores. This low degree of leaching out is quite remarkable, and comparable to the low leaching of dyes that are covalently linked to the matrix. We tested the toxicity of the nanoparticles by performing MTT assays. These toxicity assays

show that the nanoparticles are practically non-toxic to cells, after 4 hour incubation at a 1mg/mL concentration, exhibiting a higher than 98% cell viability.

(3a)

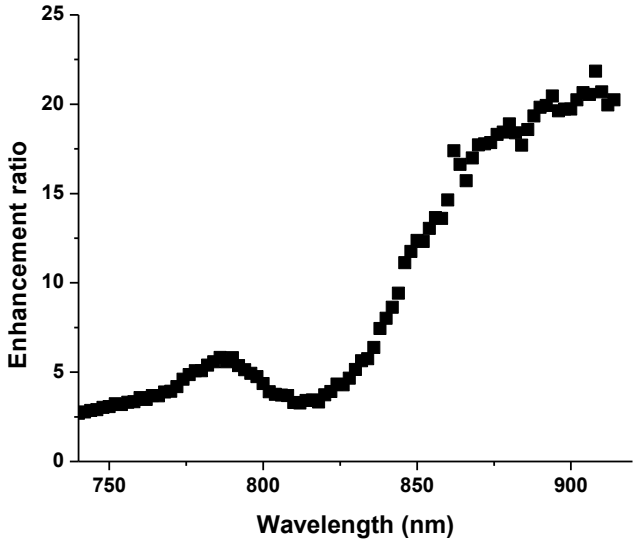

(3b)

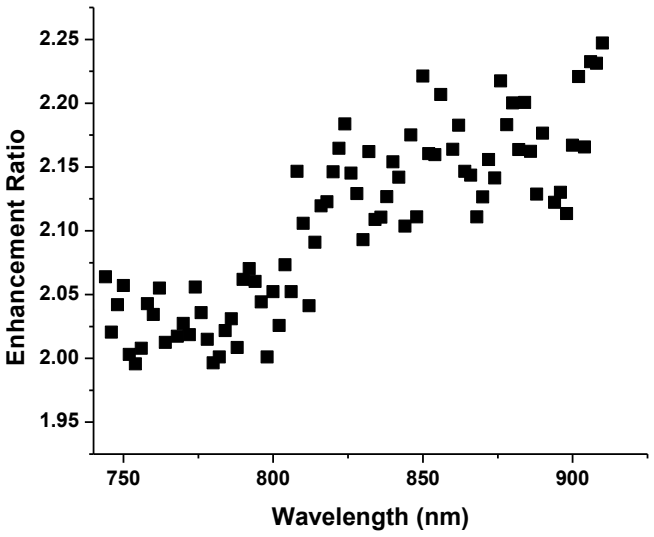

Figure.3 Two-photon fluorescence enhancement of the HPTS-nanoparticles with 60 nm silver core (Fig. 3a) and 10 nm silver core (Fig. 3b). For the 60 nm silver we see a maximum enhancement of 20 times whereas for the 10 nm silver we see a maximum enhancement of only 2.2 times.

Two Photon fluorescence enhancement

The enhancement of the two-photon signal was observed by comparing the fluorescence signal from the nanoparticles with silver core to that from equivalent amounts of free dye as well as nanoparticles containing dye but no nanoparticle. HPTS has multiply-peaked, broad absorption bands, around 370 nm, 405 nm and 450 nm, and an emission maximum at 510 nm. The nanoparticles were excited at different wavelengths, between 740 to 920nm, and the fluorescence emission between 480 and 580 nm was measured. The wavelength dependent enhancement for the fluorescent signal is shown in Fig 3. For the 60nm silver core we see a maximum *enhancement of about 20 times* (Fig 3a.) and for the 10 nm silver core we see an enhancement of only 2.2 times (Fig 3b.). We also found a similar enhancement trend for the nanoparticles with a 60 nm or 10 nm silver core, by measuring the fluorescence intensity between 560 nm and 600 nm, which was done to avoid any error due to possible interference at shorter wavelength, despite the much weaker fluorescence signal intensity.

We hypothesize that the major reason for the higher enhancement (~ 10 times) in the fluorescent signal of the nanoparticles with the 60 nm silver cores — compared to the nanoparticles with 10 nm silver cores — may be due to resonance energy transfer or due to generation of second harmonic photons, by the silver core, which in turn excites the fluorescent dye in the core's vicinity. This latter process is a one-photon fluorescence process and thus is much more efficient than the two-photon fluorescence, thus having the potential to lead to a many-fold increase in the fluorescence signal. This hypothesis is mainly based on the wavelength dependent enhancement trend, as well as on a comparison with a dye (Rhodamine 6G) that does not have an overlapping absorption spectrum with the second harmonic of the exciting light. It has been shown previously

that the hyperpolarizability (β) of the silver nanoparticles increases with particle size, [19, 26] which is in accord with the difference in the fluorescence enhancement between the nanoparticles with a 60 nm silver core and those with the 10 nm core. Fig 3 shows that the enhancement of the fluorescence is about a factor of 3-5 from 740 nm to 820 nm and then, from 820 nm, it starts to increase till the enhancement factor reaches a *maximum value of 20*.

The above enhancement method preserves all the advantages traditionally associated with two-photon fluorescence. The use of NIR radiation used ensures a large tissue penetration depth. Also, the "second harmonic" generated is highly localized, which is then absorbed only by the dye in the vicinity of the silver, thus we still get automatic image cross-sectioning, which is one of the biggest advantages of two-photon microscopy.[1-3] The localized excitation also minimizes photobleaching.

To determine the contribution of the other MEF effects, such as SPR, we tested silver nanoparticles with the rhodamine 6G dye, so as to see the effect of SPR on the enhancement of the fluorescence generated by the rhodamine dye molecules. Rhodamine and its derivatives (especially Rh-6G and Rh-B) are commonly used dyes that have been extensively utilized previously to study the metal enhanced fluorescence effects. [7, 9, 16, 36] The nanoparticles containing rhodamine dye were around 170 nm in size and contained 0.7% dye (by weight). We did not see much silver induced enhancement of the fluorescence signal emanating from the rhodamine dye. We observed a maximum fluorescence signal enhancement of 1.4 times, and 2.8 times, with the 10 nm, and 60 nm silver sphere, respectively. Thus SPR does not seem to be the major contributor to the overall enhancement we observed with HPTS. Notably, the absorption spectrum of the rhodamine does not overlap with the SH wavelength of the incident light, thus

enhancement due to HRS is excluded here. The comparison between the enhancement factor for HPTS and Rhodamine is shown in Table 1.

Nanoparticle size	60 nm silver		10 nm silver	
Dye	HPTS	Rhodamine (6G)	HPTS	Rhodamine (6G)
Maximum Enhancement Factor	20	2.8	2.2	1.4

Table 1:Comparison of fluorescence enhancement from HPTS and Rhodamine containing nanoparticle.

One point of interest here is the distance and the interaction between the HPTS dye and the silver nanospheres. To get a rough estimate of the distance between the dye molecules and the silver surface, we looked at the one-photon fluorescence enhancement. Here we observed a slight quenching of the fluorescence signal for our polyacrylamide coated silver containing dye, as compared to the free dye at equal concentration. The fluorescent signal intensity of our nanoparticle is about 80% that of the free dye at 405 nm. This indicates that the dye molecule is in very close proximity to the silver nanosphere surface as per the quenching/enhancement theory described before,[15] though the molecules may be in an altered orientation, they may not be quite "touching", which might have resulted in total quenching of the fluorescence (see more on this below). That the dye is physically adsorbed near the silver surface is also corroborated by the fact that we do not observe any dye leaching from the polyacrylamide nanoparticles

embedded with silver in them, whereas without the silver we get as much as 8% dye leaching under similar conditions.[34] Interestingly, we do not observe total quenching. This may be explained in two ways: (1) The silver nanospheres we used have a citrate capping; so the capping citrate molecules may prevent the dye molecules from getting totally quenched by helping to maintain a certain minimal distance between the metal and the dye; (2) The quenching may also depend on the orientation of the dye, with respect to the metal surface, so if the orientation of the dye is nearly perpendicular to the silver surface then it might prevent it from being totally quenched, even though it is still in close proximity to that surface. This distance between the dye and the silver surface is not optimal for our enhancement studies and the two-photon enhancement we get from our method could probably be much higher, upon optimization, than the factor of 20, which we observed. . Importantly, although the close distance between the dye and the metal surface causes some loss of fluorescence signal, it still prevents the dye from leaching, which is also a very significant point. We plan to address this question of optimal distance, to prevent any fluorescence quenching, yet to minimize the dye leaching, by using different techniques to control the distance between the dye and the silver, in a separate study. The lack of single photon enhancement for the HPTS nanoparticles with silver core further demonstrates that SPR effect is not so prominent. Thus it probably does not play a major role in the two photon fluorescence enhancement as well.

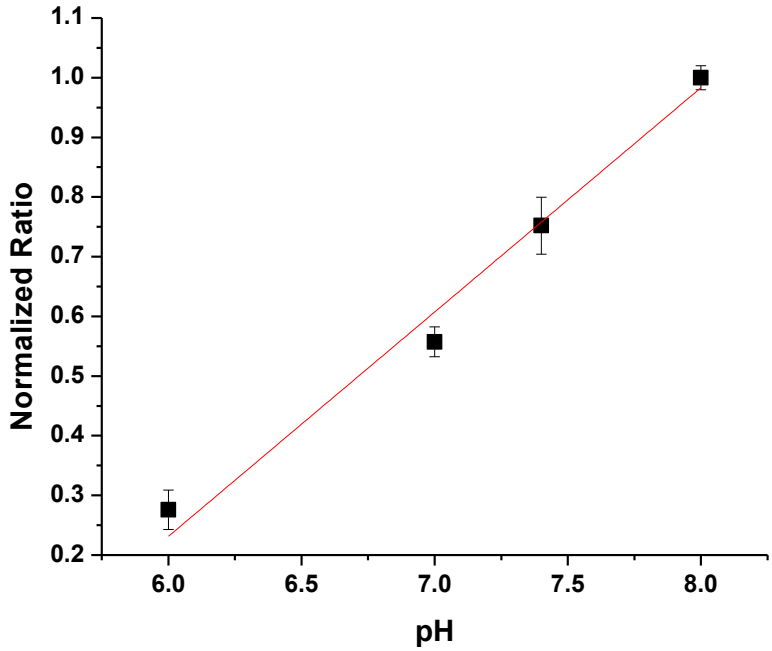

Figure. 4. The pH calibration curve of the nanoparticles. The curve is constructed by taking the ratio of the fluorescence when excited by 900 nm and 740 nm photons. We obtain an R^2 value of 0.98.

Intracellular pH mapping

We tested these nanoparticles for pH sensing in cells. As most of the drug delivery mechanisms depend on the pH, pH is an extremely important physiological parameter. Many anticancer drugs are designed to release their contents at low pH, and thus the knowledge of the exact pH inside the cells or tissues should be very helpful for drug design. The two-photon excitation spectra of the nanoparticles show a pH dependent peak at 900 nm. It corresponds to the single photon absorption peaks at 450 nm. The one-photon absorbance peaks of HPTS are highly pH sensitive. The absorption at 370 nm (between 350 nm and 410 nm) increases at lower pH, whereas the absorption at 450 nm (410 nm to 490 nm) decreases at lower pH. We observe a drastic pH

dependent change at 900 nm, but, contrary to the one-photon pH response, we do not see much change elsewhere around 800 nm, or for lower wavelengths. The fluorescence intensity ratio between the peaks of the two two-photon excitation wavelengths, at 900 nm and at an isosbestic point (740 nm), increases linearly over the pH range between 6.0 and 8.0, for these nanoparticle sensors. The pH calibration curve, based on the ratio of fluorescence intensities, with excitations at 900 nm and 740 nm, is shown in Fig 4. It is nearly linear, with an R^2 value of 0.98. We also checked the response of the nanoparticles to ions like K^+ and Na^+, which are abundantly present in the cell. This was done by using various concentrations (0 to 0.5M) of KCl and NaCl in a buffer solution. We did not observe any changes in the response of the nanoparticles to K^+ and Na^+ in these solutions.

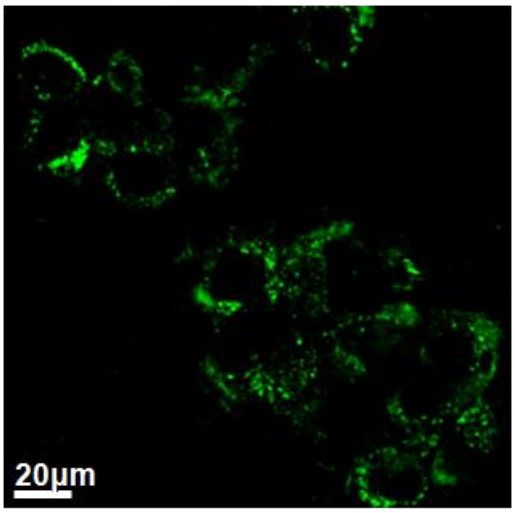

Figure.5.A two-photon fluorescence image of the MDA-MB-435 cells with pH sensing, core-shell nanoparticles, excited at 900 nm (The scale bar represents 20 µm). Monitored is the pH of the acidic endosomes/lysosomes in which the nanosensors are preferentially localized/trapped, in contrast to other cell locations.

The MDA-MB-435 cancer cells were incubated with the nanoparticles for three hours, then washed and used for imaging. The nanoparticles are taken up by endocytosis. A two-photon fluorescence image of the live MDA cells containing the nanoparticles is shown in Fig. 5. We take the ratio of the fluorescence intensity when excited at 900 nm and 740 nm, and obtain an average intracellular pH value of 6.5 ± 0.2, using the 60 nm silver core particles. The low pH value measured is probably because these nanoparticles are trapped in acidic vesicles such as late endosomes or lysosomes, which are acidic in nature. The absence of any targeting peptide on the nanoparticle surface precludes the involvement of receptor mediated endocytosis in the cellular uptake of the nanoparticles. However, the highly positive surface charge of the nanoparticles (~+18 mV by zeta potential) confers their strong affinity for the negatively charged cellular membrane, and promotes their uptake into the cell. Once endocytosed, the nanoparticles are destined for the lysosomes due to the absence of a targeting signal on their surface.

To check this preferential nanosensor trapping hypothesis we looked at the co-localization of the nanoparticles with the acidic compartments, using lysotracker. The lysotracker probes specifically stain the acidic compartments of the cells and have been widely used to visualize lysosomes, which are strongly acidic, relative to other compartments of the cell.[34] The fluorescence images were obtained by exciting the nanoparticles with 405 nm and 450 nm, and the lysotracker with 568 nm, while collecting the fluorescence emission at 510 nm and 600 nm, for the nanoparticle and lysotracker dye, respectively. The overlaid image is shown in Fig 6. We see significant co-localization of the nanoparticles with the acidic compartments. A rough estimate shows that about 50% of the nanoparticles are in acidic compartments. This estimation

was performed using the Image J software and comparing the pixel intensity of the red and green colors.

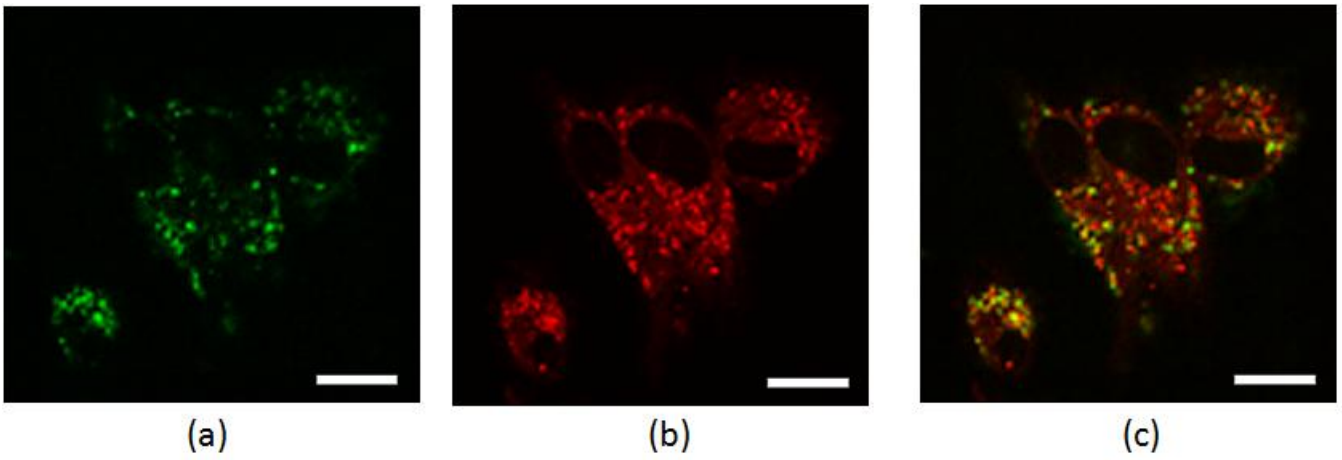

Figure. 6. Fluorescence images from the cells. (a) Fluorescence signal from the nanoparticles inside the MDA cells, (b) Fluorescence signal from the lysotracker dye used to stain the acidic vesicles and (c) Overlay of the fluorescence from nanoparticles (green) and the lysotracker (red). Orange/Yellow shows the position of nanoparticles overlapping with acidic vesicles. We see that many of the nanoparticles are inside acidic vesicles (Scale 20μm). This image was taken in the confocal mode.

Conclusions

We have demonstrated a large intensity enhancement in the two-photon fluorescence emission of HPTS dye molecules by silver nanospheres. The silver nanospheres and dye molecules were co-encapsulated inside the polyacrylamide hydrogel matrix of larger nanoparticles. We see a signal enhancement by a factor of 20 with 60 nm silver nanosphere cores, when excited at a wavelength of 900 nm. We also tested 10 nm silver nanosphere cores but observed an enhancement of only 2.2 times. This method can be employed for any dye having an absorption in the visible region.

The polymeric nanoparticle prevents silver NP aggregation, and thus any corresponding complicating optical effects; and the polymeric matrix also protects the silver and the dye from interacting with the proteins and other potentially interfering cell components. The embedding nanoparticle not only shields the silver and the dye but it potentially enables a long plasma lifetime, and even longer if used with a PEG coating,[32] as well as potential specific targeting to any type of cells, by surface engineering, such as attaching proper targeting moieties to the matrix.[32]

We applied this nanoparticle sensor to image the intracellular pH in MDA-MB-435 cancer cells. Our intracellular measurements show that most of these nanoparticles end up inside acidic endosomes and we obtain an average pH value of 6.5. Such nanosensors could further be used for work on live tissues *in-vivo*.

This technique enables one to benefit from all the advantages of multi-photon fluorescence, such as good penetration depth, highly localized excitation, low autofluorescence and high signal-to-noise ratio. Furthermore, the required multishell nanoparticle structure fits seamlessly with the recent development of smart nanoparticle based biosensors and nano-actuators, such as targeted, theranostic, multifunctional, biodegradable and bioeliminable nanoparticles for therapy, diagnostics and surgical delineation.[32]

Acknowledgements

This work was supported in part by NSF grant NSF-DMR 0455330 (RK). We thank Dr. Hoe Jin Hah for his help and useful discussions with nanosensor synthesis, Dr. Antek Wong-Foyfor his help during XRD measurements, Teppei Shirakura for his help during nanoparticle calibration, Jacquelyn Priestley for her help during synthesis of rhodamine nanoparticles and Leshern Karamchand for useful discussions about the uptake of nanoparticles in cells. We also thank Chris Edwards, Sasha Meshinchi and Dotty Sorenson at the Microscopy and Image-analysis Laboratory, the University of Michigan, for their technical support in confocal imaging and TEM imaging, respectively. The authors also thank Paul Lennon and James Windak at the Chemistry Instrument Shop, for their technical support while using the ICP machine and the UV-VIS spectrometer.

References

1. W. Denk, J. Strickler, W. Webb, *Science* **1990**, 248, 73–6.

2. F. Helmchen, W. Denk, *Nat. Methods* **2005**, 2 (12)**,** 932–40.

3. G. S. He, P. P. Markowicz, T. C. Lin, P. N. Prasad, *Nature* **2002**, 415, 767-770.

4. I. Cohanoschi, F. E. Hernandez, *J. Phys. Chem. B* **2005,** 109, 14506-14512.

5. H. Kano, S. Kawata, *Optics Letters* **1996**, 21, 1848-1850.

6. Y. Shen, J. Swiatkiewicz, T. C. Lin, P. Markowicz, P. N. Prasad, *J. Phys. Chem. B* **2002**, 106, 4040–4042 .

7. I. Gryczynski, J. Malicka, Y. Shen, Z. Gryczynski, J. R. Lakowicz, *J. Phys. Chem. B* **2002**, 106, 2191–2195.

8. J. Lukomska, I. Gryczynski, J. Malicka, S. Makowiec, J. R. Lakowicz, Z. Gryczynski, *Biochemical and Biophysical Research Communications* **2005,**328, 78-84.

9. A. M. Glass, A. Wokaun, J. P. Heritage, J. G. Bergman, P. F. Liao, D. H. Olson, *Phys. Rev. B* **1981**, 24, 4906–4909.

10. R. He, Y. Su, K. Cho, C. Lin, N. Chang, C. Chang, S. Chen, *Optics Express* **2009,** 17, 5987-5997.

11. W. Wenseleers, F. Stellacci, T. Meyer-Friedrichsen, T. Mangel, C. A. Bauer, S. J. K. Pond, S. R. Marder, J. W. Perry, *J. Phys. Chem. B* **2002**, 106, 6853–6863.

12. E. J. Sánchez, L. Novotny, X. S. Xie, *Phys. Rev. Letts.* **1999,** 82, 4014-4017.

13.L. Novotny, R. X. Bian, X. S. Xie, *Phys. Rev. Lett.* **1997**, 79, 645-648.

14. E. J. McLaurin, A. B. Greytak, M. G. Bawendi, D. G. Nocera, *J. Am. Chem. Soc.* **2009**, *131*, 12994–13001.

15. P. Anger, P. Bharadwaj, L. Novotny, *Phys Rev. Letts*.**2006**, 96, 113002:1-6.

16.K. Aslan, I. Gryczynski, J. Malicka, E. Matveeva, J. R. Lakowicz, C. D. Geddes, *Current Opinion in Biotechnology* **2005**, 16,55–62.

17. C. Lin, K. Chiu, C. Chang, S. Chang, T. Guo, S. Chen, *Optics Express* **2010**, 18, 12807-128170.

18. E. C. Hao, G. C. Schatz, R. C. Johnson, J. T. Hupp, *J. Chem. Phys.* **2002**, 117, 5963-5966.

19. P. C. Ray, *Chem. Rev.* **2010**, *110,* 5332–5365.

20.F. W. Vance, B. I. Lemon, J. T. Hupp, *J. Phys. Chem. B* **1998**, *102,* 10091-10093.

21.M. Chandra, A. M. Dowgiallo, K. L. Knappenberger Jr., *J. Phys. Chem. C* **2010**, 114, 19971–19978.

22. T. Itoh, Y. Ozaki, H. Yoshikawa, T. Ihama, H. Masuhara, *Appl. Phys. Lett*. **2006**, 88, 084102: 1-3.

23. R. C. Johnson, J. Li, J. T. Hupp, G. C. Schatz, *Chem. Phys. Letts.* **2002**, 356, 534–540.

24.A. Neely, C. Perry, B. Varisli, A. K. Singh, T. Arbneshi, D. Senapati, J. R. Kalluri, P. C. Ray, *ACS Nano.* **2009**, 3, 2834–2840.

25. A. K. Singh, D. Senapati, S. Wang, J. Griffin, A. Neely, P. Candice, K. M. Naylor, B. Varisli, J. R. Kalluri, P. C. Ray, *ACS Nano.* **2009**, 3, 1906–1912.

26. J. Griffin, A. K. Singh, D. Senapati, E. Lee, K. Gaylor, J. Jones-Boone, P. C. Ray, *Small* **2009**, 5, 839–845.

27. K. Aslan, M. Wu, J. R. Lakowicz, C. D. Geddes, *J. Am. Chem. Soc.**2007***, 129 (6), 1524–1525 .

28. K. Aslan, M. Wu, J. R. Lakowicz, C. D. Geddes, *Journal of Fluorescence* **2007**, 17, 127-131 .

29.H. A. Clark, P. J. Campagnola, J. P. Wuskell, , A. Lewis, L. M. Loew, *J. Am. Chem. Soc.***2000**, 122, 10234-10235.

30.P. J. Campagnola, H. A. Clark, W. A. Mohler, A. Lewis, L. M. Loew, *Journal of Biomedical Optics* **2001**, 6(3), 277–286.

31.H. A. Clark, M. Hoyer, M. A. Philbert, R. Kopelman, *Anal. Chem.* **1999**, 71, 4831-4836.

32. Y. E. Koo Lee, R. Smith, R. Kopelman, *Annu. Rev. Anal. Chem.* **2009**, 2, 57-76.

33. Y. E. Koo Lee, E. E. Ulbrich, G. Kim, H. Hah, C. Strollo, W. Fan, R. Gurjar, S. M. Koo, R. Kopelman, *Anal. Chem.* **2010**, 82, 8446-8455.

34. A. Ray, Y. E. Koo Lee, T. Epstein, G. Kim, R. Kopelman, *Analyst* **2011**, 136 (18), 3616 – 3622.

35. Y. Zhang, A. Dragan, C D. Geddes, *J. Phys. Chem. C* **2009,** *113*, 12095–12100.

36. M. R. Gartia, A. Hsiao, M. Sivaguru, Y. Chen and G. L. Liu, *Nanotechnology* **2011**, 22, 365203:1-11.

Chapter 4

Nanoprobe aided pH measurement *in vivo* using photoacoustics

Introduction

The pH level is one of the most important parameters in many physiological, pathological and therapeutic processes. Since pH is strictly regulated, abnormal pH levels can act as indicators for diseases or other bodily dysfunction. Deviations in pH may reflect body stress conditions such as inflammation, high exercise levels, interruption of normal blood supply, and bio-chemical shock. According to previous studies [1], a lower pH level is a typical characteristic of cancerous tissues, which also affects the delivery and effectiveness of drugs to the tumor [2]. Other clinical examples of anomalous tissue pH include arthritis [3] and wounds [4]. Thus monitoring the pH at tissue and intracellular level *in vivo* could help diagnose the severity of diseases and monitor disease progression, as well as treatment progression.

Several methods, including positron emission tomography (PET) [1, 5], magnetic resonance spectroscopy (MRS) and imaging (MRI) [1, 6] have been utilized previously for measuring the pH of tissues *in vivo*. Although they are very widely used, these methods have their own disadvantages such as high cost, low sensitivity and low temporal resolution. Additionally PET utilizes ionizing radiation which also limits its usage. Optical methods provide an alternate and attractive solution due to their low cost, non invasiveness, utilization of non-ionizing radiation and ability of continuous online monitoring of the dynamic pH changes. The optical pH

measurements are generally performed using exogenous contrast agents such as pH sensitive dyes, polymers or nanoprobess, by an intensity-based, ratiometric fluorescence excitation or emission method [7, 8] or by the fluorescence lifetime method [9]. However, due to the strong scattering of light in most biological tissues, conventional optical techniques such as fluorescence imaging have limited spatial resolution when working in a light diffusion regime. Combining the advantages of both light and ultrasound, the emerging biomedical photoacoustic technique has been extensively tried for its potential applications in both imaging and sensing [10, 11]. As an example, the feasibility of the photoacoustic technique for pH sensing and imaging has been previously demonstrated *in vitro* [12-14]. The molecular contrast agents used in previous studies, however, are not suitable for *in vivo* applications.

Here we demonstrate, for the first time, a ratiometric photoacoustic based method for *in vivo* pH sensing using pH sensitive nanoprobes. The nanoprobes consist of the pH sensitive dye seminaphthorhodafluor (SNARF) encapsulated in a polyacrylamide hydrogel matrix. The nanoprobes have a hydrophobic core and a hydrophilic surface, so as to efficiently trap the SNARF molecules inside. The polyacrylamide matrix protects the dye from interacting with the external proteins and cell organelles in the plasma, but allows free flow of ions and small molecules, such as O_2, through the matrix. As demonstrated in previous studies, the interaction of the pH sensitive dyes with different proteins often leads to an undesirable change in the optical properties of those dyes [15]. Therefore, by using the nanoprobe design, the optical and chemical properties of the pH sensitive dyes are better preserved in the complex *in vivo* environment, which is essential to achieve a quantitative evaluation of pH levels inside live biological samples. The polyacrylamide matrix of the nanoprobes is biocompatible, biodegradable, and can be

retained in the cytoplasm for days. Moreover, by surface modification and attachment of different peptides or antibodies, the nanoprobes can be targeted to specific cells or tissues [16]. This nanoparticle platform enables specifically targeted delivery of the unmodified SNARF dye. For specific targeting applications, the SNARF dye itself can also be modified to have different functional group as well, which can be used for attachment to targeting peptides or antibodies. However the SNARF dye with an attached functional group is significantly more expensive than the dye without the functional group. Furthermore, the direct attachment of the peptides to the dye often leads to unwanted changes in its optical characteristics and physical properties [17].

Experimental

Nanoparticle synthesis

The nanoprobes were prepared using a reverse micelle polymerization process [18]. The monomers acrylamide (689.5mg, 97%), 3- (aminopropyl)methacrylamide hydrochloride salt (APMA), the hydrophobic crosslinker (53.6mg, 3%), glycerol dimethacrylate (GDMA) (480 µL, 20%), and the dye SNARF (3mg) (Invitrogen, Carlsbad, CA)are added and emulsified in a surfactant solution of AOT (1.6g) and Brij-30 (3.3mL) in Hexane (45mL), before initiating the reaction using N,N,N’,N’-tetramethylethylenediamine (TEMED) (100 µL) and 10% (w/w) ammonium persulfate (APS) (100 µL). The reaction is allowed to continue for two hours and then hexane is removed by rotary evaporation, before washing the particles in ethanol and water several times in an amicon filter cell so as to remove the surfactants and any unreacted monomer. Acrylamide, methylene-bis-acrylamide (MBA), glycerol dimethacrylate (GDMA), dioctyl sulfouccinate (AOT), Brij 30, hexane, ammonium persulfate (APS), N,N,N’,N’-tetramethyl

ethylenediamine (TEMED). 3-(aminopropyl)methacrylamide hydrochloride salt (APMA) was obtained from Polysciences Inc. (Warrington, PA).

Result and Discussion

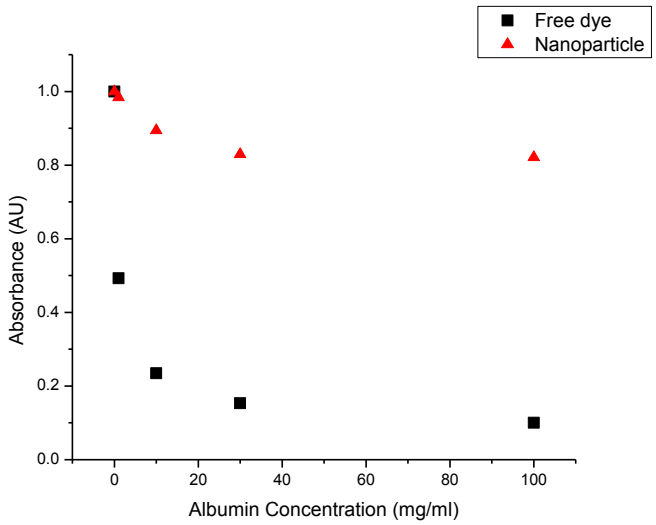

Figure 1: Interference with albumin. Changes in the absorption of the dye and the nanoprobe in presence of albumin.

The average size of the nanoprobes in aqueous medium was obtained by monitoring the dynamic light scattering and was measured to be 52 nm. They also had a surface charge of +18 mV, making them very suitable for cellular uptake. The amount of dye encapsulated in the nanoprobes was estimated by comparing the fluorescence from a known concentration of nanoprobes and the fluorescence calibration curve of free dye. We estimate that the nanoprobes encapsulate about 0.3% of the dye by weight. This result was further confirmed by comparing absorbance measurements from the dye and the absorption calibration curve. The presence of the hydrophobic functional group in GDMA and APMA makes the core hydrophobic, thus helps encapsulate the SNARF dye efficiently. For nanoprobes without GDMA, containing *N*,*N*′-

Methylenebisacrylamide, and lower amount of APMA, the amount of dye encapsulated inside the matrix was significantly lower (<5X). The dye leaching from the nanoprobes was tested in PBS and we did not observe any dye leaching even after 24 hours.

To demonstrate the effectiveness of the nanoprobe matrix for protecting the encapsulated dye, we studied the interaction of the SNARF free dye versus that of the nanoprobes containing the SNARF dye with albumin, a protein most abundantly presents in the blood and tissues. We observed that the free dye on interaction with albumin partially lost its color instantly. Its optical absorbance throughout the spectrum, from 500nm to 600nm, was reduced as much as 90% from the initial value, as shown in Fig 1. In comparison, the SNARF dye encapsulated in the nanoprobe matrix was protected from albumin well. A mild loss of less than 18% in optical absorbance was observed, even after 48 hours of incubation. The long term stability demonstrates good encapsulating benefited from the hydrophobic core of the nanoprobes which successfully prevented the dye from leaching out in the presence of albumin.

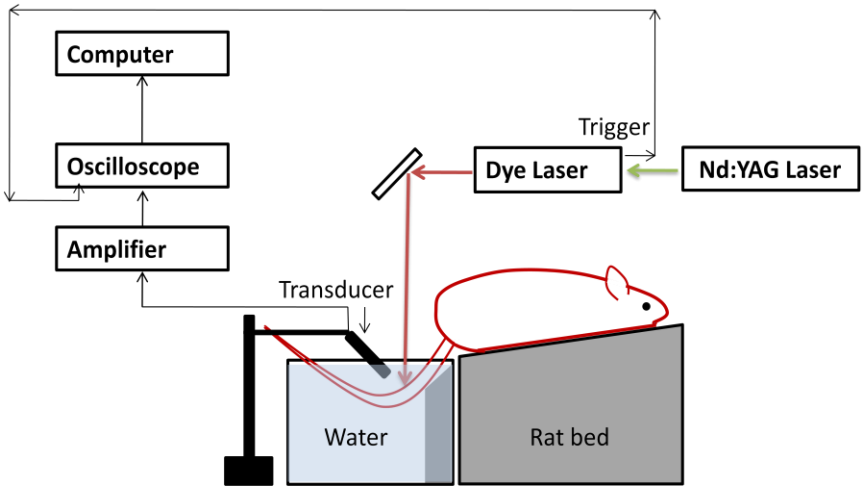

Figure 2: Schematic setup for the experiment on live rats.

The setup for spectroscopic photoacoustic measurement of pH level on live rats is shown in Fig. 2. A tunable dye laser (ND6000, Continuum) pumped by the second harmonic of a pulsed Nd:YAG laser (Powerlite, Continuum) was used to provide pulsed light with a pulse width of 5 ns and pulse repetition rate of 10 Hz. The two wavelengths used for spectroscopic measurement were 565 nm and 580 nm. Light fluence of about 5.1 mJ/cm^2 at 580 nm, and of 3.8 mJ/cm^2 at 565 nm was used to generate photoacoustic signals. These light fluence are much lower than the ANSI safety limit for human skin. Before *in vivo* experiments on live rats, we first acquired a pH calibration curve through the *in vitro* experiment on phantoms. The nanoprobes containing the pH sensitive dye was injected, using a syringe pump, into a section of transparent soft tubing (0.58 mm- BD Intramedic, Sparks, MD, USA) mimicking a blood vessel. The photoacoustic signal created from the nanoprobes in the tubing was detected by a high-sensitivity and wide-bandwidth (132.63% at - 6 dB with a center frequency of 9.01 MHz) ultrasonic transducer (V312, Panametrics). The transducer was cylindrically focused on the tubing with a focal length of 0.75 inch. The signals received by the transducer were amplified and digitized by a 500 MHz digital oscilloscope (TDS 540B, Tektronix) before being transferred to a computer. For each data point, the signal averaging was performed over 30 measurements to improve the signal-to-noise ratio. As shown in Fig. 3, the ratio between the photoacoustic signal intensities at the two wavelengths, i.e. 580 nm and 565 nm, increases linearly in the pH range from 6.0 to 8.0.

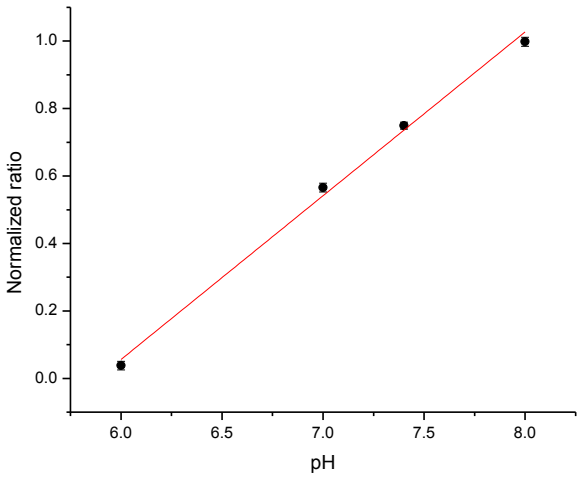

Figure 3: *In vitro* pH calibration curve. The calibration curve was obtained by taking the ratio of the photoacoustic signal intensities when the nanoprobes were illuminated at 580nm and 565nm, respectively.

To examine whether photoacoustic measurement of pH level can be achieved in an *in vivo* environment, experiments were performed on a rat joint model (Sprague Dawley, 100 g body weight, Charles River Laboratory). During the whole experiment, the rats were anesthetized using isoflurane. To prevent motion, the rat was placed on a pad and its tail was fixed firmly on a 45º inclined platform. Both the rat tail and the transducer were placed in water for ultrasound coupling. The nanoprobes (200 μL) containing the pH sensitive dye were injected locally into a tail joint. The center of the joint space was 2-3 mm deep from the skin surface of the tail. Before injection, the nanoprobe solutions were prepared by suspending them in deionized water (pH 7) and pH buffer (pH 8) respectively, leading to a dye concentration of 300 microgram/ml. The spectroscopic photoacoustic measurement of the pH level in the target tail joint was conducted by illuminating the collimated light beam, at 580nm and 565nm wavelengths respectively, on the surface of the tail and pointing the ultrasonic transducer to the illuminated area. Then photoacoustic signals, correspondent to the two wavelengths, were recorded from the joint area, an example shown in Fig. 4. By subtracting the signal before nanoprobe injection from the signal

after injection, the background photoacoustic signal from the joint tissue was removed. The local pH level in the joint was then determined by comparing the ratio of the photoacoustic signal intensities at the two wavelengths with the *in vitro* calibration curve in Fig. 3. Before computing the ratio, the difference in tissue optical attenuation between the two wavelengths was also compensated using the tissue optical parameters from the literature [19]. The average pH levels were 7.1± 0.1 in the tail joints with injected nanoprobe solution in de-ionized water (pH 7); while the average pH levels were 7.8±0.1 in the tailed joints with injected nanoprobe solution in pH buffer (pH 8), both close to the respective preset pH level of the solution. The small deviation between photoacoustic measurements and the preset values may be attributed partially to the mixing of the nanoprobe solution with the joint fluid.

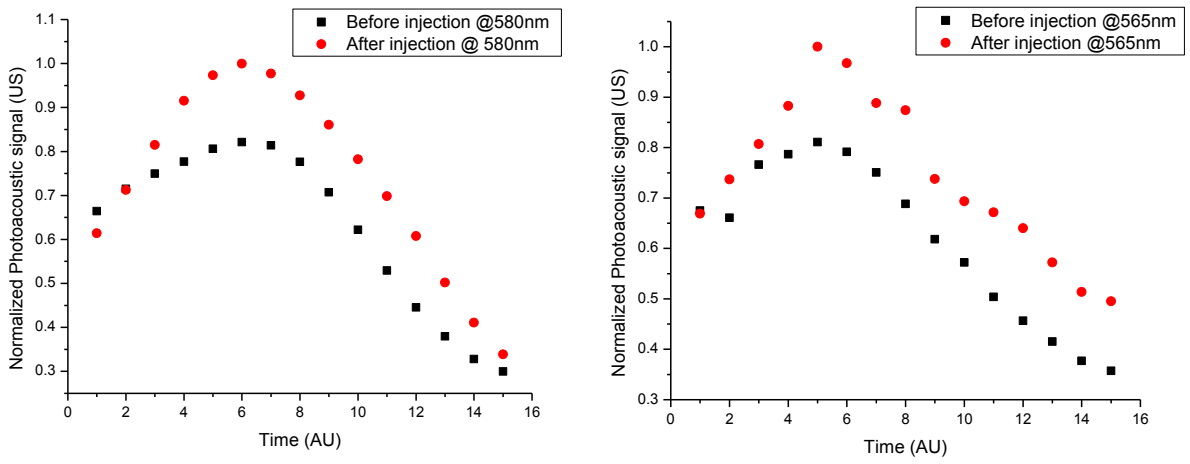

(a) (b)

Figure 4: Photoacoustic signals at (a) 580nm and (b) 565nm, respectively, from a rat tail joint, before and after the local injection of the pH sensitive nanoprobes.

Conclusion

We demonstrated, for the first time, through the experiments on phantoms and live animals, the feasibility of quantifying pH level using ratiometric intensity based spectroscopic photoacoustic measurement facilitated with pH sensing nanorpobes. Our results show that the properties of the dye in its free form get severely altered in the presence of albumin. In comparison, the nanoprobes, consisting of polyacrylamide matrix with a hydrophobic core and a hydrophilic surface, largely prevent the interaction of the dye with proteins appearing prevalently in the *in vivo* environments. Preserving the optical properties of the pH sensitive dye while sustaining its chemical properties is crucial for successful application of this technology to live biological samples. Through the *in vitro* experiments on phantoms, a calibration curve was generated, which further enabled successful pH sensing *in vivo* on a rat joint model.

Acknowledgements

The authors would like to acknowledge NIH grant R21CA160157, R01AR060350 and R01AR055179, NSFC grant 11028408, and SPIE student scholarship for funding the research.

References

1. X. Zhang, Y. Lin and R. J. Gillies, *J Nucl Med* 2010, **51** (8), 1167-1170.

2. O. Trédan, C. M. Galmarini, K. Patel, I.F. Tannock, *J Natl Cancer Inst* 2007, **99**, 1441–54.

3. S. E. Andersson, K. Lexmüller, A. Johansson and G. M. Ekström, *J Rheumatol*. 1999, **26**(9), 2018-24.

4. L. A. Schneider, A. Korber and S. Grabbe, J. Dissemond, *Arch Dermatol Res*. 2007, **298**(9), 413-20 .

5. A. L. Vāvere, G. B. Biddlecombe, W. M. Spees, J. R. Garbow, D. Wijesinghe, O. A. Andreev, D. M. Engelman, Y. K. Reshetnyak and J. S. Lewis, *Cancer Res.* 2009, **69**(10),4510-6.

6. F. A. Gallagher, M. I. Kettunen, S. E. Day, D. E. Hu, J. H. Ardenkjær-Larsen, R. Zandt, P. R. Jensen, M. Karlsson, K. Golman, M. H. Lerche and K. M. Brindle, *Nature* 2008, **453**, 940-943.

7. G. Helmlinger, F. Yuan, M. Dellian and R. K. Jain, *Nature Medicine* 1997, **3**, 177 – 182

8. A. Ray, YE Koo Lee , G. Kim and Kopelman R, *Small* 2012, **8**(14),2213-21.

9. C. Hille, M. Berg, L. Bressel, D. Munzke, P. Primus, H. G. Löhmannsröben and C. Dosche, *Anal. Bioanal. Chem.*, 2008, **391**, 1871–1879.

10. M. Xu and L. V. Wang, Photoacoustic imaging in biomedicine, *Rev. Sci. Instrum.* 2006, **77**, 041101.

11. A. Ray, J. Raijan, Y.E. Koo Lee, X. Wang and R. Kopelman, *Journal of Biomedical Optics*, 2012, **17** (5), 057004.

12. T. D. Hovrath, G. Kim, R. Kopelman, and S. Ashkenazi, *Analyst* 2008, **133**, 747– 749.

13. B. Schlageter, *Sens. Actuators B* 1997, **38–39**(3), 443–447.

14. M. R. Chatni, J. Yao, A. Danielli, C. P. Favazza, K. I. Maslov, and L. V. Wang, *Journal of Biomedical Optics* 2011, **16**(10), 100503-1 to 4.

15. S. Egginton, E. W. Taylor and J. A. Raven, Cambridge University Press, 1999, 521623170.

16. A. Ray, X. Wang, Y. E. Koo Lee, H. J. Hah, G. Kim, T. Chen, D. A. Orringer, O. Sagher, X. Liu and R. Kopelman, *Nano Research* 2011, **4**(11), 1163-1173.

17. O. Guryev, B. Abrams , C. Lomas , Q. Nasraty , E. Park, and T. Dubrovsky, *Anal. Chem.*, 2011, ***83*** (18), 7109–7114

18. A. Ray, Y. E. Koo Lee, T. Epstein, G. Kim and R. Kopelman, *Analyst* 2011, **136,** 3616-3622.

19. W. F. Cheong, S. A. Prahl and A. J. Welch, *IEEE J. Quantum Electronics* 1990, **26,** 2166-2185.

Chapter 5

Oxygen sensing *in vivo* using photoacoustics

This chapter has been adapted with minor modifications from the following published article:

A. Ray, J. Raijan, Y. E. Koo Lee, X. Wang and R. Kopelman, "Lifetime based photoacoustic oxygen sensing *in-vivo*" *Journal of Biomedical Optics*, 17 (5), 057004 (2012).

Introduction

Oxygen plays a key role in the energy metabolism of living organisms. Hypoxia is a condition where the body or a particular region of a body has less than adequate oxygen; while hypoxemia refers to a low level of oxygen in the blood. Depending on the severity of the hypoxia or hypoxemia, it may lead to complications such as unconsciousness, seizures, coma and even death[1,2]. Hypoxia is also a very important factor in tumor biology as it is very prominent in tumor tissues. It is a common characteristic of locally advanced solid tumors and has been revealed to promote angiogenesis, tumor aggressiveness, local recurrence and metastasis[3,4,5]. Hypoxia is also known to impede the effectiveness of different therapies such as photodynamic therapy, radiotherapy and chemotherapy[5,6,7].

Several methods have been developed to monitor oxygenation *in vivo* . One of the most commonly used techniques involves polarographic electrodes[6]. However, this technique is invasive in nature and also has the tendency to consume oxygen from the surroundings. Other

non-invasive methods such as MRI[8], PET[9] and phosphorescence[10,11,12,13,14] have also been explored previously. Although these techniques have a fairly high degree of success there are drawbacks. PET is expensive, with limited availability, and utilizes ionizing radiation, which can be harmful to the body. MRI is also fairly expensive and cannot be used for patients with implants or pacemakers. Neither can be very conveniently used. They are also not suitable for continuous online monitoring of oxygen concentration. The use of phosphorescent oxygen indicator dyes is highly attractive, due to its high sensitivity and ability for continuous monitoring of rapid kinetic changes in the surrounding oxygen level, and also due to the relative simplicity and low-cost of optical techniques. These dyes can be used to determine the oxygen level quantitatively, by monitoring the change in the upper (excited) state lifetime or the change in the absolute phosphorescence intensity. Monitoring the upper state lifetime of the dye is more desirable because it eliminates errors due to variations in dye concentration, absolute signal calibrations, autofluorescence, light scattering, etc., or, alternatively, the requirement for a good reference dye.

Although the standard optical phosphorescence and fluorescence techniques are highly sensitive and reliable, they suffer from low penetration depth due to the strong optical attenuation in tissues, especially blood. Moreover, the autofluorescence from tissues also poses potential problems. In comparison to conventional optical florescence techniques, photoacoustic imaging (PAI), combining the merits of both light and ultrasound, can lead to much better penetration depth, of up to a few centimeters, while preserving high spatial resolution[15]. PAI does not require the use of ionizing radiation, as do some of the other imaging modalities.

Oxygenated- and deoxygenated-hemoglobin, the two major chromospheres in the blood, have distinct optical absorption spectra in the spectral range from visible to near-infrared.

Therefore, PAI, when performed in a spectroscopic way by using multiple wavelengths, could evaluate the blood oxygen saturation based on the endogenous contrast between the two forms of hemoglobin, without using any contrast agent[16, 17]. However due to the strong optical attenuation of biological tissue, which is also a function of laser wavelength, the distribution of light fluence in a sample is strongly heterogeneous in most cases, especially when the imaged sample has a large scale and a complicated morphological structure. Inaccurate prediction of light fluence in the sample, at the wavelengths for spectroscopic imaging, strongly affects the accuracy of PAI in quantifying blood oxygen saturation based on the endogenous optical contrast. Thus in most deep tissue applications, the hemoglobin-based spectroscopic photoacoustic measurements of blood oxygenation can achieve only limited accuracy.

Here we demonstrate the technique of photoacoustic lifetime (PALT) measurement using an oxygen sensitive dye to quantify the oxygen concentration in biological tissues *in vivo* . Unlike the spectroscopic PAI measurements based on the endogenous contrast, this technique can evaluate the oxygen concentration in not only blood but also other media, such as water, as well as blood-devoid tissues. Moreover, since the PALT measurement is focused on the exponential decay curve that gives the lifetime of the indicator agent, rather than the absolute photoacoustic signal intensity from the indicator agent, the PALT based measurement of oxygen saturation is not affected any more by the heterogeneous optical properties and the inhomogeneous light fluence in the background.

The technique of photoacoustic lifetime measurement of indicator dyes was first developed in our lab[18]. A porphyrine based dye, Pt(II)octaethylporphine, was used for the purpose of *in-vitro* oxygen sensing. However this particular dye has an absorption at 532 nm, which would severely limit the penetration depth for any *in vivo* measurements, as a result of the strong

light scattering and absorption in the visible spectrum region. Moreover, the dye was not soluble in aqueous solution and therefore not readily applicable for biological applications. This technique was further developed with an oxygen sensitive water-soluble methylene blue dye[19] that has an absorption peak at 660 nm, enabling improved imaging depth in optically scattering tissues. However, often the methylene blue dye, in its free form, gets degraded into an inactive leuko (white) form in the body, by the ubiquitous cellular coenzymes, NADH and FADH [20, 21] . Both the previous studies on oxygen sensing using methylene blue and PtOEP had been limited to *in vitro* applications.

To validate the feasibility of this technique for *in vivo* measurements of oxygenation, we used Pd-tetra-(4-carboxyphenyl) tetrabenzoporphyrin dendrimer (G2) (from Oxygen Enterprises Ltd., Philadelphia, PA) as an oxygen sensing dye [10,11,12,13,14]. The G2 dye is based on a dendrimer with a Pd-tetrabenzoporphyrin core. The G2 dye, and a newer variant of the same dye, have previously been used for oxygen mapping in tumors *in vivo* [10,22]. It has a ground state absorption maximum at 630 nm. Once the dye is excited to an intermediate triplet state, it has a relatively long lifetime (~250 microseconds), before relaxing to the ground state by a parity-forbidden transition mechanism. However, in the presence of oxygen, the lifetime of this dye at its excited triplet state gets shortened. In PALT measurements, we first excite the dye with a pump beam at 630 nm and then use a probe beam at 950 nm to measure its transient absorption in the excited triplet state. The excited triplet state absorption at 950 nm depends on the phosphorescent lifetime and the delay between the pump and the probe beams. By changing the time delay between the pump and the probe beams, an exponentially decaying photoacoustic amplitude curve can be obtained. Evaluating the upper state lifetime of the indicator dye by a series of photoacoustic measurements facilitates a quantitative assessment of the oxygen concentration in the medium containing the dye.

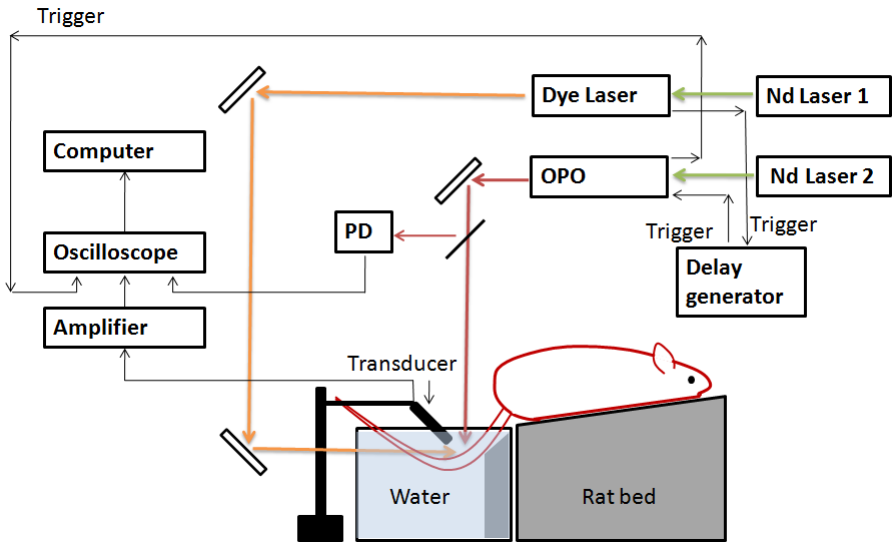

Fig. 1: The schematic of the experimental setup. PD: Photodiode, OPO: Optical parametric oscillator, Nd Laser: Second harmonic of Nd:YAG laser. The dye laser is used to trigger the delay generator which, in turn, triggers the OPO after a set delay. The acoustic signal corresponding to different delay times is measured using the transducer.

Experimental

The schematic of the experimental setup is shown in Fig 1. A tunable dye laser (ND6000, Continuum) pumped by the second harmonic of a pulsed Nd:YAG laser (Powerlite, Continuum) was used as a pump beam to provide pulsed light, with a pulse width of 5 ns, at a wavelength of 630 nm. The probe beam at 950 nm, with pulse duration of 5.5 ns, was generated using an optical parametric oscillator (Vibrant B, Opotek) pumped by the second harmonic of another Nd:YAG laser (Brilliant B, BigSky). Both the probe beam and pump beam were operated at a 10 Hz repetition rate. During PALT measurement, the pump beam and the probe beam illuminate the same object, with incident light energy densities of about 18mJ/cm^2 which is lower than the ANSI safety limit. A delay generator (DG535, Stanford Research Systems) was used to precisely control the delay between the pump (dye laser) and the probe (OPO) beams. The photoacoustic signals created by the two beams, respectively,

were detected by a high-sensitivity, wide-bandwidth (133% at -6 dB with a center frequency of 10 MHz) ultrasonic transducer (V312, Panametrics) that was cylindrically focused with a focal length of 0.75 inch. The signals received by the transducer were amplified and then digitized by a 500 MHz digital oscilloscope (TDS 540B, Tektronix) before being transferred and stored in a computer. The signal averaging was performed over 30 measurements, for each data point. A beam splitter was used to direct a small fraction of the beam from the OPO to the photodiode (Model 2031, Newport Corporation), which was used to normalize the measured photoacoustic signal intensity so as to take into account any error due to fluctuations in the OPO output power.

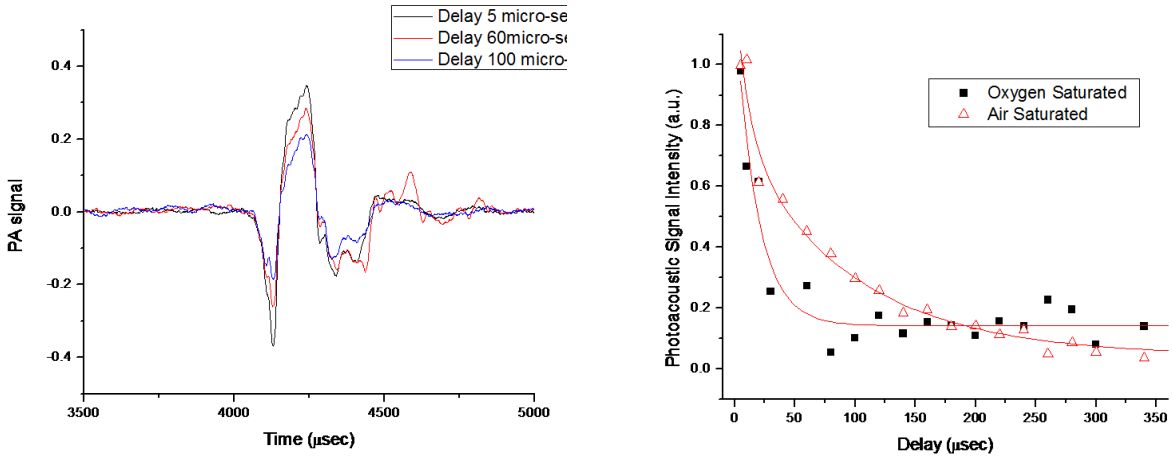

Fig. 2. (a) The photoacoustic (PA) signals from the G2 dye dissolved in water (containing 6% albumin), correspondent to different pump-probe delays. (b) The *in-vitro* change in the photoacoustic amplitude with time. The exponential decay curves for oxygen saturated water and air saturated water, mixed with albumin, are shown for comparison.

Result and Discussion

We first checked the feasibility of the PALT for oxygen sensing using the G2 dye *in-vitro*. We dissolved the dye in water containing 6% albumin. The G2 dye binds to albumin and the

resultant absorbance and fluorescence gets significantly enhanced[12, 13]. During photoacoustic measurement, the G2 dye solution was injected, using a syringe pump, into a transparent soft tubing (0.58 mm- BD Intramedic, Sparks, MD, USA), mimicking a blood vessel. The photoacoustic signal from the dye, in response to the probe beam, was measured for a series of time delays, varying from 0 to 350 microseconds. Examples of the photoacoustic signals for delays of 5, 60 and 100 microseconds are shown in Fig 2a, where a significant change in signal amplitude, as a function of the delay time, can be seen. By reading the peak-to-peak signal amplitude for each delay time, a delay curve can then be drawn, as shown in Fig. 2b. To demonstrate the feasibility of the G2 dye for oxygen sensing, the delay curves of the dye in two different media were measured, one in normal air-saturated water and the other in oxygen-saturated water prepared by purging with pure oxygen gas. The phosphorescence lifetime of the dye is about 250 microsecond in nitrogen-saturated water [11,12] and decreases with increase in oxygen concentration.

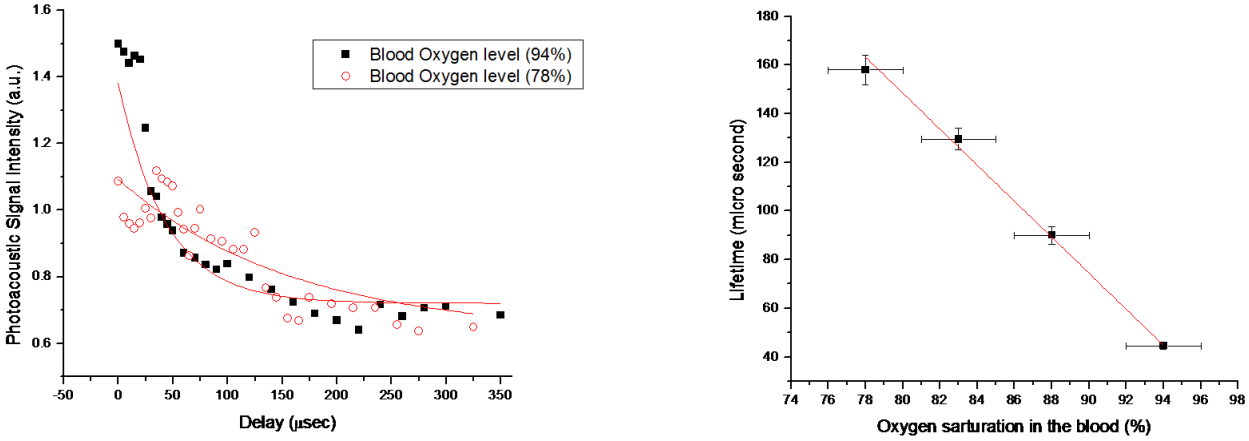

Fig. 3: (a) The *in vivo* change in the photoacoustic amplitude with time. The exponential decay curves for two different levels of oxygen saturation are shown. (b) The change in the upper-state lifetime of the dye measured with PALT for different blood oxygen saturations (R sq value: 0.99).

The *in vivo* experiments were performed on live Sprague Daley Rats (100 g, Charles River Laboratory). Before measurement, general anesthesia was administered to the rat by an intramuscular injection of 87 mg/kg Ketamine plus 13 mg/kg Xylasine. During the experiment, the rat was placed on a heating pad and its tail was fixed firmly on a 45^{o} inclined platform in a water tank, to prevent motion. One lateral vein of the rat tail was identified, and a catheter (24 gauge, 19 mm long, BD Angiocath, Sandy, Uta) was placed for systemic administration of the dye solution. By illuminating the light beam at the ventral surface of the tail and pointing the ultrasonic transducer to the illuminated area, PALT measurement of blood oxygenation was conducted on the ventral caudal artery in the rat tail. At the same time, the arterial blood oxygenation level was also monitored by a tail sensor of a pulse-oximeter (NONIN, 8500A, Plymouth, MN) that was attached over the ventral caudal artery. The time-averaged readout of blood oxygen saturation from the pulse-oximeter provided a gold standard to validate the PALT results. The heart rate of the rat was also monitored continuously, using the pulse-oximeter, showing that the rat was in good condition during the course of the experiment.

The dye solution was prepared by dissolving the G2 dye in Phosphate Buffer Saline (PBS) at a concentration of 5 mg/ml. We injected 0.9 ml of the dye solution into the circulatory system of the rat, to have a final dose of 45mg per Kg body weight. During the experiment, the rat breathed through a breathing mask. By changing the content of the oxygen in the breathing gas, the global arterial oxygenation level of the rat was changed over different levels (77%, 83%, 88% and 94%), with 94% corresponding to the normal blood oxygen level. No measurement was conducted below 77% since severe hypoxia could lead to the death of animals. At each arterial oxygenation level, the photoacoustic signal amplitude was measured, as a function of the delay time between the pump and the probe beams. The PALT decay curves correspondent to the two different blood oxygenation levels, 94% and 77%, are

shown, as examples, in Fig 3a. We performed two sets of measurements for each injection. We also monitored the photobleaching and the elimination of the dye from the animal for the duration of experiment by monitoring the photoacoustic signal of the dye from the tail vein. Over the time of measurement these parameter changes were almost negligible but were still taken into account by incorporating the photobleaching/elimination time constant, during final analysis. The upper state lifetimes of the dye, for four different blood oxygen concentrations, as measured with PALT, are shown in Fig 3b. The lifetime measured with PALT shows a good linear relationship with the blood oxygenation level. The signal averaging was performed over 30 measurements, for each data point, while obtaining the exponential decay curve as shown in Fig 2b and 3a. Whereas each data point in Fig 3b shows the average of the lifetime measurement calculated from two sets of data that were obtained for the same blood oxygen concentration. The horizontal error bars are from the pulse oxymeters. During our measurement the blood oxygen level was fairly constant with occasional fluctuations, as shown by the error bar in Fig 3b. The observed lifetimes obtained using PALT are slightly longer than the reported phosphorescent lifetimes. This discrepancy can be attributed to the relatively low quantum yield of the dye (~10%). PALT is measuring the depletion of the excited state, rather than strictly the radiant transition, like phosphorescence. Thus the lifetimes measured using the two different techniques should not be quantitatively compared. However the important aspect is that the lifetime decreases with increase in oxygen concentration, which is quite consistent with the phosphorescence.

This system can further be modified for *in vivo* 3-dimensional mapping of oxygen. For our current measurement we used a single transducer, which essentially focuses on one spot and obtains the lifetime measurement in that region. 3D imaging can be achieved through a 2D raster scan of a single transducer, which, however, takes a long time for data acquisition. In order to improve the speed for 3D PALT, a 2D transducer array should be used, which could

enables the acquisition of a 3D image after a single laser pulse. In that case, 3D PALT could be conducted with the similar speed as in this study focused on one point.

Conclusion

In conclusion, we demonstrated, for the first time, through experiments on live animals, the feasibility of quantifying blood oxygenation by using PALT measurements facilitated with an oxygen sensing dye. The measurements from the rat tail artery indicated that the lifetime of the dye quantified with the PALT technique showed a linear relationship with the blood oxygenation levels in the targeted artery. Unlike the spectroscopic PAI based on endogenous contrast, the PALT technique is not dependent on the optical absorption of hemoglobin for the oxygen level measurement. Therefore, this technique can be further extended to measure the oxygen concentration in any other media. This makes it a potentially powerful tool to evaluate oxygenation levels in tissues that are devoid of blood, such as the necrosis core of a solid tumors. With its high resolution and good imaging depth, PALT holds promise for evaluation of tumor hypoxia which is usually very heterogeneous in nature.

Acknowledgements

This work was supported by NIH grants R33CA125297 (RK), R01AR055179 (XW) and R01AR060350 (XW), and NSFC grant 11028408 (XW).

References

1. K. A. Krohn, J. M. Link and R. P. Mason, "Molecular Imaging of Hypoxia," *J Nucl Med* 49, 129S–148S (2008).

2. R. M. Schwartzstein and M. J. Parker, "Respiratory Physiology: A Clinical Approach," Lippincott Williams & Wilkins, Philadelphia (2005).

3. S. D. Young, R. S. Marshall and R. P. Hill, "Hypoxia induces DNA overreplication and enhances metastatic potential of murine tumor cells," *Proc. Nat. Acad. Sci. U.S.A.* 85, 9533-9537 (1988).

4. G. L. Semenza, "Regulation of hypoxia-induced angiogenesis: a chaperone escorts VEGF to the dance," *J. Clin. Invest.* 108, 39-40 (2001).

5. J. M. Arbeit, J. M. Brown, K. S. C. Chao, J. D. Chapman, W. C. Eckelman, A. W. Fyles, A. J. Giaccia, R. P. Hill, C. J. Koch, M. C. Krishna, K. A. Krohn, J. S. Lewis, R. P. Mason, G. Melillo, A. R. Padhani, G. Powis, J. G. Rajendran, R. Reba, S. P. Robinson, G. L. Semenza, H. M. Swartz, P. Vaupel and D. Yang, "Hypoxia: importance in tumor biology, noninvasive measurement by imaging, and value of its measurement in the management of cancer therapy," *Int. J. Radiat. Biol.* 82, 699-757 (2006).

6. M. Nordsmark, S. M. Bentzen, V. Rudat, D. Brizel, E. Lartigau, P. Stadler, A. Becker, M. Adam, M. Molls, J. Dunst, D. J. Terris and J. Overgaard, "Prognostic value of tumor oxygenation in 397 head and neck tumors after primary radiation therapy. An international multi-center study," *Radiother. Oncol.* 77, 18–24 (2005).

7. R. E. Durand, "The influence of microenvironmental factors on the activity of radiation and drugs," *Int J Radiat Oncol Biol Phys.* 20(2), 253-8 (1991).

8. V. D. Kodibagkar, X. Wang, J. Pacheco-Torres, P. Gulaka, R. P. Mason, "Proton imaging of siloxanes to map tissue oxygenation levels (PISTOL): a tool for quantitative tissue oximetry," *NMR Biomed.* 21, 899-907 (2008).

9. P. Zanzonico, J. O'Donoghue, J. D. Chapman, R. Schneider, S. Cai, S. Larson, B. Wen, Y. Chen, R. R. Finn, S. Ruan, L. Gerweck, J. Humm and C. Ling, "Iodine-124-labeled iodo-azomycin-galactoside imaging of tumor hypoxia in mice with serial microPET scanning," *Euro. J. Nucl. Med. Mol. Imag.*, 31, 117-128 (2004).

10. I. Dunphy, S. A. Vinogradov and D. F. Wilson, "Oxyphor R2 and G2: phosphors for measuring oxygen by oxygen-dependent quenching of phosphorescence," *Anal. Biochem.* 310, 191-198 (2002).

11. L. S. Ziemer, W. M. F. Lee, S. A. Vinogradov, C. Sehgal and D. F. Wilson, "Oxygen distribution in murine tumors: characterization using oxygen-dependent quenching of phosphorescence," *J. Appl. Physiol.* 98, 1503–1510 (2005).

12. D. F. Wilson, W. M. F. Lee, S. Makonnen, O. Finikova, S. Apreleva and S. A. Vinogradov, "Oxygen pressures in the interstitial space and their relationship to those in the blood plasma in resting skeletal muscle," J. Appl. Physiol. 101, 1648-1656 (2006).

13. A. Y. Lebedev, A. V. Cheprakov, S. Sakadzic, D. A. Boas, D. F. Wilson and S. A. Vinogradov, "Dendritic phosphorescent probes for oxygen imaging in biological systems," *Acs Appl. Mater. Interfaces* 1, 1292-1304 (2009).

14. M. A. Yaseen, V. J. Srinivasan, S. Sakadzic, W. Wu, S. Ruvinskaya, S. A. Vinogradov and D. A. Boas, "Optical monitoring of oxygen tension in cortical microvessels with confocal microscopy," *Opt. Express* 17, 22341-22350 (2009).

15. M. Xu and L. V. Wang, "Photoacoustic Imaging in biomedicine," *Rev. Sci. Instrum.* 77, 041101 (2006).

16. E. W. Stein, K. Maslov and L. V. Wang, " Noninvasive, *in vivo in vivo* imaging of blood-oxygenation dynamics within the mouse brain using photoacoustic microscopy," *J. Biomedical Optics*, 14 (2), 020502-1 to 3 (2009).

17. J. Laufer, C. Elwell, D. Delpy and P. Beard, "*In vitro* measurements of absolute blood oxygen saturation using pulsed near-infrared photoacoustic spectroscopy: accuracy and resolution," *Phys. Med. Biol.* 50 4409 (2005).

18. S. Ashkenazi, S.W. Huang, T. Horvath, Y.E. Koo Lee and R. Kopelman, "Photoacoustic probing of fluorophore excited state lifetime with application to oxygen sensing," *J. Biomed Opt.* 13(3), 034023 (2008).

19. S. Ashkenazi, "Photoacoustic lifetime imaging of dissolved oxygen using methylene blue," *J. Biomed Opt.* 15(4), 040501 (2010).

20. M. Wainwright, "Non-porphyrin photosensitizers in biomedicine," *Chem. Soc. Rev.* 5, 351-359 (1996).

21. D. Gabrielli, E. Belisle, D. Severino, A. J. Kowaltowski and M. S. Baptista, "Binding, aggregation and photochemical properties of methylene blue in mitochondrial suspensions," *Photochem Photobiol*. 79(3), 227-32 (2004).

22. T. V. Esipova, A. Karagodov, J. Miller, D. F. Wilson, T. M. Busch, and S. A. Vinogradov, "Two New "Protected" Oxyphors for Biological Oximetry: Properties and Application in Tumor Imaging," *Anal. Chem., 83* (22), 8756–8765 (2011).

Chapter 6

Nano-Contrast Agent for Brain Tumor Delineation using Photoacoustic

This chapter has been adapted with minor modifications from the following published article: A. Ray, X. Wang, Y. E. Koo Lee, H. J. Hah, G. Kim, T. Chen, D. A. Orringer, O. Sagher, X. Liu and R. Kopelman, "Targeted blue nanoparticles as photoacoustic contrast agent for Brain tumor delineation", *Nano Research,* Vol. 4, Issue 11, 1163-1173 (2011).

Introduction

For most patients affected by brain tumors, surgical excision is one of the core components of treatment. Of the several types of brain tumors, such as craniopharyngiomas, ependymomas, medulloblastomas and meningiomas, gliomas are the most common type of primary brain tumor especially in adults. The quality of life and survival of patients depends, in part, on the extent of surgical resection of the brain tumors [1]. During surgical resection, identifying the tumor boundary by eye can be misleading due to the heterogeneous nature and indistinguishable appearance of the glioma. Pre-operative images of the tumor, obtained by MRI (magnetic resonance imaging) or CT (computed tomography) scans after administering intravenous contrast agents, are commonly used to aid the surgeons. However, due to the dynamic geometry of tumor tissue as well as normal brain during surgery, none of these pre-imaging technologies enables reliable intraoperative guidance for brain tumor resection

surgery. Another approach to aid the visualization of the tumors during the surgical procedure employs dyes to demarcate the tumor boundaries. Several visual and fluorescent dyes such as Coomassie Blue, Bromophenol Blue, Indocyanine Green, fluorescent porphyrins and fluorescein have been used for this purpose [2–9]. However, there are negative side effects generated by the systemic injection of the dye, especially when the concentration of the dye needs to be high enough for visualization by eye. Furthermore, in order to visualize fluorescent dyes, special illumination and a dark background are essential, but these are likely to interfere with the surgical procedure. Therefore, keeping the dye concentration as low as possible, while still providing sufficient contrast for differentiating tumors from background tissue, is still a major challenge. Moreover, based on the direct visualization of the dyes, during the surgical procedure the surgeon can only evaluate the surface of the brain but has no access to three-dimensional (3D) morphological tissue information including the depth and extension of the tumor in subsurface brain.

Photoacoustic imaging (PAI), as an emerging hybrid imaging modality that combines the merits of both light and ultrasound, may provide an alternative approach for mapping the optical contrast agents in the brain and for guiding the surgical resection of tumors. In PAI, a short-pulsed laser source is used to illuminate the tissue sample, and the photoacoustic waves excited by thermoelastic expansion due to light absorption are then measured to reconstruct the optical absorbers distribution in the sample. Therefore, while a PAI image presents the optical contrast in the biological tissues, its resolution is primarily limited by the bandwidth of the detected photoacoustic waves [10]. Because ultrasonic waves are much less scattered in biological tissues than are optical waves, PAI can depict subsurface tissue structures much more accurately than

optical imaging. Like conventional optical imaging technologies, PAI presents high sensitivity in imaging versatile contrast agents. However, unlike fluorescent imaging, PAI does not require a dark background, which is especially favorable for intraoperative tumor delineation during a surgical operation that has to be carried out under abundant lighting conditions. Employing laser-based PAI, imaging of the dynamic distributions of Indocyanine Green (ICG) in the circulatory system in small animal brains has been achieved in vivo [11]. More recently, noninvasive mapping of sentinel lymph nodes and lymphatic vessels in rats in vivo has been realized using PAI enhanced by ICG contrast agent [12]. These studies have demonstrated the high sensitivity, good spatial resolution and satisfactory imaging depth of PAI in localizing and quantifying optical contrast agents in living tissues [13–15].

Reported in this article is an exploratory study on tumor delineation by PAI that is aided by tumor-targeting blue nanoparticles (NPs) as an optical contrast agent. The hydrogel NPs are made of an inert polyacrylamide (PAA) matrix with covalently linked Coomassie Blue (CB) dye molecules, and their surfaces are conjugated with F3 peptides for active tumor targeting. The PAA nanoparticles are biocompatible, chemically inert, with a long plasma circulation lifetime and nontoxic, which makes them suitable as nanodevices for efficient imaging of tumors [16, 17]. Compared to the free Coomassie Blue dye, the nanoparticles can be selectively targeted to specific tumors or tumor vasculature. They have the ability to act as a platform for delivering contrast agents and drugs into tumors in vivo [18, 19]. Previously, our lab has used Coomassie Blue (CB)-containing nanoparticles to delineate brain tumors visually [20]. We use blue nanoparticles, as blue offers the best contrast with the red (blood) background, and is most suitable for visual delineation. In this work, we investigated the possibility of imaging and

delineating tumors based on PAI, while using the same CB nanoparticles as the PAI contrast enhancement agent. We focused especially on the use of PAI for tumors treated with a very low dose of nanoparticles and, hence, not differentiable by eye. The method presented here can be used as a complement to visual delineation, especially in areas or at levels indistinguishable by eye.

Highly sensitive imaging of the nanoparticles in the tumor was possible using a home-made PAI system. We used reconstruction-based PAI for our imaging purpose. Compared to the reflection model, reconstruction-based PAI using an array of transducers for reconstruction-based PAI enables real time imaging. Also, for a reconstruction-based PAI system, the image quality, including resolution and pixel number is not limited by the number of transducers but instead by the bandwidth and receiving angle of the transducer, making it more economical and affordable. We first explored the sensitivity of this system by imaging nanoparticles in phantoms. The lowest concentration that was detectable by the PAI was about 0.01 mg/mL. At this concentration, the nanoparticle-containing inclusions in the phantoms cannot be differentiated from the background by the naked eye. Following the experiments on phantoms, the PAI setup was used to image ex vivo rat brains containing tumors that had been treated with various doses of nanoparticles. The high sensitivity of the PAI enabled a successful delineation of tumors that did not show any color contrast, compared to the background brain tissues, when observed by the eye. This exploratory study suggests that PAI, enhanced by tumor-targeting nanoparticle contrast agents for delineating tumors, has the potential for reliable preoperative or intraoperative guidance of surgical resection of glioma.

Experimental

Chemicals and materials

Acrylamide, methylene-bis-acrylamide (MBA), dioctylsulfosuccinate (AOT), Brij 30, hexane, ammonium persulfate (APS), *N*,*N*,*N*′,*N*′-tetramethylethylenediamine (TEMED), *N*-(3-dimethylaminopropyl)- *N*′-ethylcarbodiimide hydrochloride (EDC), bovine serum albumin (BSA) (30% w/v), *L*-cysteine, Coomassie Blue derivative(CB), *N*,*N*-dimethylformamide (DMF) and glycerol dimethacrylate (GDMA) were all acquired from Sigma-Aldrich (St. Louis, MO). 3-(aminopropyl)methacrylamide hydrochloride salt (APMA) was obtained from Polysciences Inc. (Warrington, PA). Ethanol (95%) was acquired from Decon labs, Inc (King of Prussia, PA). *N*-hydroxysulfosuccinimide (sulfo-NHS) and succinimidyl 4-[*N*-maleimidomethyl]cyclohexane-1-carboxylate (SMCC) were acquired from Pierce Biotechnology (Rockford, IL). F3-Cys peptide (PKAARALPSQRSRPPEKAKKPPDKPAPEKKKC) was purchased from SynBioSci (Livermore, CA). All solutions were prepared in 18-MΩ water purified in a Barnstead 1 Thermolyne NANOpure II system. All chemicals and materials were used as received.

Photoacoustic setup

A schematic illustration of the experimental setup is shown in Fig. 1. A tunable dye laser (ND6000, Continuum) pumped by the second harmonic of a pulsed Nd:YAG laser (Powerlite, Continuum) was employed to provide pulsed light with a pulse width of 5 ns, a tuning range of 578–610 nm using R610 dye, and a pulse energy of 90 mJ at a wavelength of 590 nm (the optical absorption peak of the nanoparticles). After being expanded and homogenized, the laser beam covered an area of about 30 cm^2 on the surface of the sample with an incident energy density of

3 mJ/cm^2, well below the American National Standard Institute (ANSI) safety limit of 20 mJ/cm^2.

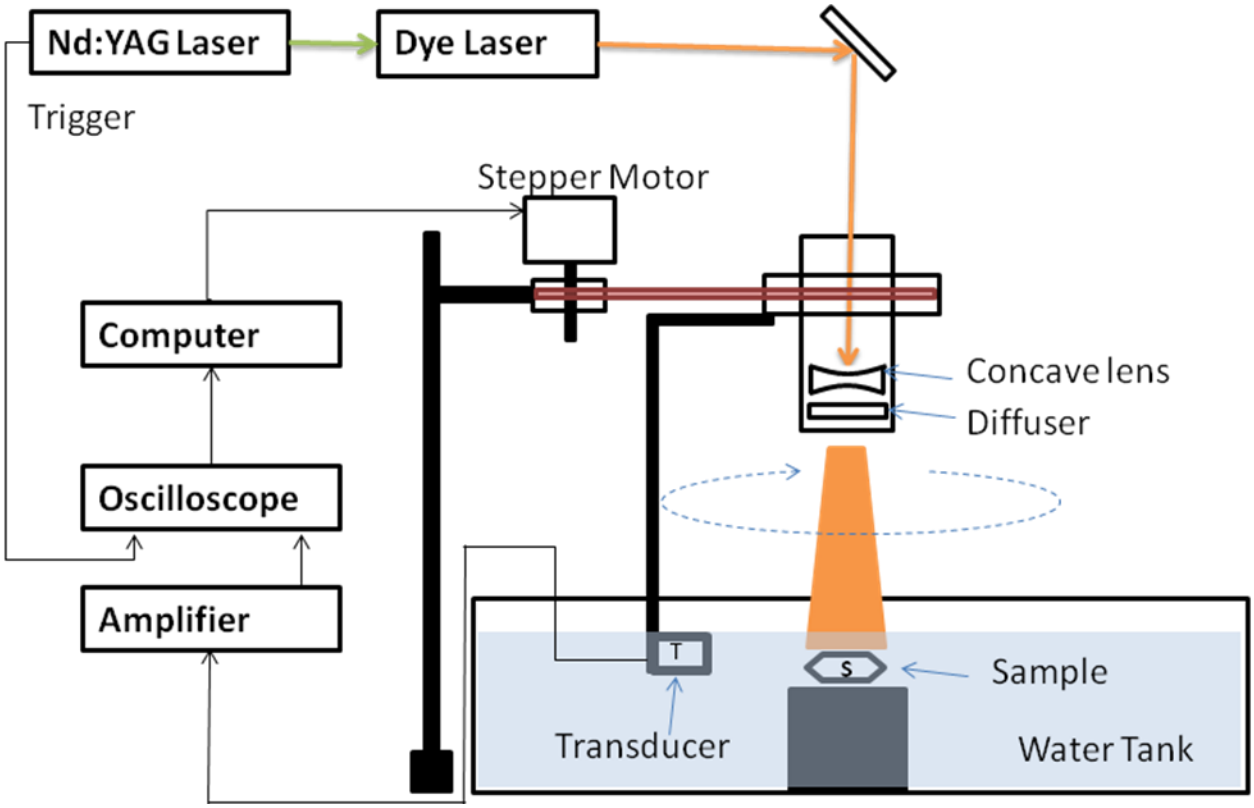

Figure 1 Schematic illustration of the PAI setup.

The ultrasound signal created due to the laser induced thermo-elastic expansion was detected by a high-sensitivity, wide-bandwidth (132.63% at –6 dB with a center frequency of 9.01 MHz) ultrasonic transducer (V312, Panametrics) that was cylindrically focused with a focal length of 0.75 inch. Using the transducer with a cylindrical focusing, resolution along the Z-axis was 0.46 mm. The signal from the transducer was amplified and then digitized by an oscilloscope. Driven by a computer controlled stepper motor, the transducer scanned circularly around the sample

with a step size of 3 degrees and a number of steps of 120 (i.e. 360 degrees of total view angle). The images were collected very close to the surface of the tumors. With all the data collected, a two-dimensional (2D) cross sectional image of the sample was built using a modified back-projection algorithm [21, 22]. For this prototype study we used a single transducer. However an ultimate clinical device would probably involve a transducer array, possibly ring shaped.

Preparation of nanoparticles

The nanoparticle contrast agents for PAI were prepared by a reverse nanoemulsion polymerization method as shown in Fig.2 [16]. The monomer solution was prepared using 8.6 mmol of acrylamide and 0.25 mmol of 3- (aminopropyl)methacrylamide hydrochloride salt (APMA) dissolved in 1.0 mL of water. The dye solution was prepared by dissolving 0.12 mmol of CB-derivatized acrylamide in 400 μL of DMF and then 360 μL of glycerol dimethacrylate (GDMA) were added. This monomer solution and the dye solution were combined and sonicated before adding them to 120 mL of a hexane solution containing 28.5 mmol Brij-30 and 8.77 mmol dioctylsulfosuccinate. The two solutions were emulsified by stirring them for 20 min under an inert atmosphere. The reaction was initiated by using 150 μL of *N*,*N*,*N*′,*N*′-tetramethylethylenediamine (TEMED) and 240 μL of ammonium persulfate (APS). The APS was freshly prepared by dissolving it in water 50% (W/V). The solution was further stirred for two hours under an inert atmosphere, to complete the polymerization. The hexane was removed by rotary evaporation, using a Rotavapor-R (Brinkmann Instruments) and then ethanol was added to the residue. The surfactants and excess dye were removed by washing the particles several times with ethanol and then with water in an Amicon ultra-filtration cell (Millipore Corp., Bedford, MA) using a 300 kDa filter and then freeze-dried with a 5L ModulyoD freeze

dryer (Thermo Fisher Scientific). Thus prepared CB-containing PAA nanoparticles were surface-conjugated with F3 peptide so as to enhance tumor selective staining. The F3 peptide is a 31-amino acid fragment of HMNG-2 (human high-mobility group-2) protein and is known for its tumor homing capability towards neucleolin-over-expressing tumor and tumoric endothelial cells [23–25]. Affinity towards tumor cell lines has been previously investigated in our lab [26, 27]. The freeze-dried PAA nanoparticles (50 mg) were dissolved in pH 7.4 phosphate buffered saline (PBS) (2.5 mL), treated with PEG–SMCC (2 µmol) and stirred at room temperature for 30 min. The reaction mixture was then subjected to thorough washing to remove any unreacted ligands and concentrated to ~20 mg/mL. F3-Cys peptides (0.06 µmol) was added to the concentrated nanoparticle solution which was gently stirred overnight (>8 hours) at room temperature and treated with *L*-cysteine (1 µmol) for another 2 hours. The resultant solution was thoroughly washed with water and PBS in an Amicon cell and then freeze dried.

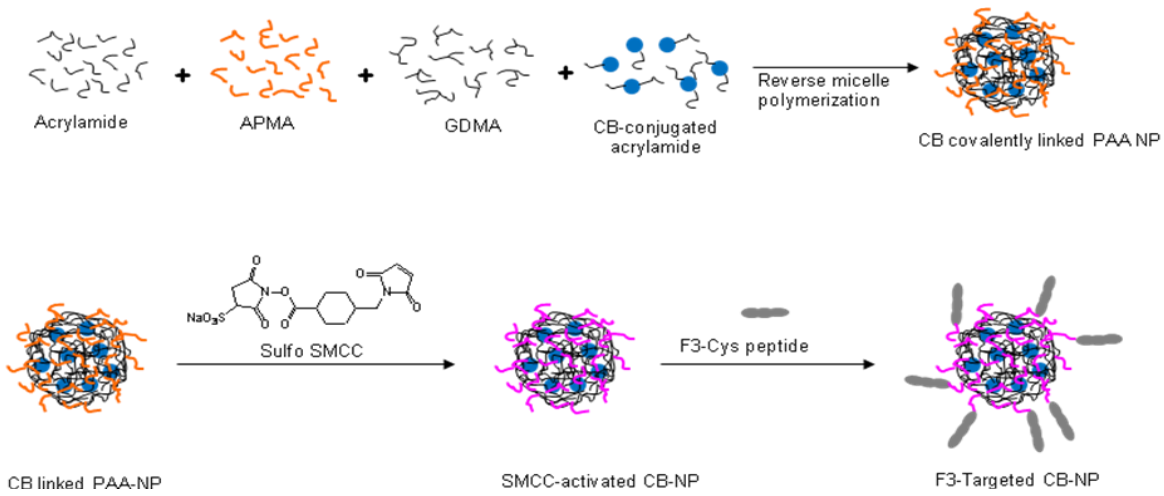

Figure 2 Synthesis of targeted Coomassie Blue-loaded nanoparticles, through a reverse nano-emulsion polymerization process followed by the attachment of the tumor-homing F3 peptide.

Results and discussion

Nanoparticle characterization

The size of the nanoparticles in dried powder form was measured by scanning electron microscopy (SEM) while the size distribution of the nanoparticles in aqueous solution was obtained by dynamic light scattering (DLS) using a Beckman Coulter DelsaNano C zeta potential/submicrometer size analyzer. The particle size of the dried form was approximately between 15–40 nm and the average particle size in aqueous solution was 80 nm (Figs. 3a and 3b). The CB dye loading per nanoparticle was determined by comparing the optical absorbance of the nanoparticle suspension of a known concentration with those of free CB dye at different known concentrations. The measured CB contents per nanoparticles thus obtained were about 7.0% by weight. The prepared nanoparticles are highly suspendable in water and PBS (>50 mg/mL). The nanoparticles had a maximum absorption of around 590 nm as shown in Fig. 3c.

Moreover, these nanoparticles are quite stable and the nanoparticle suspension in PBS showed no change in spectral characteristics and no precipitate formation after storing in the refrigerator for 6 months. No dye leaching out of the nanoparticles was observed after incubation for 72 hours in 9% albumin containing PBS at 37 °C.

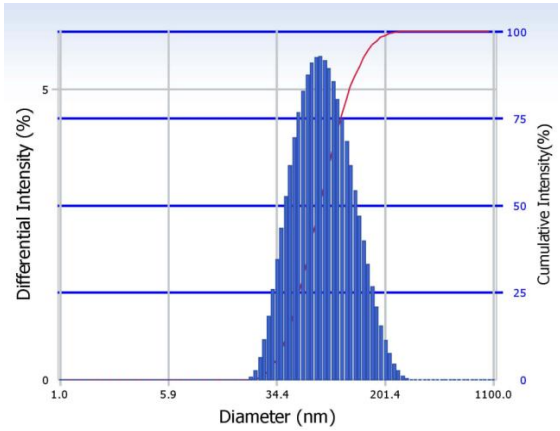

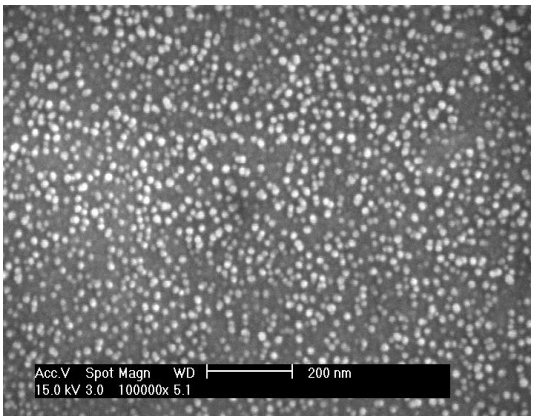

(a) (b)

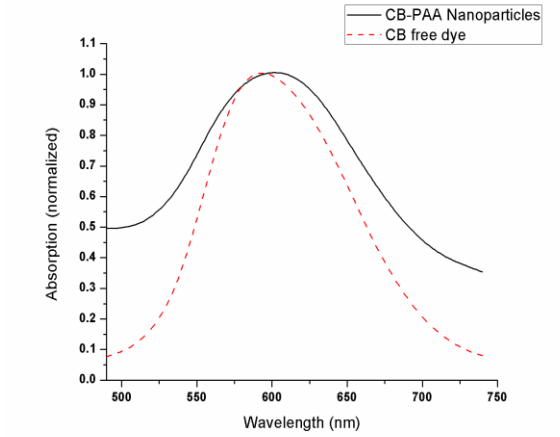

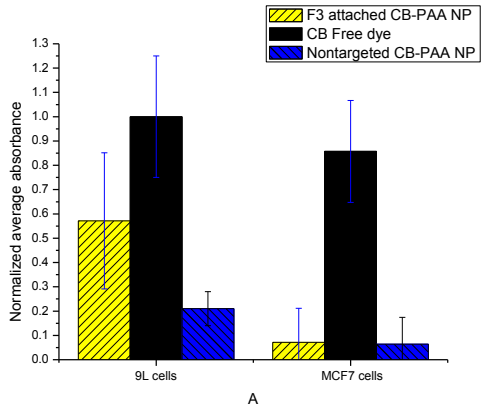

(c) (d)

Figure 3 Characterization of the Coomassie Blue-attached nanoparticles. (a) The size distribution of the nanoparticles in aqueous medium, as obtained from the DLS reading. (b) SEM image of the nanoparticles, (c) Normalized extinction (absorption + scattering) spectrum of the nanoparticles and the free dye. The nanoparticle spectral curve does not go to the baseline due to significantly higher scattering, compared to the free dye. (d) The 9L glioma cell and MCF7 cell targeting efficiency of the F3-attached nanoparticles. The dye stains the cells, irrespective of the cell line, due to its high affinity towards the proteins. However the F3-targeted nanoparticles stain the 9L cells significantly more than the MCF7 cells. Note that the non-targeted nanoparticles stain the targeted cells (9L) significantly less, while for the non-targeted cells (MCF7) both targeted and non-targeted particle staining is equally poor, as expected.

We compared the staining efficiency of the F3-targeted nanoparticles with the non-targeted nanoparticles in vitro. 9L cells (glioma) and MCF7 cells (breast cancer) were incubated with both F3-targeted and non-targeted CB nanoparticles in separate wells in a six-well plate. After incubation for 30 minutes, the cells were washed thoroughly and their absorbance at 620 nm was observed using a plate reader. We saw a significant amount of staining of the 9L cells that were incubated with the F3-targeted nanoparticles, as compared to the non-targeted ones (Fig. 3d). The 9L cells incubated with non-targeted nanoparticles did not show significant staining. The MCF7 cells showed little staining with either the F3-targeted or non-targeted nanoparticles (Fig. 3d). While cells incubated with free CB dye also stained well, there was no specific/selective staining towards any cell line such as 9L vs. MCF7 (Fig. 3d). The reason for the high staining is attributed to the high affinity of this dye towards any protein. Thus this in vitro experiment clearly demonstrates the advantage of using specifically targeted nanoparticles, compared to free dye, for selective and efficient staining of gliomas.

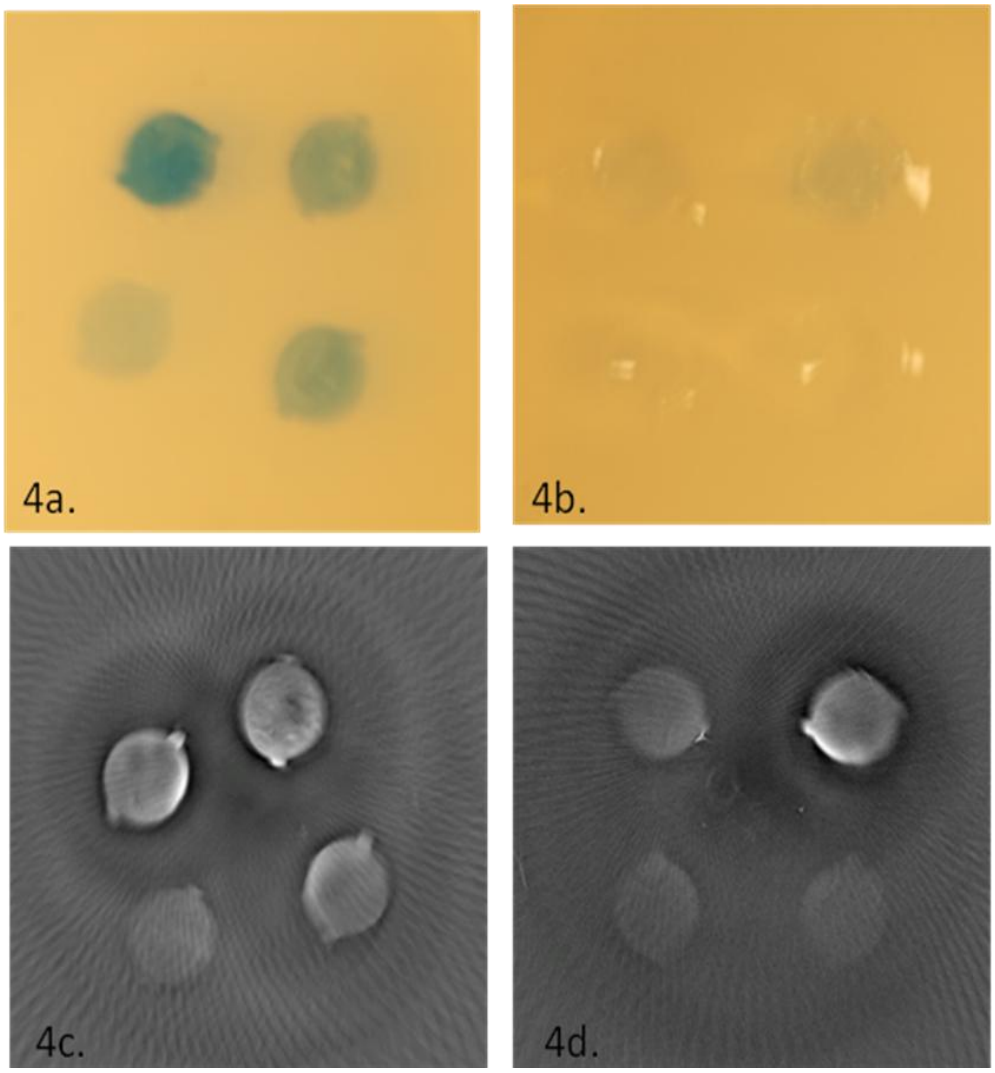

Figure 4 (a) and (b): Photographs of phantoms #1 (concentration of nanoparticle (clockwise): 0.5 mg/mL, 0.25 mg/mL, 0.2 mg/mL and 0.125 mg/mL) and #2 (concentration of nanoparticles (anti-clockwise): 0.1 mg/mL, 0.04 mg/mL, 0.02 mg/mL and 0.01 mg/mL) , respectively. (c) and (d): PAI images of the phantoms #1 and #2, respectively (taken with an amplifier gain of 35 db and 45 db, respectively) (scale 3 cm x 3 cm).

Phantom imaging

In order to examine the detection limit of our nanoparticle contrast agent by the PAI system, gel phantoms with inclusions containing different concentrations of the nanoparticle contrast agent were imaged. Two phantoms (#1 and #2) were made by boiling 2.5 g of agarose in 100 mL of water, with each having four cylindrical inclusions, as shown by their photographs in Figs. 4a and 4b, respectively. In phantom #1, the concentrations of the nanoparticles in the four inclusions were 0.5 mg/mL, 0.25 mg/mL, 0.2 mg/mL and 0.125 mg/mL. At these concentrations, the four inclusions can be easily recognized in the sample photograph. In phantom #2, the concentrations of the nanoparticles in the four inclusions were 0.1 mg/mL, 0.04 mg/mL, 0.02 mg/mL and 0.01 mg/mL. By observing the phantom by naked eye, the inclusions with concentrations of 0.1 mg/mL and 0.04 mg/mL are just barely distinguishable; however, the inclusions with concentrations of 0.02 mg/mL and 0.01 mg/mL are not distinguishable from the background. The imaging of the phantoms with higher concentration of nanoparticles (Fig. 4a) was performed at a slightly lower amplifier gain (35 db), compared to the one with low concentration of nanoparticles (Fig. 4b), due to signal saturation of the signal over 35 db. The rest of the measurements were taken at 45 db. The PAI images of the two phantoms are shown in Figs. 4c and 4d, respectively. All the inclusions in the two phantoms can be recognized clearly, including the two most diluted inclusions that cannot be differentiated from the background by the naked eye. We have imaged additional phantoms with inclusions containing even further diluted concentrations of nanoparticle contrast agent. When the concentration was 0.005 mg/mL or lower, the contrast-to-noise ratio in imaging the inclusions was less than 1, i.e. the inclusions could not be recognized in the image any more. Using our current PAI system, the maximum

sensitivity in visualizing the nanoparticle contrast agent is on the order of 0.01 mg/mL, which is equivalent to 0.7 μg/mL or 0.84 μM CB dye at an incident energy density of 3 mJ/cm^2. We obtained signal-to-noise (S/N) ratios of 11, 11, 9 and 5, respectively, for each inclusion in the phantom with high concentration of nanoparticles (Fig. 4c). For the phantom with low concentration nanoparticle inclusions, we obtained fairly high S/N ratios of 11, 5, 3, 2, respectively, for each of the inclusions (Fig. 4d).

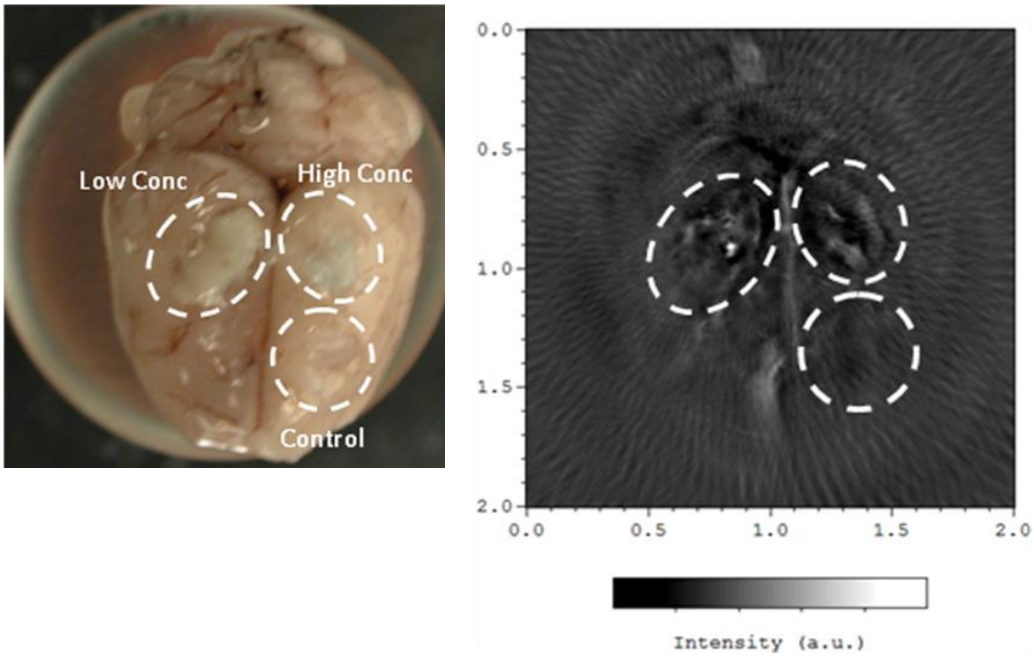

(a) (b)

Figure 5 (a) Photograph of a rat brain with three embedded tumors. (b) PAI image of the brain (scale 2 cm x 2 cm).

***Ex vivo* imaging**

The in vivo feasibility tests were performed on a rat brain tumor window (BTW) model—a rat with a cranial glass window and a 9L glioma implanted tumor, for visual observation of the rat brain. The BTWs were installed in Sprague Dawley rats weighing 250 to 350 g. The tumor model used was an orthotopic model, i.e., gliomas were grown in the rat brain by implanting the 9L cells about 2 mm deep into the inner table of the skull and then subsequently closing the skin, as reported before [2]. Implantation of the tumor in the rats was part of a separate study that aims to establish visual tumor delineation. The nanoparticle contrast agents conjugated with the tumor-targeting F3 peptide were administered intravenously into the right femoral vein of live Sprague Dawley rats with developed brain tumors, as described previously [2, 20]. The animals were sacrificed by CO_2 asphyxiation, 6–10 days after nanoparticle administration. At the conclusion of each delineation experiment, the brain and intact tumor were removed from the skull of the rat. Gross brains and tumors were embedded in Tissue-Tek Optimal Cutting Temperature compound (Sakura Finetek, Zoeterwoude, Netherlands) before being frozen at –80 ^{o}C for preservation. Previously, tissue distribution studies (liver, kidney, lungs, heart, spleen, brain and the bone marrow) have been performed by our group after a *single* intravenous *bolus injection* of ^{14}C labeled non-targeted and PEGylated nanoparticles into the tail veins of healthy male rats [28]. It was found that the liver was the major site of deposition among the organs, while the lungs and kidneys were secondary sites of deposition, for both formulations. In term of concentrations, the majority of the organs contained levels of radiolabel that were roughly comparable, with the exception of the brain in which an approximate 10-fold reduction was observed [28]. Our other previous studies showed that, in the case of tumor-bearing rats, the

nanoparticles can be efficiently delivered intravascularly to the brain tumor site [18]. Moreover, the same studies revealed that the presence of the F3-targeting moiety results in a significantly greater amount of nanoparticle accumulation and longer duration within the tumor, leading to significant enhancement in image contrast and therapeutic efficacy of the nanoparticles [18]. Our previously published MRI images of rat brain tumors [18] show that non-targeted PAA nanoparticles are not retained inside the tumors beyond two hours after IV injection, whereas the F3-targeted PAA nanoparticles show significant retention several days later. In the recent delineation protocols [20] and those reported here, we waited several days post-injection before sacrificing the animals. Given this significantly long time, the retention of non-targeted nanoparticles inside the tumors would be negligible. Therefore, we did not study a control group with non-targeted nanoparticles for the in vivo visual delineation protocol [20], nor in this current ex vivo photoacoustic delineation protocol, but limited ourselves to studying controls with no nanoparticles. In the first study, three tumors, were embedded at different locations in an excised rat brain specimen and then imaged simultaneously, as shown in Fig. 5(a). The three tumors were harvested from three different rats: two of them were injected with different dose of nanoparticles (250 mg/Kg of rat weight and 125 mg/Kg of rat weight) and the third rat was not injected with the nanoparticle and thus was used as control. The tumor, extracted from the rat injected with a dose of 250 mg/Kg of rat weight, containing a higher dose of nanoparticles, was slightly bluish. It could be differentiated from the background upon close visual inspection; however, the other tumor, containing the lower dose of nanoparticles, did not show a distinct color and could not be differentiated from the background brain tissue by the naked eye. A PAI image of the three tumors embedded on the brain is shown in Fig. 5b. We can clearly distinguish the two tumors that were treated with the nanoparticle contrast agent, including the one that is

not distinguishable by eye. In comparison with the two nanoparticle-containing tumors, the control tumor that was extracted from a rat not injected with any nanoparticle, did not show any enhanced signal.

In another experiment, we imaged quite a few individual tumors, each in their original brain specimen. Figure 6a shows a sample photograph of a rat brain containing a tumor containing a low dose of nanoparticles (125 mg/Kg of rat weight). At this dose, the color contrast between the tumor and background brain tissue is not sufficient to differentiate the tumor by the eye. However, as shown in Fig. 6b, the tumor can be clearly recognized in the PAI image, facilitated by the superior sensitivity of PAI in imaging the nanoparticle contrast agent. We have also observed strong signals from some specific areas of the tumor, which is likely due to the higher local density of the nanoparticles in those areas, as a result of inhomogeneous uptake of the contrast agent by the tumor tissue. For comparison with Fig. 6b, Fig. 6c shows the image of a tumor in another specimen that does not contain any nanoparticles. The intrinsic contrast of the tumor is quite similar to that of the rest of the brain. Thus the outline of the brain tumor is barely visible from the background, which is in stark contrast to the photoacoustic images of the tumors targeted with the blue nanoparticles. We found an average S/N ratio of around 2.0 for the photoacoustic images of the tumor. The current method can also be used to quantify the size of the tumors. We performed 2D imaging and so, in our measurements, we were able to estimate the cross section of the rat brain tumors with an accuracy of ±1 mm. However we expect that any 3D PAI will enable us to estimate the complete tumor size with similar accuracy (±1 mm).

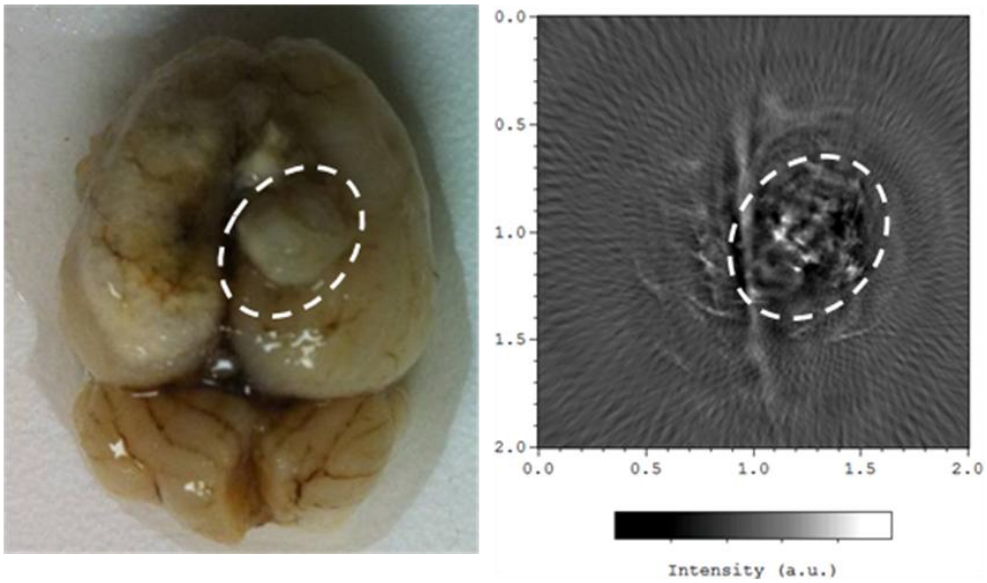

(a) **(b)**

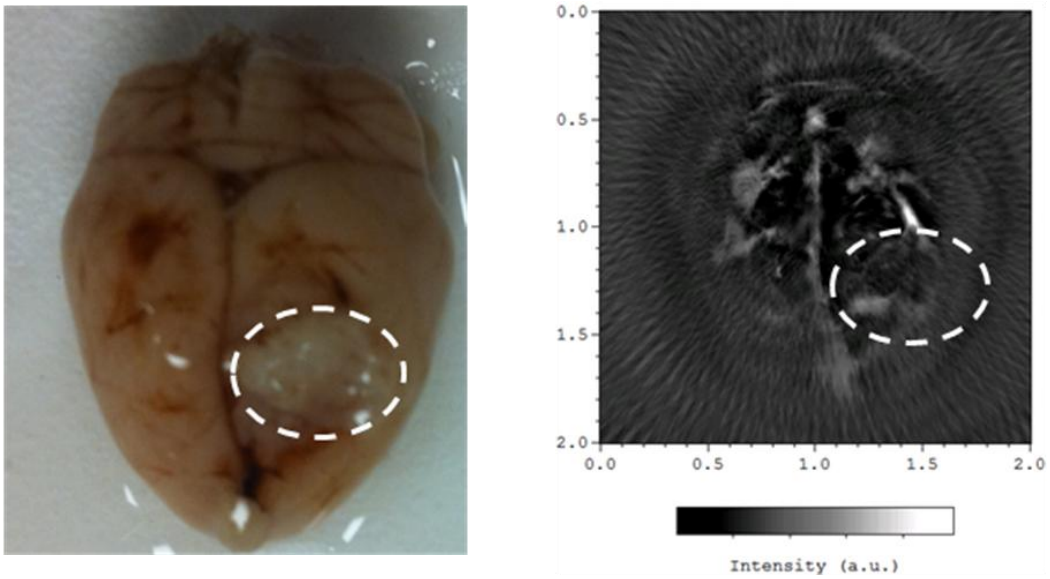

(b) **(d)**

Figure 6 (a) Photograph of a rat brain containing a tumor treated with nanoparticles. (b) PAI image of the sample (scale 2 cm x 2 cm). (c) Photograph of the control tumor in the brain containing no contrast agent. (d). PAI image of the sample (scale 2 cm x 2 cm). We do not see any signal from the control tumor.

This study was performed to show a proof of principle for our blue nanoparticle-aided PAI for the purpose of tumor delineation and thus only eight tumors (two containing a high dose of nanoparticles, three containing low dose of nanoparticles, and three control tumors with no nanoparticles) were imaged, and all the images were taken ex vivo. We did not see any enhanced PA signal from the three control tumors, whereas all the five tumors that had been targeted with the nanoparticles at both high and low concentrations showed a significantly increased PA signal. We believe that this preliminary study on ex vivo animal models has demonstrated the potential of PAI in delineating brain tumors targeted with our blue nanoparticles.

Also with a maximum absorption at 590 nm, the blue nanoparticles show a strong optical contrast with respect to the background tissue and hence can be clearly visualized by eye. For this reason, using the blue nanoparticles to delineate the tumor boundary will be highly advantageous to surgeons. The aim of this study is to develop a complementary technique to current visual tumor delineation, presenting tumor locations with better accuracy whenever the visual contrast is not sufficient. Therefore, using the same contrast agent for both PAI and visual delineation is the best strategy and is what we examined in this study. However, contrast agents working in the visible region of the optical spectrum are not the most suitable for in vivo PAI due to the strong intrinsic absorption from the blood. In comparison, near-infrared region contrast agents with absorption from 700 nm to 950 nm should be a better choice considering the weak absorption of blood and, as a result, the low background signals from the brain. In the future, nanoparticle contrast agents with broader absorption spectra or dual absorption peaks, one around 590 nm while the other in the near-infrared spectral region, could provide better solutions.

Conclusion

We have demonstrated the feasibility of imaging brain tumors by using PAI aided by tumor-targeting blue PAA nanoparticles as a contrast agent. These nanoparticles provide excellent contrast enhancement when imaged by our PAI system. Facilitated by the intrinsically high sensitivity of PAI, brain tumors containing contrast agent with concentrations that are too low to be visualized by the naked eye could still be recognized clearly in the PAI images. Benefiting from both high sensitivity and excellent spatial resolution, PAI could contribute to future surgical procedures on gliomas by aiding the surgeons in delineating the tumors in the brain, without the need for the high dose of contrast agent that is necessary for visual delineation. We note that reducing the dose of administered nanoparticles by a factor of four or more would have high clinical significance. Although the performance of PAI in imaging the brain tumor was only validated through 2D imaging experiments in this study, PAI allows high resolution 3D imaging and good penetration depth up to several centimeters in strongly optically scattering tissues [10]. We thus expect PAI to also be useful for delineating the 3D distribution and morphological shape of tumors in the brain. Moreover, since the nanoparticle contrast agents are biocompatible, chemically inert and have a long circulation lifetime, they could also be designed to target other specific cell membrane receptors found in various types of cancer cells, such as prostate and bladder cancers, and thus could act as a demarcation agent for other cancerous tumors.

Acknowledgements

This work was supported by NIH grant R33CA125297 (RK) and NSFC grant 11028408 (XW). We thank Dr. Z. Xie and Dr. J. Rajian for their help during photoacoustic imaging. We also like to extend our sincere thanks to Dr. M. Nie for his help during nanoparticle synthesis. We would also like to thank Dr. Oren Sagher, Dr. Daniel Orringer and Mr. Dah-Luen Huang for development of the BTW model.

References

1. Sanai, N.; Berger, M. S. Glioma extent of resection and its impact on patient outcome. *Neurosurgery*, **2008**, *62*, 753–766.

2. Orringer, D. A.; Chen, T.; Huang, D. L.; Armstead, W. M.; Hoff, B. A.; Koo, Y. E.; Keep, R. F.; Philbert, M. A.; Kopelman, R.; Sagher, O. The brain tumor window model: A combined cranial window and implanted glioma model for evaluating intraoperative contrast agents. *Neurosurgery* **2010**, *66*, 736–743.

3 Ozawa, T.; Britz, G. W.; Kinder, D. H.; Spence, A. M.; VandenBerg, S.; Lamborn, K. R.; Deen, D. F.; Berger, M. S. Bromophenol blue staining of tumors in a rat glioma model. *Neurosurgery*, **2005**, *57*, 1041–1047.

4. Britz, G.; Ghatan, S.; Spence, A.M.; Berger, M. S. Intracarotid RMP-7 enhanced indocyanine green staining of tumors in a rat glioma model. *J. Neurooncol*. **2002**, *56*, 227–232.

5. Hansen, D. A.; Spence, A. M.; Carski, T.; Berger, M. S. Indocyanine green (ICG) staining and demarcation of tumor margins in a rat glioma model. *Surg. Neurol*. **1993**, *40*, 451–456.

6. Shinoda, J.; Yano, H.; Yoshimura, S.; Okumura, A.; Kaku, Y.; Iwama, T.; Sakai, N. Fluorescence-guided resection of glioblastoma multiforme by using high-dose fluorescein sodium. *J. Neurosurg*. **2003**, *99*, 597–603.

7. Stummer, W.; Pichlmeier, U.; Meinel, T.; Wiestler, O. D.; Zanella, F.; Reulen, H. J. Fluorescence-guided surgery with 5-aminolevulinic acid for resection of malignant glioma: A randomised controlled multicentre phase III trial. *Lancet Oncol*. **2006**, *7*, 392–401.

8. Moore, G. E. Fluorescein as an agent in the differentiation of normal and malignant tissues. *Science* **1947**, *106*, 130–131.

9. Veiseh, M.; Gabikian, P.; Bahrami, S. B.; Veiseh, O.; Zhang, M.; Hackman, R. C.; Ravanpay A. C.; Stroud, M. R; Kusuma, Y.; Hansen, S. J.; Kwok, D.; Munoz, N. M.; Sze, R. W.; Grady W. M.; Greenberg, N. M.; Ellenbogen, R. G.; Olson, J. M. Tumor paint: A chlorotoxin:Cy5.5 bioconjugate for intraoperative visualization of cancer foci. *Cancer Res.* **2007**, *67*, 6882–6888.

10. Xu, M.; Wang, L. H. Time-domain reconstruction for thermoacoustic tomography in a spherical geometry. *IEEE T. Med. Imaging* **2002**, *21*, 814–822.

11. Wang, X.; Ku, G.;,Wegiel, M. A.; Bornhop, D. J.; Stoica, G.; Wang, L. V. Noninvasive photoacoustic angiography of animal brains in vivo with near-infrared light and an optical contrast agent. *Opt. Lett.* **2004**, *29*, 730–732.

12. Kim, C.; Song, K. H.; Gao, F.; Wang, L. V. Sentinel lymph nodes and lymphatic vessels: Noninvasive dual-modality in vivo mapping by using indocyanine green in rats—volumetric spectroscopic photoacoustic imaging and planar fluorescence imaging. *Radiology* **2010**, *255*, 442–450.

13. Kim, C.; Cho, E.; Chen, J.; Song, K. H.; Au, L.; Favazza, C.; Zhang, Q.; Cobley, C. M.; Gao, F.; Xia, Y.; Wang, L. V. In vivo molecular photoacoustic tomography of melanomas targeted by bioconjugated gold nanocages. *ACS Nano* **2010**, *4*, 4559–4564.

14. De la Zerda, A.; Zavaleta, C.; Keren, S.; Vaithilingam, S.; Bodapati, S.; Liu, Z.; Levi, J.; Smith, B. R.; Ma, T.; Oralkan, O.; Cheng, Z.; Chen, X.; Dai, H.; Khuri-Yakub, B. T.; Gambhir, S. S. Carbon nanotubes as photoacoustic molecular imaging agents in living mice. *Nat. Nanotechnol.* **2008**, *3*, 557–562.

15. Li, P.; Wang, C.; Shieh, D.; Wei, C.; Liao, C.; Poe, C.; Jhan, S.; Ding, A.; Wu, Y. In vivo photoacoustic molecular imaging with simultaneous multiple selective targeting using antibody-conjugated gold nanorods. *Opt. Express* **2008**, *16*, 18605–18615.

16. Koo Lee, Y. E.; Smith, R.; Kopelman, R. Nanoparticle PEBBLE sensors in live cells and in vivo. *Annu. Rev. Anal. Chem.* **2009**, *2*, 57–76.

17. Orringer, D. A.; Koo, Y. E.; Chen, T.; Kopelman, R.; Sagher, O.; Philbert, M. A. Small solutions for big problems: The application of nanoparticles to brain tumor diagnosis and therapy. *Clin. Pharmacol. Ther.* **2009**, *85*, 531–534 .

18. Reddy, G. R.; Bhojani, M. S.; McConville, P.; Moody, J.; Moffat, B. A.; Hall, D. E.; Kim, G.; Koo, Y. E.; Woolliscroft, M. J.; Sugai, J. V.; Johnson, T. D.; Philbert, M. A.; Kopelman, R.; Rehemtulla, A.; Ross, B. D. Vascular targeted nanoparticles for imaging and treatment of brain tumors. *Clin. Cancer Res.* **2006**, *12*, 6677–6686.

19. Winer, I.; Wang, S.; Koo Lee, Y. E.; Fan, W.; Gong, Y.; Burgos-Ojeda, D.; Spahlinger, G.; Kopelman, R.; Buckanovich, R. J. F3-Targeted cisplatin–hydrogel nanoparticles as an effective therapeutic that targets both murine and human ovarian tumor endothelial cells in vivo. *Cancer Res.* **2010**, *70*, 8674–8683.

20. Orringer, D. A.; Sagher, O.; Kopelman, R.; Koo, Y. E. Dye loaded nanoparticle. US Patent 20100098637, April 22, 2010.

21. Xu, M.; Wang, L. V. Universal back-projection algorithm for photoacoustic-computed tomography. *Phys. Rev. E* **2005**, *71*, 016706.

22. Wang, X.; Pang, Y.; Ku, G.; Xie, X.; Stoica, G.; Wang, L. V. Non-invasive laser-induced photoacoustic tomography for structural and functional imaging of the brain in vivo. *Nat. Biotechnol.* **2003**, *21*, 803–806.

23. Porkka, K.; Laakkonen, P.; Hoffman, J. A.; Bernasconi, M.; Ruoslahti, E. A fragment of the HMGN2 protein homes to the nuclei of tumor cells and tumor endothelial cells in vivo. *Proc. Natl. Acad. Sci. USA* **2002**, *99*, 7444–7449.

24. Akerman, E.; Chan, W. C.; Laakkonen, P.; Laakkonen, P.; Bhatia, S. N.; Ruoslahti, E. Nanocrystal targeting in vivo. *Proc. Natl. Acad. Sci. USA* **2002**, *99*, 12617–12621.

25. Ruoslahti, E.; Duza, T.; Zhang, L. Vascular homing peptides with cell-penetrating properties. *Curr. Pharm. Des.* **2005**, *11*, 3655–3660.

26. Orringer, D. A.; Koo Lee, Y. E.; Chen, T.; Kim, G.; Hah, H. J.; Xu, H.; Wang, S.; Keep, R.; Philbert, M. A.; Kopelman, R.; Sagher, O. In vitro characterization of a targeted, dye-loaded nanodevice for intraoperative tumor delineation. *Neurosurgery* **2009**, *64*, 965–972.

27. Lee Koo, Y. E.; Reddy, G. R.; Bhojani, M.; Schneider, R.; Philbert, M. A.; Rehemtulla, A.; Ross, B. D.; Kopelman, R. Brain cancer diagnosis and therapy with nano-platforms. *Adv. Drug Deliver. Rev.* **2006**, *58*, 1556–1577.

28. Wenger, Y.; Schneider II, R. J.; Ramachandra Reddy, R.; Kopelman, R.; Jolliet, O.; Philbert, M. A. Tissue distribution and pharmacokinetics of stable polyacrylamide nanoparticles following intravenous injection in the rat. *Toxicol. Appl. Pharmacol.* **2011**, *251*, 181–190.

Chapter 7

Summary and Future directions

Summary

Presented in this thesis is a combination of tumor-targeting, biocompatible, contrast enabling nanoprobes with optical imaging techniques, such as two photon fluorescence and photoacoustics (PA). These emerging optical imaging techniques, when combined with nanotechnology, provide a simple, low cost**,** non-ionizing and non-invasive method for monitoring chemical and morphological properties in biological systems. Recently, these optical techniques have drawn considerable attention and have been explored for their potential application to a variety of diseases, especially cancers, in pre-clinical settings. The feasibility of these techniques for chemical sensing and structural imaging were demonstrated on cancer cells and animal models.

In chapter 2 we presented a method of intracellular pH sensing, utilizing polyacrylamide (PAA) based nanoprobes to map out the pH in 9L rat gliosarcoma cells and HeLa cell spheroids, using two photon fluorescence microscopy. The pH sensitive nanoprobes were prepared by encapsulating a pH sensitive dye, HPTS into a hydrophilic PAA matrix. A special property of these nanoprobes is that their two photon fluorescence excitation of the nanoprobes changes with the pH of the external environment. Furthermore, their excitation at 900nm is extremely sensitive to the pH whereas the excitation at 752nm is nearly the same at all pH values. Thus the ratio of

the excitation at 900nm to 752nm was used to calculate the pH within the micro-environment of the nanoprobes with high precision. The pH sensitive nanoprobes were designed to specifically target the nucleolin receptors, over expressed on the surface of the rat gliosarcoma (9L) and melanoma (MDA-MB-435) cancer cell lines by using the F3 peptide. Our results therefore provide an insight into the pH distribution within single cells as well as for micro-tumors called spheroids. We also compared the distributions of targeted and non-targeted nanoprobes inside tumor cells and their co-localization with the acidic endosomes and lysosomes. [1]

In chapter 3 we introduced a new method of enhancing two photon fluorescence inside live cells. We successfully demonstrated two photon fluorescence enhancement using silver nanospheres and dye molecules, encapsulated inside the PAA nanoprobes. We incorporate 60nm or 10nm silver spheres inside the polymer matrix. At 900nm excitation we observed maximum fluorescence enhancement of 2.2 fold and 20 fold for the 10nm and 60nm silver cores respectively. We attribute this enhancement to the metal enhanced fluorescence effects that arise due to several phenomena, such as surface plasmon resonance, resonance energy transfer and second harmonic generation of the exciting light generated by the silver nanospheres. These nanoprobes were utilized for mapping the pH in endosomes of MDA-MB-435 cells.[2]

In chapter 4 we extended the application of the nanoprobes to *in vivo* studies. Although two photon fluorescence has a large optical penetration depth of several hundred's of microns, for the purpose of pH sensing *in vivo* we employed photoacoustics, which enables measurements at a larger penetration depth, in the order of millimeters. Here, we demonstrated the feasibility of *in vivo* pH quantification by nanoprobe-aided PAI using a rat-tail joint model. The nanoprobes employed in these experiments had hydrophobic cores loaded with the pH-sensitive dye,

SNARF. The photoacoustic signal from the nanoprobes are highly pH sensitive, when irradiated at 580 nm, but not so when irradiated at 565nm. Our results demonstrated that the properties of the free dye get severely altered in the presence of albumin; in comparison, the nanoprobes largely prevent the interaction of the encapsulated dyes with serum proteins that reside in the *in vivo* environment, thus preserving their optical properties and pH sensitivity *in vivo*. The *in vivo* experiments entailed injection of the pH sensitive nanoprobes (50mg/Kg of rat weight) into the tail joints of Sprague Dawley rats, after which the tail joint was sequentially irradiated at 580nm and 565nm, and the ratio of the resultant photoacoustic signals was used to determine the pH of the local environment, within 0.1 pH units.

In chapter 5, we demonstrate the feasibility of PAI in quantifying oxygen saturation, facilitated by an oxygen sensing probe. We used an oxygen sensing probe containing a porphyrin core and dendrimer covering, Pd-tetra-(4-carboxyphenyl) tetra-benzo-porphyrine-dendrimer (G2), for the *in-vivo* PAI application, using a lifetime based measurement technique. The probe has a ground state absorption maximum at 630 nm. Once the probe is excited to an intermediate triplet state, it has a relatively long lifetime (~250 micro-seconds) due to its relaxing to the ground state by a parity-forbidden transition mechanism. In the presence of oxygen, which is paramagnetic, this lifetime is shortened. We first excited the G2 with a pump beam at 630 nm and then used a probe beam at 950 nm to measure the transient absorption, in the excited triplet state. The photoacoustic signal intensities corresponding to the two beams were then recorded. The absorption of the probe beam in the excited triplet state depends on the phosphorescent lifetime and the delay between pump and probe beams. By changing the delay between the pump and probe beams, an exponentially decaying curve can be measured, from which the oxygen

concentration in the tissue can be elucidated. The *in vivo* experiments performed on Sprague Dawley rats entailed injection of a 0.9 mL dose of 5 mg/mL G2 solution (prepared in phosphate buffered saline) through a catheter inserted in the tail vein following which, the photoacoustic signals were measured from the main artery of the rat tail; while the global arterial oxygen saturation of the rat was adjusted to different levels by changing the percentage of oxygen in the breathing gas. As a gold standard to validate photoacoustic results, the local arterial oxygen saturation level in the rat tail was also monitored using a pulse-oxy meter. We observed a significant change in the decay curve corresponding to the change in oxygen saturation in the target blood vessel *in-vivo*. The lifetime of the G2 dye *in vivo,* quantified with PAI non-invasively, shows a good linear relationship with the blood oxygen saturation in the target vessel. Therefore, using a rat model, we successfully demonstrated the feasibility of using the G2 dye for *in vivo* quantitative evaluation of oxygen saturation with a sensitivity of 5 Torr. Although the feasibility of oxygen sensing using this technique was demonstrated in blood, this technique can also be applied to tissues devoid of blood, such as tumors, which is currently not possible with most of the established functional imaging techniques. [3]

The sixth chapter demonstrates the feasibility of nanoprobe-aided structural imaging of tumors. Experiments were performed *ex vivo* on rat brain samples embedded with 9L gliomas, within which Coomassie Blue nanoprobes were already sequestered. The blue-stained gliomas were produced, as a part of a separate study, with the aimof establishing visual tumor delineation [4]. Briefly, the nanoparticle contrast agents, bearing multiple surface conjugated tumor targeting F3 peptide, were administered intravenously into the right femoral vein of live Sprague Dawley rats with established brain tumors. Over time these nanoparticle contrast agents gets selectively

accumulated in the tumor and impart a bluish color to the tumors, when used at high concentrations. The animals were sacrificed, several days (6-10 days) after nanoparticle administration, and their brain tumor tissues were imaged *ex vivo* using our prototype PAI system. Three tumors were embedded at different locations in the rat brain and then imaged simultaneously. Each tumor was harvested from one of three different rats, two of which were injected with different doses of nanoparticles (125 mg/Kg and 250 mg/Kg of rat weight respectively) and the third rat, which served as control, was not injected with nanoparticles. From the images we were able to clearly distinguish the tumors containing nanoparticle contrast agents that were delivered systemically. In comparison to the nanoprobe containing tumors, the control tumor, which was extracted from a rat not injected with any nanoprobe, did not show any enhanced signal. Our data shows that the targeted CB-PAA NP, at very low concentrations, about 0.84 μM CB dye can be visualized by PAI. Furthermore we observed a 100% increase in the contrast enhancement factor *in vivo* and an 11 fold increase in phantoms. The contrast enhancement factor is defined as the overall ratio of signal to background ratio for tumor containing targeted nanoparticle contrast agent versus that ratio for tumor devoid of contrast agent. [5]

Future directions

1. System Improvement

(i) Modulation of signal from the nanoprobes for better signal to noise ratio: Signal to noise ratio is always a big challenge for imaging and sensing applications. One method of improving the signal to noise ratio would be to modulate the fluorescent or photoacoustic signal from the nanoprobes. This can be achieved with any one of the following approaches. Modulation can be

achieved by incorporating a paramagnetic or superparamagnetic nanoparticle, such as iron oxide, into the polymer matrix along with the dye of interest and then half coating it with a highly reflecting nonmagnetic metal, such as gold or silver. An alternate approach would be to use paramagnetic materials to half coat the nanoparticles [6]. Signal modulation from the nanoparticles can be achieved by either vibrating the nanoparticles or by rotating the nanoprobes, which is less likely to create any perturbation to the system.

(ii) IR based contrast agents with lower fluorescence quantum efficiency: Most of the nanoprobes used in the photoacoustic experiments had an optical absorption in the 560-660nm region, which is in the yellow to red region of the optical spectrum. This region of the spectrum has a fairly good tissue penetration depth for the purpose of photoacoustics. However utilizing probes with spectra that are closer to the NIR region will significantly increase the tissue penetration depth, to a few cm.

Also the photoacoustic signal to noise ratio can be improved by (a) utilizing molecular probes that have a lower fluorescent quantum efficiency, (b)utilizing specially designed nanoprobes containing quenching elements (complex formation, collisional quenching) or (c) having a donor-acceptor pair for resonance-energy-transfer, so as to reduce the fluorescence signal and enhance the photoacoustic efficiency.

(iii) Improvement of photoacoustic System

The two main aspects of medical imaging: (i) Resolution and (ii) Image acquisition time. The chemical sensing and structural imaging described in this thesis were performed using single element transducers. This increases the time of measurement, especially in case of structural imaging. For the purpose of structural imaging of brain tumors the transducer had to be rotated 360^{o} and the photoacoustic signal collected at different angles for applying the back projection

algorithm. This measurement time can be improved by an order of magnitude using a circular array of transducers. Thus the ultimate clinical device would probably involve a transducer array, possibly ring shaped.

The achievable resolution for structural imaging, using the current setup, is quite good (~100's μm). For the purpose of our experiment we used a diffused optical beam and focused ultrasound transducers to collect the signal. However, the spatial resolution can be further improved by utilizing tapered fibers for delivering the excitation light and by utilizing a raster scanning based imaging system.

2. Potential clinical translation

Integration of the nanoplatform and application to clinical settings

The study presented in this thesis gives the proof of principle of a new technology, utilizing different types of nanoprobes that are combined with optical and photoacoustic imaging modalities. These can be utilized for quantitative analysis of chemical and structural properties *in vivo*, with a special emphasis on tumor diagnostics and monitoring.

The next step will be to expand this study on different types of tumor models in small animals. A successful study in animal models will accelerate the development of this technology for comprehensive diagnosis, as well as therapeutic monitoring, of diseases, and will subsequently lead to clinical translation.

While PAI is under intense research and development for potential adaptation to clinical settings and possible FDA approval, the orders of magnitude increases in efficiency afforded by the new nanoprobes described here should promote accelerated clinical implementation of this imaging technique. Recently polymeric nanoparticles based on *poly(lactic-co-glycolic acid*)

(PLGA) have been approved by the FDA for use in human clinical trials [7]; this being first approval of a synthetic polymeric nanoparticle for use in clinical research. This is indeed promising, and will hopefully pave the way for several other polymeric nanoparticles, especially the polyacrylamide based nanoprobes described here, towards achieving FDA approval for clinical trials.

Combining the different types of nanoprobes, presented here, into a single multifunctional nanoprobe, that will enable simultaneous functional and structural imaging, may lead the way to an extremely low cost and highly reliable diagnostic tool. Furthermore, using such a single nanoparticle contrast agent that enables multiple functional and structural imaging functions will obviate the need for healthcare practitioners to perform a series of examinations with a diverse set of contrast agents so as to generate a complete diagnostic assessment. This novel diagnostic strategy will reduce the time and uncertainty associated with multiple agents. Moreover, the ability to perform multiple functional and morphological imaging simultaneously, especially when realized with the low-cost, yet powerful, PAI technique, will help reduce the current exorbitant medical costs associated with diagnosis and treatment of cancer, and many other diseases, a central focus of health care reform. The latter, if successfully implemented, may create a revolutionary impact on the clinical management of diseases.

Reference

1. Ray A, Koo YEL, Epstein T, Kim G and Kopelman R, Two-photon nano-PEBBLE sensors: subcellular pH measurements, *Analyst* 2011, 136; 3616-3622.

2. Ray A, Koo YEL , Kim G and Kopelman R, Two-photon fluorescence imaging super-enhanced by multi-shell nano-photonic particles : Application to subcellular pH, *Small* 2012, 8(14):2213-21.

3. Ray A, Raijan J, Koo YEL, Wang X and Kopelman R, Lifetime based photoacoustic oxygen sensing *in-vivo, Journal of Biomedical Optics* 2012, 17 (5); 057004.

4. Orringer, D. A.; Sagher, O.; Kopelman, R.; Koo, Y. E. Dye loaded nanoparticle. US patent 20100098637, 2010.

5. Ray A, Wang X, Koo Lee YE, Hah HJ, Kim G, Chen T, Orringer DA, Sagher O, Liu X and Kopelman R, Targeted blue nanoparticles as photoacoustic contrast agent for Brain tumor delineation, *Nano Research* 2011, 4(11); 1163-1173.

6. Anker JN and Kopelman R, Magnetically modulated optical nanoprobes, *Appl. Phys. Lett.* 2003, 82: 1102.

7. Lü JM, Wang X, Marin-Muller C, Wang H, Lin PH, Yao Q, and Chen C, Current advances in research and clinical applications of PLGA-based nanotechnology, *Expert Rev Mol Diagn*. 2009, 9(4): 325–341.